



TECHNISCHE
UNIVERSITÄT
WIEN
Vienna University of Technology

DISSERTATION

Ultrastrong Light-Matter Coupling in Circuit QED

ausgeführt zum Zwecke der Erlangung des akademischen Grades eines Doktors der
Naturwissenschaften unter der Leitung von

Assoc. Prof. Dr.rer.nat. Peter Rabl

E141

Atominstitut

eingrichtet an der Technischen Universität Wien

Fakultät für Physik

von

Tuomas Jaako, M.Sc.

Matrikelnummer: 01528773

Untere Weißgerberstraße 10, 1030 Wien

Wien, am

Tuomas Jaako

Diese Dissertation haben begutachtet:

Prof. Dr. David Zueco

Dr. Gheorghe-Sorin Paraoanu



Die approbierte gedruckte Originalversion dieser Dissertation ist an der TU Wien Bibliothek verfügbar.
The approved original version of this doctoral thesis is available in print at TU Wien Bibliothek.

Abstract

In circuit quantum electrodynamics (QED) effective light-matter interactions can be studied in terms of superconducting two-level systems (“artificial atoms”) coupled to microwave resonators. Compared to regular cavity QED systems with atoms and optical photons, the achievable coupling strengths in such artificial systems can be enhanced by many orders of magnitude and even exceed the bare energies of the photons and atoms. In this so-called ultra-strong coupling (USC) regime the simple physics of the Jaynes-Cummings model is no longer valid and new exotic phenomena emerge.

This thesis addresses the physics of circuit and cavity QED systems beyond the standard description based on the Dicke model. First of all, a rigorous derivation of the effective circuit QED Hamiltonian is presented, which shows that the Dicke model is no longer valid in the USC regime of circuit QED. Instead, a new model, the Extended Dicke model (EDM), is identified as a physically consistent description. In the remainder of the thesis, the physics of the EDM is studied, first in the case of non-interacting qubits. From this analysis a new ground state phase, the subradiant phase, is found, where the qubits decouple from the photons, but at the same time they are strongly entangled with each other. In a next step the cases of repulsively and attractively interacting qubits are discussed. From this analysis it can be shown that the origin of the usual superradiant phase transition is related to the presence of attractive qubit-qubit interactions and not to the presence of a cavity mode, as commonly understood. In the successive parts of the thesis also the excited states of the EDM are discussed, in particular in the low-photon-frequency regime. In this limit the photons behave as effective particles moving in a potential landscape determined by the coupling to the qubits. Several symmetry-breaking transition in the qubit excited states are found and ways to probe them are discussed. Finally, as an application of these new USC effects a scheme to extract entanglement from the subradiant vacuum and a quantum simulation scheme of the EDM with trapped ions are proposed and analyzed.

Zusammenfassung

“Circuit quantum electrodynamics (QED)” bezeichnet ein junges Forschungsfeld in dem effective Licht-Materiewechselwirkungen anhand der Kopplung von supraleitenden Qubits (“künstliche Atome”) und Mikrowellenphotonen untersucht werden. Im Vergleich zu traditionellen Resonator QED Systemen mit Atomen und optischen Photonen kann in diesen künstlichen Systemen die Kopplungsstärke um viele Größenordnungen erhöht und dadurch vergleichbar mit der absoluten Energie der Photonen werden. In diesem Regime der sogenannten ultrastarken Kopplung (USK) gelten die bekannten Gesetze der Quantenoptik nicht mehr und neue exotische Phänomene treten zu Tage.

In dieser Dissertation werden die grundlegenden physikalischen Eigenschaften von Circuit- und Resonator-QED Systemen anhand von einfachen Modellen beschrieben und diskutiert. Dazu wird insbesondere durch verschiedene explizite Herleitungen gezeigt, dass in diesem Regime das oft verwendete Dicke Model seine Gültigkeit verliert und durch ein erweitertes Dicke Model (EDM) ersetzt werden muss. Im Bereich USK sagt dieses Model einen neuartigen, subradianten Grundzustand voraus, in welchem die Qubits oder Atome von den Photonen komplett entkoppelt, aber gleichzeitig untereinander stark verschränkt sind. Durch die Ableitung von weiter vereinfachten effektiven Modellen kann diese Phase, so wie auch viele andere Eigenschaften des Grundzustands und der angeregten Zustände von stark-wechselwirkenden Licht-Materie Systemen, verstanden werden. Dadurch konnten mit dieser Dissertation auch jahrelang kontrovers diskutierte Fragen in diesem Feld, wie zum Beispiel die Existenz eines superradianten Phasenübergangs, entgültig geklärt werden. Basierend auf diesem neuen grundlegenden Verständnis werden in dieser Dissertation des Weiteren ein Protokoll diskutiert, um stark verschränkte Zustände aus dem subradianten Vakuum zu extrahieren und die Möglichkeit das EDM mit Hilfe gefangener Ionen zu simulieren im Detail analysiert.

Acknowledgements

It is good to start the thesis with its most important part. My time in Vienna during the last four years doing a PhD have been a pleasure. I have come across many interesting people, and had even more delightful conversations.

I am forever indebted to my supervisor Peter Rabl, without whom this thesis and the work presented in it would not have been possible. During my time here in Vienna I have learned a great deal from him, both about physics and how to lead a group and supervise. Second, I would like to thank my fellow PhD students in the group, Giuseppe Calajó, Yuri Minoguchi, Julian Huber and Daniele De Bernardis. A special mention goes to Thomas Milburn, who sadly passed away three years ago. I am thankful to Daniele with whom I have had many interesting discussions and the pleasure to co-author two papers. Thanks go out to members of the CoQuS programme and its staff. It is a wonderful programme and has provided amazing opportunities for me. A shout out goes also to Ze-Liang Xiang a postdoc in the group when I started my PhD. It was a pleasure to work with him on my first paper.

I am also grateful for my parents for their support in my journey, even though it has brought me far away from home. They have been always encouraging me to learn and develop myself. Without their support I would not be here. Especially a comment from my father after finishing high school has had a big impact on the direction that I have taken.

Lastly I would like to thank my girlfriend. Having her in my life has made this already wonderful time even better. Sometimes physics is very frustrating and her support has made all the difference. I am also grateful to her family who have welcomed me in. Having a second family in Austria when my own is far away has made my life that much more enjoyable.



Die approbierte gedruckte Originalversion dieser Dissertation ist an der TU Wien Bibliothek verfügbar.
The approved original version of this doctoral thesis is available in print at TU Wien Bibliothek.

Contents

1	Introduction	1
1.1	Cavity quantum electrodynamics	1
1.2	Circuit quantum electrodynamics	2
1.3	Ultra-strong coupling	2
1.4	Beyond the Dicke model in circuit QED	3
1.5	Outline	4
2	Superconductivity	7
2.1	Basics of macroscopic superconductivity	7
2.2	Josephson junction	8
2.2.1	Josephson effect	8
2.3	Flux quantization	11
3	Quantum electric circuits	13
3.1	Hamilton formalism for circuits	13
3.1.1	Generalized flux and charge, and types of elements	13
3.1.2	Degrees of freedom and the Hamiltonian	15
3.2	Quantization of circuits	18
3.3	Quantum LC -oscillator	18
3.4	Superconducting qubits	20
3.4.1	Charge qubits	20
3.4.2	Flux qubits	23
3.5	Circuit quantum electrodynamics	26
3.5.1	Capacitive coupling	27
3.5.2	Inductive coupling	31
4	Models of ultra-strong light-matter coupling	35
4.1	Rabi model	35
4.2	The Dicke model	37
4.2.1	Superradiant phase transition	37
4.2.2	The A^2 -term and no-go theorems	39

4.3	The Extended Dicke model	40
4.3.1	Non-interacting qubits	40
4.3.2	Repulsive dipole-dipole interactions	43
4.3.3	Attractive dipole-dipole interactions	45
4.3.4	General description of qubits coupled to a single mode resonator	47
4.4	Justification of the EDM	49
4.4.1	Gauge freedom in cavity QED	49
4.4.2	Case study: flux qubits coupled to an LC-resonator	51
4.4.3	Gauge non-invariance of TLA	52
4.4.4	TLA in Coulomb gauge	52
4.4.5	TLA in electric dipole gauge	53
4.4.6	Validity of the TLA	54
4.4.7	Remarks	56
5	Physics of the Extended Dicke model	59
5.1	Special case of non-interacting qubits	59
5.1.1	Bosonization in the large N limit	59
5.1.2	Light-matter decoupling: the subradiant phase	62
5.2	Phase diagram of cavity QED	69
5.2.1	Normal phase	70
5.2.2	Subradiant phase	71
5.2.3	Superradiant phase	73
5.2.4	Super- to subradiant phase transition	76
6	Ultra-strong coupling radio-frequency circuit QED	79
6.1	Born-Oppenheimer approximation	80
6.2	Adiabatic potential structures	82
6.2.1	Ground state instability	82
6.2.2	Non-interacting qubits	84
6.2.3	General structure	85
6.3	Probing the spectrum	87
6.3.1	Strong-coupling condition	88
6.3.2	Detecting the change in the stability of the excited state	89
6.4	Wave-packet dynamics	91
6.5	Circuit QED implementation	93
7	Generating multi-qubit entanglement from the subradiant vacuum	97
7.1	General description of the protocol	97
7.2	Extracting the ground state entanglement	99

CONTENTS

7.3	Experimental imperfections	101
7.3.1	Extracting entanglement from a thermal state	102
7.4	Circuit QED implementation	103
8	Simulating non-perturbative cavity QED	107
8.1	Trapped-ion implementation of the EDM	108
8.1.1	Collective TLS-field coupling	109
8.1.2	The P^2 -term	110
8.1.3	Dipole-dipole interactions	111
8.1.4	Accessible parameter regimes	112
8.2	Examples	115
8.2.1	Qubit excitation spectrum	115
8.2.2	Ground state preparation	118
8.3	Discussion	119
9	Summary and Outlook	121
9.1	Outlook	123
A	Polaron transformation	125
B	Effective low energy theory for the USC regime	129
B.1	Effective Hamiltonian	129
B.2	Correction to the eigenstates	132
C	Master equation for ultra-strongly coupled systems	135
C.1	Simulation of the master equation with time-dependent couplings	138

Chapter 1

Introduction

1.1 Cavity quantum electrodynamics

The study of light-matter interactions had a paramount importance for the development of quantum mechanics [1]. At first, light-matter interactions were studied in free space, where the coupling between radiation and matter is small. These types of considerations led to, e.g., the understanding of spontaneous emission [2, 3] and the Lamb shift [4]. In 1946 Purcell discovered the *Purcell effect*: enhanced spontaneous emission rate of an atom placed in a resonant cavity [5, 6]. This discovery can be viewed as the start of *cavity quantum electrodynamics* (QED) [7] the study of light-matter interactions between confined electromagnetic modes of a cavity and atoms or other matter systems. The relevant energy scales in the problem are the frequencies of the cavity and the matter systems, ω_r and ω_q , the coupling between light and matter g and the dissipation rates of the cavity and matter, κ and γ , respectively. The Purcell treatment is valid in the *weak coupling* regime of cavity QED where the cavity can still be treated as a continuum, i.e. $g \ll \kappa$.

A new regime of cavity QED is reached when the light-matter coupling g is larger than the dissipation rates γ and κ , the *strong coupling* regime [7, 8]. The strong coupling regime was first demonstrated in systems with a large number of atoms interacting with the electromagnetic field [9]. In multi-atom systems the coupling of light and matter is enhanced by the number of atoms N to $\sqrt{N}g$, which facilitated the observation of the strong coupling regime with a small single atom-photon coupling $g \ll \kappa, \gamma$. The regime where the collective coupling $\sqrt{N}g$ is larger than the dissipative rates is also called collective strong coupling. With single atoms the strong coupling regime was reached in 1987 using microwave cavities [10]. In the optical regime 5 years later [11]. Since these pioneering experiments strong light-matter coupling has been demonstrated in a variety of

different systems [12–21]. The strong (single atom-photon) coupling regime makes it possible to couple matter to radiation in a highly controllable way, enabling precision control of single quantum emitters, used e.g. for entangling quantum bits (qubits) in small scale quantum processors [22–24].

1.2 Circuit quantum electrodynamics

With the advent of circuit QED [16, 17, 25] the study of light-matter physics with even stronger couplings became relevant. Circuit QED is the study of light-matter interactions in artificial setups. The optical or microwave photons are replaced by microwave photons living in coplanar waveguides, transmission lines or lumped element LC -circuits. These harmonic systems are coupled to superconducting (SC) qubits, which play the role of artificial atoms. The advancement of the SC technology in last decades has been staggering, and nowadays SC qubits and circuit QED are one of the leading technologies in the pursuit of building a universal quantum computer [26, 27].

In many systems the single atom-photon coupling g is inherently small [28], and it is enhanced by coupling a large number of matter constituents to the electromagnetic field. In these cases the system can usually be described by a linearised model [29], which loses the inherent non-linear character of the atoms. In circuit QED, however, even the single photon-atom coupling strength can be very strong [28]. One of the reasons of strong light-matter in circuit QED is the small mode volumes of the “cavities” used. For example, in a transmission line resonator the field is strongly confined along the transverse directions, reducing the mode volume well below the limit λ^3 , where λ is the resonant wavelength, of a traditional 3D cavity [25, 30]. Another advantage is the engineerability of SC qubits. Experimenters do not have to settle for what nature provides them, rather SC qubits can be designed to have properties needed in the experiment in question, whether that is long coherence times [31–33], or large anharmonicity [34].

1.3 Ultra-strong coupling

The most extreme regime of light-matter interactions is reached when the coupling is in the order of the bare energies of the atoms and the field, ω_q and ω_r . This regime is called the *ultra-strong coupling* (USC) regime and for historical reasons has been considered to start at $g/\omega_{r/q} = 0.1$ [35, 36]. This is an arbitrary bound and has no physical meaning, rather it was set by the first experiments observing the breakdown of the rotating wave approximation (RWA) [37–39]. In this thesis we, however, set the limit of USC to $g/\omega_{r/q} \sim 1$, in the literature sometimes referred to

as the deep strong coupling (DSC) regime [40], which has also been experimentally demonstrated [41–43]. In the USC regime many exotic features of light-matter coupled systems have been predicted, such as ground state entanglement [44–46], phase transitions [47, 48] and light-matter decoupling [49–51]. Also some applications of USC have been proposed such as protected [52], holonomic [53] and ultrafast [54] quantum computing, ultrafast gates [55], quantum memories [56, 57] and entanglement harvesting [58]. Compared to regular cavity QED, the range of applications in the USC regime is, however, still limited and most of the physics in this regime is still unexplored.

1.4 Beyond the Dicke model in circuit QED

This thesis concentrates on the physics of circuit QED systems in the USC regime, which has been recently demonstrated in experiments with single superconducting flux qubits [41, 42]. At the starting point of this thesis, there was still a debate about the correct effective models to use to describe the physics of cavity and circuit QED systems in this regime [47, 48, 59–66]. The debate concerned mostly the existence or non-existence of the superradiant phase transition SRPT, predicted to occur in the ground state of the Dicke model (DM) [47, 48]. It was later shown that the so-called A^2 -term, appearing in the minimal coupling Hamiltonian, prevents such a transition [59, 60]. In the context of circuit QED it was claimed in Ref. [65] that such a mechanism does not exist in circuit QED systems, while Ref. [66] argued, based on very general considerations, that a SRPT does not exist in these systems either.

One of the main motivations for this thesis was to resolve these contradictions, and to provide a consistent description of multi-qubit circuit QED systems in the USC regime. This we achieved by a rigorous derivation of the effective circuit QED Hamiltonian starting from the full circuit models, considering both charge and flux qubits, and different coupling schemes. These explicit first-principle derivations show that neither the Dicke model nor the Dicke model with the A^2 -term provide a correct description of these circuits. Instead, the Extended Dicke model (EDM) is identified as a minimal model for multi-qubit cavity QED systems in the USC regime. This new model resolves the issue of the SRPT in the DM, is physically consistent with basic electrostatics and gives the SRPT a new interpretation as an instability of interacting qubit ensembles [50, 51].

In addition to resolving long-lasting debates in the field of cavity QED, the EDM predicts very different USC physics than what has been discussed in the context of the DM. Thus, a large part of this thesis has been devoted to the analysis of the ground and excited states of the EDM, approximation methods for the USC regime and first potential applications of the new effects. These effective

models have been compared to exact numerical simulations of small circuits in order to identify realistic configurations, where this new physics could be observed. In this regime, compared to regular circuit QED, the anharmonicity of the qubit circuit has turned out to be the most crucial criterion, which makes flux qubits [67] one of the most promising systems to explore this physics. In recent years work towards USC using charge qubits [17, 31] has been made [68, 69]. In these systems the qubits are only weakly anharmonic which sets bounds on the theoretically obtainable coupling strengths [50, 68, 70]. A limitation that is not present in the highly anharmonic flux qubit systems [50, 70, 71].

1.5 Outline

This thesis is organized as follows: In [Chap. 2](#) we present the basics of superconductivity that are needed to understand superconducting circuits, the Josephson effect and flux quantization. [Chap. 3](#) is dedicated to the Hamiltonian formalism in circuits and circuit quantization. The quantum LC -oscillator is presented along with two main types of qubits, the charge and the flux qubit. At the end of the chapter we discuss coupling of qubits to LC -circuits. The main coupling schemes, capacitive and inductive coupling, are introduced, and bounds and scalings for the obtainable light-matter coupling strength are derived.

In [Chap. 4](#) we first discuss the two main USC models in the literature the Rabi model and the Dicke model. We explain the superradiant phase transition found in the Dicke model and the A^2 no-go theorem based on the minimal coupling Hamiltonian. Next we derive, with explicit examples, a new model for USC systems the Extended Dicke model (EDM). We analyze three different example circuits: non-interacting and attractively or repulsively interacting qubits coupled to a field mode. Lastly we show that the EDM is an accurate two-level-truncated description of the full physics in the USC regime in contrast to the Dicke model. The reason for the lower accuracy of the two-level-approximation in the Dicke model is identified as the momentum coupling to the electromagnetic field found in the minimal coupling Hamiltonian.

[Chap. 5](#) analyses the physics of the EDM. The ground state phase diagram is discussed. A new vacuum state, the subradiant vacuum, is found in the USC regime for systems of non-interacting qubits or qubits with repulsive dipole-dipole interactions. In the subradiant phase the qubits and the harmonic mode are shown to decouple, while the qubits are strongly entangled. The Dicke SRPT is given a new interpretation as an instability of an attractively interacting TLS ensemble, which is not created by the cavity mode. A new phase transition from the superradiant phase to the subradiant phase is found and its properties are discussed.

In [Chap. 6](#) an extreme parameter regime in which the mode frequency is much

smaller than that of the qubits is discussed. A Born-Oppenheimer approximation is used to analyze the situation and many instabilities are found in the excited states. Protocols to probe the instabilities only involving qubit operations are presented. The subradiant vacuum is put to use in [Chap. 7](#) where it is used to extract multi-qubit entangled states. The presented protocol is shown to be robust against relevant experimental limitations and non-idealities. A flux qubit implementation of the protocol is presented at the end of the chapter. Lastly a trapped-ion quantum-simulation scheme of the EDM is proposed in [Chap. 8](#). Using appropriately chosen driving lasers the EDM Hamiltonian can be implemented as the effective Hamiltonian description. The entanglement extraction protocol of [Chap. 7](#) is used to prepare the ion system in the subradiant vacuum state and a measurement of the spectrum is described. In [Chap. 9](#) we summarize our findings and give an outlook on possible future research directions.

This thesis also includes three appendices that give more details on the derivations presented. In [App. A](#) the Polaron transformation is presented, and it is applied to the EDM. The following appendix, [App. B](#), presents details on the perturbation theory used to derive the effective low-energy description used in [Chap. 5](#). Lastly the USC master equation used in [Chap. 7](#) is derived in [App. C](#).

Chapter 2

Superconductivity

In this chapter we present the basics of the phenomenon of superconductivity, that are needed to understand the properties of superconducting circuits used in the rest of the thesis. We begin with a short review of the basics of the superconducting state, then we give a phenomenological explanation of the Josephson effect and the properties of a Josephson junction, the fundamental building block of superconducting qubits. Lastly we go through the effect of flux-quantisation, extremely important for “flux-type” superconducting qubits i.e. flux qubits. The discussion in this chapter is mainly based on references [72, 73].

2.1 Basics of macroscopic superconductivity

The microscopic theory of conventional superconductors, the BCS theory [74, 75], was developed in the 1950’s by Bardeen, Cooper and Schrieffer. Before the BCS theory a phenomenological macroscopic theory was developed by Ginzburg and Landau [76, 77], verified by the microscopic theory of BCS. The basic assumption of the macroscopic model is that the *Cooper pairs* of the superconducting state can be described by a macroscopic wave function

$$\psi(\mathbf{r}, t) = \sqrt{\rho(\mathbf{r}, t)}e^{i\varphi(\mathbf{r}, t)}, \quad (2.1)$$

where $\rho(\mathbf{r}, t)$ is the density of Cooper-pairs and $\varphi(\mathbf{r}, t)$ is the phase of the wave function [72]. Using basic relations of quantum mechanics and electromagnetism, an equation for the supercurrent density in the metal can be derived [72]

$$\mathbf{j} = \frac{e^*\hbar}{2im^*} (\psi^*\nabla\psi - \psi\nabla\psi^*) - \frac{e^{*2}}{m^*c}|\psi|^2\mathbf{A}, \quad (2.2)$$

with effective charge $e^* = -2e$ and effective mass $m^* = 2m_e$ of a Cooper pair, e being the elementary charge and m_e the mass of an electron. In Eq. (2.2) \mathbf{A}

denotes the vector potential related to the magnetic field $\mathbf{B} = \nabla \times \mathbf{A}$. For the macroscopic wave function Eq. (2.1) we obtain

$$\mathbf{j} = \frac{\hbar e^* \rho}{m^*} \left(\nabla \varphi - \frac{e^*}{\hbar} \mathbf{A} \right), \quad (2.3)$$

where the term in the parentheses is the *gauge invariant phase difference*. From this expression the London equations [78] can be deduced, and, thus, the two fundamental attributes of superconductivity, the Meissner effect [79] and vanishing electrical resistance [80], can be explained.

2.2 Josephson junction

The Josephson junction is probably the most important circuit element in circuit quantum electrodynamics. Its non-linear current characteristic allows it to be used to create circuits with anharmonic energy spectra. A Josephson junction is comprised of two superconductors separated by a thin layer of oxide, acting as an insulating barrier. The effect responsible for the properties of the Josephson junction is called the *Josephson effect*, which we will now briefly review.

2.2.1 Josephson effect

The Josephson effect was discovered theoretically by Josephson in 1962 [81]. He predicted the current and voltage relations across the junction. Already before Josephson's findings, the DC Josephson effect had been observed in experiments, but it had been attributed to imperfections in the set-up. The first experimental verification of Josephson's predictions was conducted by Philip Anderson and John Rowell [82] the next year.

The first Josephson relation tells how the junction behaves when there is no voltage bias on the junction. It states that the current is given by

$$I(t) = I_c \sin(\varphi(t)), \quad (2.4)$$

where I_c is the critical current, that is the maximal current the junction can pass through while remaining in the superconducting state. The phase φ is the phase difference of the wave functions of the two superconductors connected by the insulating layer, $\varphi = \varphi_L - \varphi_R$ and $\psi_{L/R} = \sqrt{\rho_{L/R}} e^{i\varphi_{L/R}}$ with $L(R)$ referring to the superconductor left(right) of the insulating barrier. If the phase difference is non-zero, $\text{mod } \pi$, the junction supports a current without a voltage difference.

The second Josephson relation describes the behaviour of the voltage across the junction. It is given by

$$V(t) = \frac{\hbar}{2e} \frac{d\varphi}{dt}(t) = \Phi_0 \frac{d\varphi}{dt}(t), \quad (2.5)$$

where we have defined the reduced flux quantum (the origin of which is explained in the next section) $\Phi_0 = \hbar/(2e)$ and φ is again the phase difference. This means that if we bias the junction with an external DC voltage source such that $V(t) = V_{\text{DC}}$ the phase evolves as

$$\varphi(t) = \frac{V_{\text{DC}}t}{\Phi_0} + \varphi_0, \quad (2.6)$$

where φ_0 is the initial value of the phase, such that the resulting current is

$$I(t) = I_c \sin\left(\frac{V_{\text{DC}}t}{\Phi_0} + \varphi_0\right). \quad (2.7)$$

The DC voltage bias, thus, results in AC current flowing through the junction. The angular frequency of the AC current is V_{DC}/Φ_0 .

Comparing the second Josephson relation to Lenz's law

$$V = -\frac{d\Phi}{dt}, \quad (2.8)$$

where Φ is a magnetic flux, we can say that the superconducting phase difference acts for all intents and purposes like a magnetic flux.

The detailed derivation of the Josephson relations from microscopic details is a complicated task, which we will not undertake. The effect can be understood based on the phenomenon of *Andreev reflection* [83]. However, can one understand these relations from simple arguments in a qualitative way?

Simple derivation of the Josephson relations

If we take as for granted the fact that Cooper-pairs can tunnel through the insulating barrier coherently, it is possible to understand the Josephson relations based on a simple model. We do this below.

In a superconductor the electrons have paired into Cooper-pairs of charge $-2e$. Let us say there are N Cooper-pairs in the superconductor when it is in its ground state. The total Cooper pair number is a conserved quantity as long as the superconductor stays in the ground state. Now let us take two such superconductors and connect them with a thin insulating layer to form a Josephson junction. Let us call the total number of Cooper-pairs in these two superconductors N . The number of Cooper-pairs on the two superconductors can change, if the insulating layer is not too thick, say N_L in the left superconductor and N_R in the right superconductor, the only constraint is that $N_L + N_R = N = \text{const.}$ at all times. The individual Cooper-pair numbers for the left and right superconductors N_L and N_R change by a Cooper-pair tunnelling through the insulating barrier to the other side. In the

first approximation we neglect the energy required to place an extra charge on the superconductors, such that all combinations of N_L and N_R , with the constraint $N_L + N_R = N$, have the same energy. The quantum states can be labelled as

$$|N_L + l, N_R - l\rangle \quad (2.9)$$

where l is the number of Cooper-pairs that have tunnelled from the right superconductor to the left after some, arbitrary, reference point with N_L pairs on the left and N_R on the right. Negative value of l signifies that Cooper-pairs have tunnelled from left to right. These sites form a “tight-binding” lattice in the space of $|N_L + l, N_R - l\rangle$ states. The tunnelling of a Cooper-pair from right to left through the junction is a hop between adjacent lattice sites $|N_L + l, N_R - l\rangle$ and $|N_L + l + 1, N_R - l - 1\rangle$. This process costs some amount of energy let us call it E_J . It is the energy cost of transporting a single Cooper-pair through the junction. The Hamiltonian for this system then reads

$$H = \sum_l -\frac{E_J}{2} [|N_L + l, N_R - l\rangle \langle N_L + l + 1, N_R - l - 1| + \text{H.c.}], \quad (2.10)$$

where H.c. stands for the Hermitian conjugate. This Hamiltonian can be diagonalized to [84]

$$H = \sum_{\varphi} -E_J \cos(\varphi) |\varphi\rangle \langle \varphi|, \quad (2.11)$$

where φ is the Fourier transform of the tunnelled Cooper-pair number l . Since l and φ are connected by a Fourier transform we know φ has to be a phase variable. It can be identified as the phase difference between the superconductors introduced above. If we now consider the current of Cooper-pairs from right to left we obtain

$$I = 2e \frac{1}{\hbar} \frac{\partial}{\partial \varphi} [-E_J \cos(\varphi)] = I_c \sin(\varphi), \quad (2.12)$$

which is exactly the first Josephson relation, Eq. (2.4). Above we have used the definition of the group velocity $v_g(\varphi) = \partial_{\varphi} E / \hbar$, multiplied by the charge to get the current and defined the energy scale E_J through the critical current $E_J = \Phi_0 I_c$.

This treatment gives an intuitive picture of the $\sin(\varphi)$ dependence of the current by relating it to the well know tight-binding picture. This is of course not a comprehensive explanation. We did not give an explanation why the Cooper-pairs can move across the insulator in pairs without breaking them, for instance.

Also the second Josephson relation can be understood from this tight-binding picture. Biasing of the junction with an external voltage can be taken into account by adding a term

$$H_{\text{DC}} = -2eV_{\text{DC}}n, \quad (2.13)$$

to the Hamiltonian, where $n = \sum_l l |N_L + l, N_R - l\rangle \langle N_L + l, N_R - l|$ is the number of Cooper-pairs transferred across the junction. The time evolution for the phase φ is then given by

$$\frac{d\varphi}{dt} = -\frac{i}{\hbar}[H_{\text{DC}}, \varphi] = \frac{V_{\text{DC}}}{\Phi_0}, \quad (2.14)$$

which is the second Josephson relation.

2.3 Flux quantization

Superconducting loop pierced by a magnetic flux

A phenomenon of superconductivity important to us is *flux quantization*. Consider a loop made out of superconducting metal, cooled into its superconducting state. Let us place the loop in a magnetic field \mathbf{B} , smaller than the critical field B_c . The current density in the superconductor is given by Eq. (2.3) above. Since the field is smaller than the critical field the current density inside the superconductor vanishes, $\mathbf{j} = 0$. Thus, we also have

$$0 = \oint_C \mathbf{j} \cdot d\mathbf{l} = \oint_C (\hbar \nabla \varphi - 2e\mathbf{A}) \cdot d\mathbf{l} = 2\pi \hbar n - 2e \int \nabla \times \mathbf{A} \cdot d\mathbf{a}, \quad (2.15)$$

where C is a path inside the superconducting ring, $n \in \mathbb{Z}$ is an integer, due to the uniqueness requirement on the wave function (going around the ring can change the phase only by an integer multiple of 2π). In the last step in Eq. (2.15) we have converted the closed line integral to a surface integral over the area enclosed by C . From the above equation it follows that the magnetic flux threading the superconducting loop satisfies

$$\Phi = \int \mathbf{B} \cdot d\mathbf{a} = 2\pi n \Phi_0, \quad (2.16)$$

That is the flux penetrating a superconducting loop is quantized in units of the flux quantum, $2\pi\Phi_0 = h/(2e)$. The above result holds in the case that the superconducting loop is much thicker than the London penetration depth λ_L . If the thickness is on the order of λ_L the flux is still quantized, but the quantization unit can be different from $2\pi\Phi_0$.

A loop interrupted by junctions and/or inductors

Consider now that we interrupt the loop with a Josephson junction. Since the superconducting phase difference φ behaves as a magnetic flux, up to unit conversion, we must include it in Eq. (2.15). The equation including the phase difference

becomes

$$0 = 2\pi\hbar n - \hbar\varphi - 2e \int \mathbf{B} \cdot d\mathbf{a}, \quad (2.17)$$

and, thus, instead of Eq. (2.16) we get

$$2\pi\Phi_0\varphi + \Phi = 2\pi n\Phi_0. \quad (2.18)$$

That, is the phase difference and the external magnetic flux must sum up to multiple of the flux quantum. Going forward we absorb $2\pi n\Phi_0$ into the definition of the external flux.

For a loop intersected by multiple junctions the above formula generalizes to

$$\sum_i 2\pi\Phi_0\varphi_i + \Phi = 0. \quad (2.19)$$

If there are inductors part of the loop the flux penetrating the inductor has to be also taken account. In general we can write

$$\sum_i \Phi_i + \Phi_e = 0, \quad (2.20)$$

where the Φ_i are fluxes corresponding to Josephson junctions through the phase difference, or actual magnetic fluxes in inductors, and Φ_e is the external magnetic flux threading the loop formed by the inductors and Josephson junctions.

The flux quantization condition Eq. (2.20) is very important when it comes to the analysis of flux type superconducting qubit, as we will see in Chap. 3. These types of qubits always include a loop which is biased with an external magnetic flux.

Chapter 3

Quantum electric circuits

This chapter is dedicated for presenting the required theoretical formalism for modelling quantum electromagnetic circuits. We begin by reviewing the Hamiltonian description of electric circuits, a central tool in circuit QED. We proceed by applying this formalism to the simplest possible circuit, the LC resonator. Afterwards we move to non-linear systems and discuss the most important superconducting qubit types, the charge and flux qubits. Lastly we couple both types of qubits to LC -oscillators and derive scalings and bounds to the obtainable coupling strength. The Hamilton formalism for circuits presented in this chapter is mainly based on reference [85].

3.1 Hamilton formalism for circuits

At an abstract level electric circuits are networks of elements which are connected by nodes. The elements can be in principle be connected to an arbitrary number of nodes. In this chapter and the whole thesis we are, however, only dealing with dipole elements, i.e. elements that connect to two nodes only. The dipole elements constitute what are called the branches of the networks. In addition we only consider non-dissipative circuits in this chapter.

3.1.1 Generalized flux and charge, and types of elements

To each branch of the network, or rather to the element in each branch, we relate two variables, the branch voltage $V_b(t)$, over the element, and branch current $I_b(t)$, flowing through the element. The branch voltages and currents are defined through

the underlying electromagnetic fields as [85]

$$V_b(t) = \int_{\text{start of } b}^{\text{end of } b} \mathbf{E}(\mathbf{r}, t) \cdot d\mathbf{s}, \quad (3.1)$$

$$I_b(t) = \frac{1}{\mu_0} \oint_{\text{around } b} \mathbf{B}(\mathbf{r}, t) \cdot d\mathbf{s}. \quad (3.2)$$

The direction of the positive current and voltage for each branch is arbitrary, but we choose the positive current and voltage directions to be the opposite, as is usually done. The energy stored in an element is obtained from the familiar expression for power, $P = VI$, by integrating over time [85]

$$E_b(t) = \int_{-\infty}^t V_b(t') I_b(t') dt'. \quad (3.3)$$

The lower bound of the integral, $-\infty$, refers to a time far in the past when the circuit was at rest. An element is conservative, i.e. non-dissipative, if the energy is stored in the electromagnetic field.

From the branch currents and voltages one can define another set of variables which are essential for the development of the Hamiltonian description for circuits. These variables are called the branch flux and branch charge defined through the voltages and currents as [85]

$$\Phi_b(t) = \int_{-\infty}^t V_b(t') dt', \quad (3.4)$$

$$Q_b(t) = \int_{-\infty}^t I_b(t') dt'. \quad (3.5)$$

Again the lower bound of the integral refers to a time in the distant past when no currents or voltages were present.

An element is said to be capacitive if the voltage $V(t)$ across it is directly only a function of the charge $Q(t)$ and nothing else

$$V(t) = f(Q(t)). \quad (3.6)$$

The capacitance of the element is then defined to be

$$C(Q) = \left[\frac{df}{dQ} \right]^{-1} \quad (3.7)$$

and it only depends on the charge. For a linear capacitance $C(Q) = C$ is independent of Q , and thus $V = Q/C$. The energy stored by a linear capacitance is easily calculated from Eq. (3.3) to be

$$E(t) = \frac{Q(t)^2}{2C} = \frac{C\dot{\Phi}(t)^2}{2}, \quad (3.8)$$

where we have used $I(t) = \dot{Q}(t)$ and $V(t) = \dot{\Phi}(t)$, from the definitions Eq. (3.4) and Eq. (3.5), to obtain the two different forms.

An inductive element is an element for which the current $I(t)$ is a direct function of the flux $\Phi(t)$ only. The inductance of the element is defined as

$$L(\Phi) = \left[\frac{df}{d\Phi} \right]^{-1} \quad (3.9)$$

which only depends on the flux. A linear inductor is an inductive element for which the inductance $L(\Phi) = L$ is independent of the flux Φ . The energy stored by a linear inductor is given by

$$E(t) = \frac{\Phi(t)^2}{2L} = \frac{L\dot{Q}(t)^2}{2}, \quad (3.10)$$

where we have again used Eq. (3.4) and Eq. (3.5) to obtain the two different forms.

In Sec. 2.2 we saw that the current through a Josephson junction is sinusoidal in the generalized flux, the first Josephson relation Eq. (2.4), thus, it is an inductive element but not a linear inductance. The inductance of a Josephson junction is given by

$$L = \frac{\Phi_0}{I_c \cos\left(\frac{\Phi}{\Phi_0}\right)} \equiv \frac{L_J}{\cos\left(\frac{\Phi}{\Phi_0}\right)}, \quad (3.11)$$

where Φ_0 is the reduced flux quantum and we have defined for future reference the linear Josephson inductance $L_J = \Phi_0/I_c$, i.e. the flux independent part of the inductance. With the help of the second Josephson relation we calculate the energy stored by the junction to be

$$E(t) = \frac{\Phi_0^2}{L_J} \left[1 - \cos\left(\frac{\Phi(t)}{\Phi_0}\right) \right] \equiv E_J \left[1 - \cos\left(\frac{\Phi(t)}{\Phi_0}\right) \right], \quad (3.12)$$

In the rest of the work we use the Josephson energy to characterize a junction rather than the critical current I_c . Many times the constant term E_J is dropped so that the energy is varies between $-E_J$ and E_J .

3.1.2 Degrees of freedom and the Hamiltonian

A circuit has less degrees of freedom than it has branches, due to restrictions from Kirchhoff's laws: the sum over voltages around every closed loop must be zero and

the sum of currents arriving to a node must also be zero. In terms of the flux and charge variables these rules read [85]

$$\sum_{b \in l} \Phi_b = \tilde{\Phi}_l, \quad (3.13)$$

$$\sum_{b \rightarrow n} Q_b = \tilde{Q}_n, \quad (3.14)$$

where the sums go over all branch fluxes Φ_b that are in loop l and branch charges Q_b which arrive to node n , and $\tilde{\Phi}_l$ and \tilde{Q}_n are constants. Using these equations one has to eliminate the extra variables from the problem. The Kirchoff's rule for the branch flux is the same as the flux quantization condition Eq. (2.20). We use a technique called the method of nodes to arrive at the solution. It works for circuits which contain only linear capacitances [85]. This is in practice not a stringent constraint, and especially all problems in circuit QED fall under the applicability of this method.

We start by choosing a node in the circuit to be the ground node with respect to all other nodes are defined, analogously to the ground point chosen for the voltage, and is chosen to have the value of zero. Then we form a spanning tree for the circuit, that is we form a path from the ground node to every other node through capacitors only and without forming loops. To the nodes of the spanning tree we can attach a node flux ϕ_n . The node fluxes are related to the branch fluxes through relations [85]

$$\Phi_{b \in T} = \phi_n - \phi_{n'}, \quad (3.15)$$

$$\Phi_{b \notin T} = \phi_n - \phi_{n'} + \tilde{\Phi}_b, \quad (3.16)$$

where T is the set of branches in the spanning tree and $\tilde{\Phi}_b$ is the flux, finite or vanishing, enclosed by a loop containing the branch in question.

Now that we have the degrees of freedom for the circuit we can set up the Lagrangian. The Lagrangian is the difference between the kinetic, E_{kin} , and potential, E_{pot} , energies of the system. For our circuits, due to the choice of using the method of nodes, the capacitive elements provide the kinetic energy, since their energy depends on the time-derivative of the node flux, Eq. (3.8) $E = C\dot{\Phi}^2/2$. The inductive elements give the potential energy. Thus, the symmetry between flux/charge and capacitive/inductive elements has been broken and the flux plays the role of "position" [85]. The Lagrangian will then have the general form

$$\mathcal{L} = \frac{1}{2} \dot{\phi}^T \mathcal{C} \dot{\phi} - \sum_b f(\Phi_b), \quad (3.17)$$

where f is either $f(\Phi) = \Phi^2/(2L_b)$ for linear inductances or $f(\Phi) = -E_J \cos(\Phi/\Phi_0)$ for Josephson junctions, and the sum goes over all the branches of the spanning

tree. The vector $\dot{\phi}$ is the a vector of the time-derivatives of the node fluxes and the matrix \mathcal{C} is the capacitance matrix. The diagonal elements of \mathcal{C} are the sums of the capacitances connected to a node and off-diagonal elements the negation of the capacitances between nodes. Naturally the branch fluxes have to be expressed through the node fluxes using Eq. (3.15). The equations of motion for the circuit then follow from the Lagrangian through the Euler-Lagrange equations

$$\frac{d}{dt} \left(\frac{\partial \mathcal{L}}{\partial \dot{\phi}_n} \right) - \frac{\partial \mathcal{L}}{\partial \phi_n} = 0 \quad (3.18)$$

as it should be.

Having established the Lagrangian there is only two step left to obtain the Hamiltonian. The conjugate momenta related to the node fluxes are defined, as always, through

$$q_n = \frac{\partial \mathcal{L}}{\partial \dot{\phi}_n}. \quad (3.19)$$

Since we restrict ourselves to linear capacitive elements the conjugate momenta $q_n = \sum_{n'} \mathcal{C}_{nn'} \dot{\phi}_{n'}$ in general. The conjugate momentum is called the node charge or conjugate charge and has the meaning of sum over all the charges on the capacitor plates connected to the node in question. Defining a vector of node charges \mathbf{q} we can write

$$\mathbf{q} = \frac{\partial \mathcal{L}}{\partial \dot{\phi}} = \mathcal{C} \dot{\phi}. \quad (3.20)$$

The Hamiltonian for the circuit is then given by the sum of the kinetic energy, $E_{\text{kin}} = E_{\text{kin}}(\{q_n\})$ now expressed with the node charges q_n , and the potential energy E_{pot}

$$\mathcal{H} = \frac{1}{2} \mathbf{q}^T \mathcal{C}^{-1} \mathbf{q} + E_{\text{pot}}. \quad (3.21)$$

Again the equations of motion are reproduced through the Hamilton's equations

$$\dot{\phi}_n = \frac{\partial \mathcal{H}}{\partial q_n} \quad (3.22)$$

$$\dot{q}_n = -\frac{\partial \mathcal{H}}{\partial \phi_n}. \quad (3.23)$$

Note that the particular form of the Hamiltonian depends on the choice of the spanning tree.

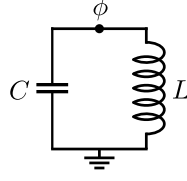


Figure 3.1: LC -oscillator: The simplest (quantum) circuit. A capacitor with capacitor C and an inductor with inductance L connected together form a circuit which obeys the equation of motion for a harmonic oscillator. The ground node is marked with the line and three bars. The active node is the one on the top where L and C meet.

3.2 Quantization of circuits

Having established the classical Hamiltonian for a circuit the quantization of the Hamiltonian is performed in a canonical manner. The conjugate pairs ϕ_n and q_n are promoted to operators $\hat{\phi}_n, \hat{q}_n$ satisfying the canonical commutation relation

$$\left[\hat{\phi}_n, \hat{q}_{n'} \right] = i\hbar \delta_{nn'}, \quad (3.24)$$

where $\delta_{nn'}$ is the Kronecker-delta. Analogous to spatial problems $\hat{q}_n = -i\hbar \frac{d}{d\phi_n}$. For nodes that are connected to capacitors and Josephson junctions only there is a slight correction to this. In this case the node flux is a compact variable defined only modulo Φ_0 [28, 85]. This leads to a modified commutation relation between \hat{q} and $\hat{\phi}$ [28]

$$\left[e^{i\hat{\phi}/\Phi_0}, \hat{q} \right] = -2e \times e^{i\hat{\phi}/\Phi_0}. \quad (3.25)$$

For $\hat{\phi} \ll \Phi_0$ this gives back the standard relation Eq. (3.24). In the following we always omit the hat's above operators for notational convenience.

3.3 Quantum LC -oscillator

The simplest quantum circuit is arguably the quantum LC oscillator Fig. 3.1. The circuit consists of just a linear capacitance and inductance and has two nodes: the ground node and one active node. We label the active node as ϕ , which in this case has the meaning of the magnetic flux threading the inductor. The Lagrangian of the LC resonator is then, using the prescription laid out in Sec. 3.1,

$$\mathcal{L} = \frac{C\dot{\phi}^2}{2} - \frac{\phi^2}{2L}. \quad (3.26)$$

The conjugate charge to ϕ is given by $q = \partial\mathcal{L}/\partial\dot{\phi} = C\dot{\phi}$. Finally the Hamiltonian is given by

$$\mathcal{H} = \frac{q^2}{2C} + \frac{\phi^2}{2L}. \quad (3.27)$$

The equations of motion for a harmonic oscillator are recovered using the Hamilton's equations, Eq. (3.22),

$$C\ddot{\phi} + \frac{\phi}{L} = 0. \quad (3.28)$$

We see that the capacitance C plays the role of the mass in the mechanical analog and inductance L is the inverse spring constant.

The quantum version is obtained by raising the conjugate pair ϕ , q to operators with commutation relation Eq. (3.24). We can also introduce the raising and lowering operators a^\dagger and a , as usual, defined by

$$\begin{aligned} a &= \sqrt{\frac{\omega C}{2\hbar}} \left(\phi + \frac{i}{\omega C} q \right), \\ a^\dagger &= \sqrt{\frac{\omega C}{2\hbar}} \left(\phi - \frac{i}{\omega C} q \right). \end{aligned} \quad (3.29)$$

With these operators the Hamiltonian reads

$$H = \hbar\omega \left(a^\dagger a + \frac{1}{2} \right), \quad (3.30)$$

where $\omega = 1/\sqrt{LC}$ is the frequency of the quantum LC resonator. Inverting the relations Eq. (3.29) gives us ϕ and q in terms of a and a^\dagger ,

$$\begin{aligned} \phi &= \sqrt{\frac{\hbar}{2\omega C}} (a^\dagger + a), \\ q &= i\sqrt{\frac{\hbar\omega C}{2}} (a^\dagger - a). \end{aligned} \quad (3.31)$$

Thus, the zero point flux and charge, for a harmonic oscillator, are given by $\phi_{\text{zpf}} = \sqrt{\hbar/(2\omega C)} = \sqrt{\hbar Z/2}$ and $q_{\text{zpf}} = \sqrt{\hbar\omega C/2} = \sqrt{\hbar/(2Z)}$, where we have defined the impedance $Z = \sqrt{L/C}$ of the resonator. The scaling of the flux and charge zero-point fluctuations with \sqrt{Z} and $\sqrt{Z^{-1}}$, respectively, will turn out to be very important later when estimating the coupling strengths of different coupling schemes [28, 50].

3.4 Superconducting qubits

In this section we briefly review the two main types of superconducting qubits (SC), the charge based qubit and the flux based qubit. They both have their own merits in simplicity, ease of manufacturing, control etc. What we are most interested in is their usefulness in ultra-strong coupling physics.

3.4.1 Charge qubits

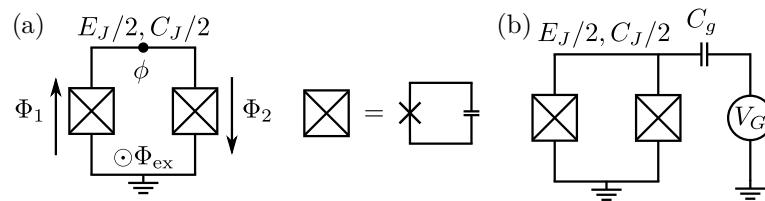


Figure 3.2: Charge qubit designs. (a) The widely used transmon qubit design. (b) Cooper-pair-box qubit, the external biasing voltage V_G is added so that the CPB can be biased to its charge sweet spot $C_g V_G / (2e) = 1/2$. The fluxes are defined as in (a).

The most widely deployed SC qubit is a charge qubit called a *transmon* [31]. It is used in many current experimental works in circuit QED and in most efforts towards building a universal quantum computer based on superconducting qubit technology.

In Fig. 3.2(a) the circuit diagram for a transmon qubit is shown. It consists of a loop made out of two Josephson junctions (JJ) threaded by an external flux Φ_{ex} . This design is not the simplest one for a transmon, a single Josephson junction would do as well, but the addition of another one adds the ability to tune the qubit using Φ_{ex} . This loop made out of two JJs is called a superconducting quantum interference device (SQUID). We assume the junctions to be identical with capacitances $C_J/2$ and Josephson energies $E_J/2$. In real world experiments there would be a large shunt capacitance in parallel with the junctions. Here we have for simplicity omitted this large capacitor and simply assume the junction capacitances to be large instead. This does not change the physics in anyway.

One of the capacitors is chosen to be the branch in the spanning tree and the rest of the branch fluxes will be determined by Eq. (3.15). The flux at the active node is labelled as ϕ . There is a closed loop in the circuit formed by the two junctions and we have to use the flux quantization condition Eq. (2.20). That is the branch fluxes for the Josephson junctions Φ_1 and Φ_2 for the left and the right

junction, respectively, are related by

$$\Phi_1 + \Phi_2 = \Phi_{\text{ex}}. \quad (3.32)$$

The Lagrangian for the transmon reads

$$\mathcal{L} = \frac{C_J \dot{\phi}^2}{2} + E_J/2 \left[\cos \left(\frac{\phi + \Phi_{\text{ex}}/2}{\Phi_0} \right) + \cos \left(\frac{\phi - \Phi_{\text{ex}}/2}{\Phi_0} \right) \right] \quad (3.33)$$

$$= \frac{C_J \dot{\phi}^2}{2} + E_J \cos \left(\frac{\Phi_{\text{ex}}}{2\Phi_0} \right) \cos \left(\frac{\phi}{\Phi_0} \right). \quad (3.34)$$

The conjugate momentum for ϕ is $q = C_J \dot{\phi}$ and the Hamiltonian becomes [31]

$$\mathcal{H} = \frac{q^2}{2C_J} - E_J(\Phi_{\text{ex}}) \cos \left(\frac{\phi}{\Phi_0} \right), \quad (3.35)$$

where we defined the external magnetic flux dependent Josephson energy $E_J(\Phi_{\text{ex}}) = E_J \cos(\Phi_{\text{ex}}/(2\Phi_0))$. Thus we can change magnitude of the potential energy by changing the external flux. This feature is of great importance for flux qubits as will become clear in [sub-Sec. 3.4.2](#).

What makes this qubit a transmon qubit is actually the ratio between the so called charging energy $E_C = e^2/(2C_J)$, i.e. the energy of charging the capacitor of the junction by a single electron, and the Josephson energy [31]. For a transmon the potential energy term E_J dominates, $E_J/E_C \gg 1$. Due to this condition the expectation value of the flux variable will be always close to zero. Now we can quantize the circuit using the normal commutation relation [Eq. \(3.24\)](#) because the lowest states do not feel the periodicity of the potential. We introduce the dimensionless variables $\varphi = \phi/\Phi_0$ and $n = q/(2e)$, $[\varphi, n] = i$, so that the quantized Hamiltonian reads

$$H = 4E_C n^2 - E_J \cos \varphi. \quad (3.36)$$

The wave functions of the few lowest states of the transmon and the potential are plotted in [Fig. 3.3](#) for $E_J/E_C = 70$. Because of the condition $E_J/E_C \gg 1$ the lowest states of the transmon can be described by expanding the cosine term up to fourth order resulting in a spectrum of a anharmonic oscillator. In this approximation the splitting between the two lowest states $\hbar\omega_q = E_1 - E_0$ and the anharmonicity $\hbar\alpha = E_2 - 2E_1 + E_0$ can be shown to be given by [31]

$$\hbar\omega_q = \sqrt{8E_C E_J} - E_C, \quad (3.37)$$

$$\hbar\alpha = -E_C. \quad (3.38)$$

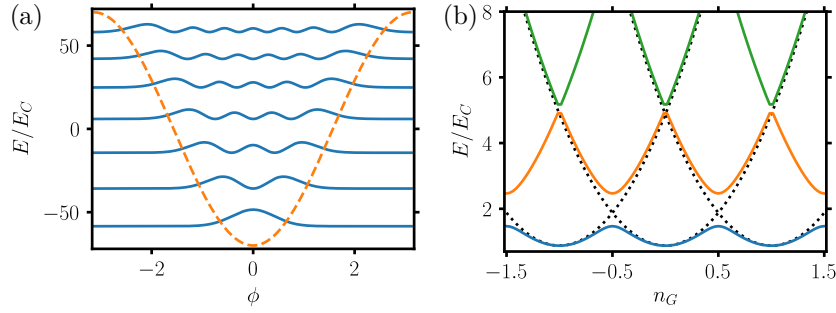


Figure 3.3: (a) Few of the lowest eigenstates of a transmon qubit in the cosine potential. (b) Eigenvalues of the CPB plotted against the gate charge n_G . The black dotted lines indicate the bare charge states without the cosine tunnelling term.

For USC purposes the transmon is not ideal since it does not allow to use the two-level-approximation for large couplings due to the lack of a large positive anharmonicity. Also the capacitive coupling between transmons and LC oscillators and the near harmonicity of the spectrum restrict the achievable coupling rates as will be shown in [sub-Sec. 3.5.1](#).

The above treatment was done in the flux, i.e. position, eigenbasis. It is also instructive to consider it in the basis of the charge eigenstates. Since $q = -i\hbar d/(d\phi)$ the eigenstates will be plane waves $\psi_Q(\phi) = e^{i\phi Q/\hbar}$. Operating on this eigenstate with the Hamiltonian of [Eq. \(3.35\)](#) gives

$$H\psi_Q(\phi) = \psi_Q(\phi) \left[\frac{Q^2}{2C_J} - \frac{E_J(\Phi_{\text{ex}})}{2} (e^{i2e\phi/\hbar} + e^{-i2e\phi/\hbar}) \right]. \quad (3.39)$$

We have three terms in the expression: the first one is just the original eigenstate multiplied by the eigenvalue Q from the q^2 operator. The last two terms include new charge eigenstates where the charge has changed by $\pm 2e$, from the $\cos(\phi)$ operator. We see, thus, that the cosine term moves a charge of $2e$, i.e. a Cooper pair, across the junction. Thus we need to consider only states which contain an integer number of Cooper pairs. This means that the dimensionless operator $n = q/(2e)$ only has integer eigenvalues and in this basis we can write [\[25\]](#)

$$H = \sum_{n=-\infty}^{\infty} 4E_c n^2 |n\rangle \langle n| - \frac{E_J(\Phi_{\text{ex}})}{2} (|n\rangle \langle n-1| + |n\rangle \langle n+1|). \quad (3.40)$$

This form gives us also the interpretation of n as the number of Cooper pairs in the island.

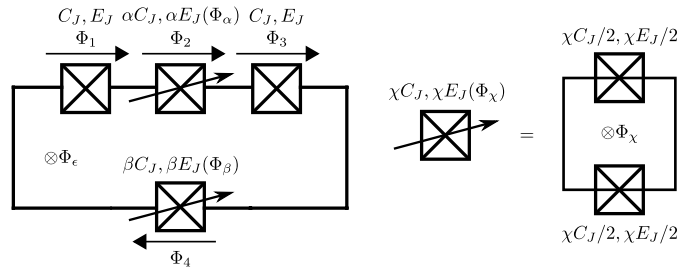


Figure 3.4: A tunable 4-junction flux qubit. Two of the Josephson junctions are replaced with a SQUID to allow the tuning of the Josephson energy as explained in [sub-Sec. 3.4.1](#).

Above we took the Josephson energy E_J to be much larger than the charging energy E_C , $E_J/E_C \ll 1$. This resulted in the weakly harmonic transmon qubit. In the opposite regime where the cosine potential can be considered as a weak perturbation on top of the kinetic energy $E_J/E_C < 1$ the circuit behaves as a *Cooper pair box* (CPB) [86]. By adding a possibility to bias the qubit as in [Fig. 3.2\(b\)](#) with an external voltage V_G , called the gate voltage, the Hamiltonian in the charge basis reads [25]

$$H = \sum_{n=-\infty}^{\infty} 4E_c (n + n_G)^2 |n\rangle \langle n| - \frac{E_J(\Phi_{\text{ex}})}{2} (|n\rangle \langle n-1| + |n\rangle \langle n+1|), \quad (3.41)$$

where $n_G = C_J V_G / (2e)$ is the gate voltage in units of Cooper pairs and the charging energy now includes the gate capacitor C_g , $E_C = e^2 / (C_J + C_g)$. Now by tuning n_G appropriately we can tune two charge states n and $n+1$ to be degenerate by setting $n + n_G = -1/2$. At this charge degeneracy or “charge sweet spot” point the spectrum of the system consist of two nearly degenerate levels split by E_J due to the cosine term and all other charge states are far higher in energy, see [Fig. 3.3\(b\)](#). We have thus realized a two-level-system to a very good approximation. The draw back of the CPB is its sensitivity to fluctuations of the gate charge n_G [86]. The transmon on the contrary is immune to these fluctuations due to the smaller charging energy E_C so that the spectrum is not sensitive to the exact value of the gate charge [31].

3.4.2 Flux qubits

Flux-type qubits are less intuitive in their nature, but due to the laws of nature they are more useful in the experimental study of USC physics, as explained in

sub-Sec. 3.5.2. We will review the physics of the tunable 4-junction flux qubit [58]. It is not the simplest flux type qubit, but we will use it in [Chap. 7](#) so it is useful to introduce it now in detail.

The circuit diagram for a tunable 4-junction qubit is depicted in [Fig. 3.4](#). It is a 4-junction qubit [34] where two of the junctions have been replaced by a SQUID. There are, thus, six junctions in the qubit. Two of them have capacitances C_J and Josephson energies E_J . For the SQUIDS the capacitances and Josephson energies are scaled, pairwise, by factors of α and β compared to the single junctions, see [Fig. 3.4](#). The self-inductance of the wires are neglected since they are much smaller than the Josephson inductances L_J . The three loops give us three flux-quantization conditions:

$$\sum_{i=1}^4 \Phi_i = \Phi_\epsilon, \quad (3.42)$$

$$\sum_{i=2,6} \Phi_i = \Phi_\alpha, \quad (3.43)$$

$$\sum_{i=4,5} \Phi_i = \Phi_\beta, \quad (3.44)$$

where Φ_X , $X \in \{\epsilon, \alpha, \beta\}$ are the external fluxes threading the big loop and the smaller SQUID loops, respectively. We use these equations to eliminate the fluxes Φ_2 , Φ_5 and Φ_6 . Let us introduce the dimensionless phases $\varphi_i = \Phi_i/\Phi_0$ and external magnetic fluxes $f_X = \Phi_X/\Phi_0$ for convenience. The potential energy for the tunable 4-junction qubit then reads

$$\begin{aligned} E_{\text{pot}} &= -E_J \left[\cos(\varphi_1) + \frac{\alpha}{2} \cos(\varphi_1 + \varphi_3 + \varphi_4 - f_\epsilon) + \frac{\alpha}{2} \cos(\varphi_1 + \varphi_3 + \varphi_4 - f_\epsilon + f_\alpha) \right. \\ &\quad \left. + \cos(\varphi_3) + \frac{\beta}{2} \cos(\varphi_4) + \frac{\beta}{2} \cos(\varphi_4 - f_\beta) \right], \\ &= -E_J \left[\cos(\varphi_1) + \alpha \cos\left(\frac{f_\alpha}{2}\right) \cos(\varphi_1 + \varphi_3 + \tilde{\varphi}_4 - \tilde{f}_\epsilon) + \cos(\varphi_3) \right. \\ &\quad \left. + \beta \cos\left(\frac{f_\beta}{2}\right) \cos(\tilde{\varphi}_4) \right], \end{aligned} \quad (3.45)$$

where $\tilde{f}_\epsilon = f_\epsilon + (f_\beta - f_\alpha)/2$ and we have defined a displaced phase jump variable $\tilde{\varphi}_4 = \varphi_4 - f_\beta/2$. This does not effect the kinetic energy, which is given by

$$E_{\text{kin}} = \frac{C_J \dot{\Phi}_1^2}{2} + \frac{\alpha C_J}{2} (\dot{\Phi}_1 + \dot{\Phi}_3 + \dot{\Phi}_4)^2 + \frac{C_J \dot{\Phi}_3^2}{2} + \frac{\beta C_J \dot{\Phi}_4^2}{2}. \quad (3.46)$$

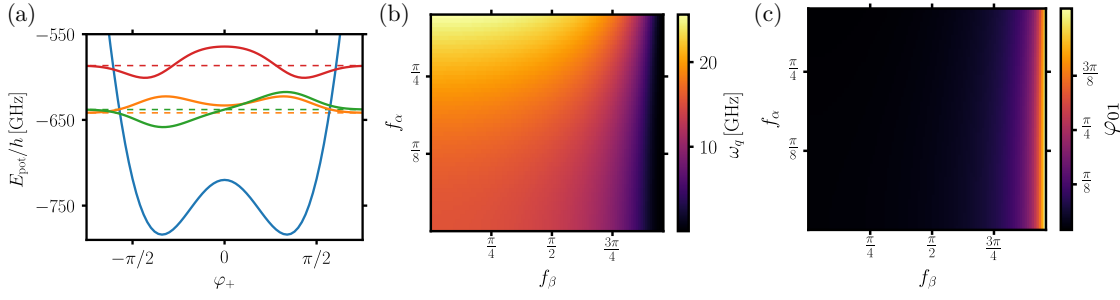


Figure 3.5: Properties of the tunable 4-junction flux qubit. (a) The double well potential of the qubit along a direction φ_+ defined in the text, and the wave functions of the three lowest eigenstates. (b) Frequency of the qubit transition $\omega_q \equiv \omega_{01}$ of the qubit as a function of the external fluxes f_α, f_β . (c) Matrix element of φ_4 between the two lowest eigenstates $\varphi_{01} = \langle 1|\tilde{\varphi}_4|0\rangle$ as a function of the external fluxes f_α, f_β . We have used $E_J/E_C = 50$, $E_J = 300\text{GHz}$, $\tilde{f}_\epsilon = \pi$, $\alpha = 0.6$ for (a-c), and $f_\alpha = f_\beta = 0$, $\beta = 1$ for (a) and $\beta = 6$ for (b,c).

From this we can calculate the kinetic energy as a function of the conjugate charges $\mathbf{q} = \mathcal{C}\tilde{\Phi}$ by inverting the capacitance matrix \mathcal{C} , see Eq. (3.21). We obtain

$$E_{\text{kin}} = \frac{4E_C}{\alpha + \beta + 2\alpha\beta} \left[(\alpha + \beta + \alpha\beta) (n_1^2 + n_3^2) + (1 + 2\alpha) n_4^2 - 2\alpha\beta n_1 n_3 - 2\alpha (n_1 + n_3) n_4 \right], \quad (3.47)$$

where we have introduced the dimensionless variables $n_i = q_i/(2e)$ and the charging energy $E_C = e^2/(2C_J)$. The Hamiltonian operator is then the sum of the kinetic and potential energies [42]

$$H = \frac{4E_C}{\alpha + \beta + 2\alpha\beta} \left[(\alpha + \beta + \alpha\beta) (n_1^2 + n_3^2) + (1 + 2\alpha) n_4^2 - 2\alpha\beta n_1 n_3 - 2\alpha (n_1 + n_3) n_4 \right] - E_J \left[\cos(\varphi_1) + \cos(\varphi_3) + \alpha \cos\left(\frac{f_\alpha}{2}\right) \cos(\varphi_1 + \varphi_3 + \tilde{\varphi}_4 - \tilde{f}_\epsilon) + \beta \cos\left(\frac{f_\beta}{2}\right) \cos(\tilde{\varphi}_4) \right], \quad (3.48)$$

where φ_i and n_i are operators satisfying the commutation relation Eq. (3.25).

The few lowest eigenstates of the 4-junction flux qubit along with the potential are plotted in Fig. 3.5(a). The coordinate in the plot is the eigenvector of the largest eigenvalue of the capacitance matrix \mathcal{C} [34]. Along the two other orthogonal directions the potential has a single well located at the origin. It is evident that the spectrum of the qubit is highly anharmonic, and the anharmonicity being positive,

i.e. $\hbar\alpha = E_2 - 2E_1 + E_0 > 0 \gg E_1 - E_0 = \hbar\omega_q$. This is an important property to be useful in USC experiments.

In the later chapters these types of qubits will be coupled to LC oscillators. The coupling is usually obtained by embedding a junction into the wire of the LC circuit [39, 41]. We will use a configuration where one of the junctions of the SQUID with junctions of size β is shared between the resonator and the qubit. In this case the coupling will happen through the flux jump related to the junction in question, in our notation $\tilde{\varphi}_4$. In Fig. 3.5(c) we plot the matrix element of $\tilde{\varphi}_4$ between the qubit levels 0 and 1, φ_{01} , as a function of the flux through the α and β SQUID-loops $f_{\alpha/\beta}$, respectively. The coupling will be directly proportional to φ_{01} . For $f_\beta \ll 1$ the matrix element is small and, thus, also the coupling of the qubit to a resonator would be small. When f_β gets close to π the matrix element starts to grow rapidly and approaches $\pi/2$. The dependence on f_α is weaker, but larger values of it do decrease the matrix element a small amount. The value is understood as half the distance between the double well minima in the $\tilde{\varphi}_4$ direction. In electric engineering terms, for small f_β the size of the SQUID-junction is largest and, thus, the inductance of the SQUID is small, $L \propto \beta_{\text{eff}}^{-1}$. Current can flow through the SQUID easily making the flux difference small. When the external flux is increased towards π the effective size gets smaller and smaller, thus increasing the inductance and making the current smaller and increasing the flux jump.

In Fig. 3.5(b) we also plot the qubit frequency ω_q as a function of f_α and f_β . The tendency of ω_q is inverse to that of the coupling. For small f_β we obtain the largest qubit frequency and for fluxes close to $f_\beta = \pi$ it reaches its lowest values. The reason for this change is that by tuning the magnetic flux we can only change the effective Josephson energy of the SQUID-loop *not* the charging energy E_C . Thus, the potential energy changes while the kinetic energy stays the same which leads to the observed change in the qubit frequency.

3.5 Circuit quantum electrodynamics

In this section we present the two main coupling schemes used to couple SC qubits to microwave modes, capacitive and inductive coupling. We will go through a simple example circuit for the two schemes and give limits to the coupling strength in limiting cases of two coupled harmonic oscillators and ideal charge and flux qubits.

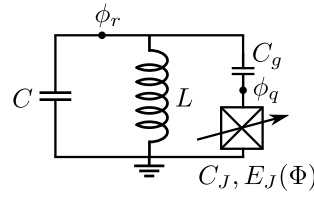


Figure 3.6: A transmon qubit capacitively coupled to an LC -circuit. We use the same circuit diagram for the tunable junction as in Fig. 3.4.

3.5.1 Capacitive coupling

We will start by considering the capacitive coupling scheme. As the name suggest the SC qubits are coupled to the microwave mode(s) capacitively through a mutual capacitance. Normally coupling through a capacitance is used to couple charge qubits to microwave modes.

We consider the simple circuit of Fig. 3.6. A transmon qubit is coupled to a simple LC circuit through a capacitance C_g . We choose the dynamical variables as depicted in the figure: ϕ_r is the time-integrated voltage over the resonators capacitance, C_r . Correspondingly ϕ_q is the generalised flux related to the transmon's Josephson junction. Since there are no closed loops in the circuit we do not need to worry about the flux quantization condition. The Lagrangian of the circuit reads

$$\mathcal{L} = \frac{C_r \dot{\phi}_r^2}{2} - \frac{\phi_r^2}{2L_r} + \frac{C_J \dot{\phi}_q^2}{2} + E_J \cos\left(\frac{\phi_q}{\Phi_0}\right) + \frac{C_g (\dot{\phi}_r - \dot{\phi}_q)^2}{2}. \quad (3.49)$$

The Hamiltonian is obtained then with the recipe of Sec. 3.1 and Sec. 3.2. The total Hamiltonian consist of three parts, the LC Hamiltonian H_r , free qubit Hamiltonian H_q and interaction Hamiltonian H_{int} , $H = H_r + H_q + H_{\text{int}}$. The three parts are given by

$$H_r = \frac{q_r^2}{2\tilde{C}_r} + \frac{\phi_r^2}{2L_r}, \quad (3.50)$$

$$H_q = \frac{q_q^2}{2\tilde{C}_J} - E_J \cos\left(\frac{\phi_q}{\Phi_0}\right), \quad (3.51)$$

$$H_{\text{int}} = \frac{q_r q_q}{\tilde{C}_g}. \quad (3.52)$$

The capacitive coupling leads to renormalization of all the capacitances $C_{r,J,g}$. The

renormalized capacitances are given by

$$\tilde{C}_r = \frac{\tilde{C}^2}{C_J + C_g}, \quad (3.53)$$

$$\tilde{C}_J = \frac{\tilde{C}^2}{C_r + C_g}, \quad (3.54)$$

$$\tilde{C}_g = \frac{\tilde{C}^2}{C_g}, \quad (3.55)$$

and $\tilde{C}^2 = C_g C_r + C_J(C_r + C_g)$.

Let us take a closer look at the coupling Hamiltonian. We can rewrite it in the form

$$H_{\text{int}} = \chi q_q \tilde{V}_r, \quad (3.56)$$

where $\chi = \tilde{C}_r / \tilde{C}_g = C_g / (C_J + C_g)$ and $\tilde{V}_r = Q_r / \tilde{C}_r$ is proportional to the resonator voltage. For an uncoupled oscillator it would be the voltage, but the coupling to the qubit changes the situation [51]. In this form we see that the coupling is of the same type as in cavity QED: the dipole moment of the qubit, the charge q , couples to the electric field of the mode, the resonator “voltage” \tilde{V}_r .

Introducing the raising and lowering operators for the LC resonator and making a two-level-approximation for the qubit we can write the free qubit and resonator Hamiltonians as

$$H_r = \hbar \tilde{\omega}_r a^\dagger a, \quad (3.57)$$

$$H_q = \frac{\hbar \tilde{\omega}_q}{2} \sigma^z, \quad (3.58)$$

where $\tilde{\omega}_r = 1/\sqrt{L_r \tilde{C}_r}$ and $\tilde{\omega}_q$ are the coupling renormalized oscillator and qubit frequencies, due to the capacitance renormalization. The qubit-resonator coupling becomes

$$H_{\text{int}} = \frac{\hbar g}{2} (a^\dagger + a) \sigma^x, \quad (3.59)$$

where $\hbar g = 2q_{\text{zpf}}^r q_{\text{zpf}}^q / \tilde{C}_g$ is the coupling and $q_{\text{zpf}}^{r,q}$ the zero point charge fluctuations of the resonator and two-level-system. We have included the factor of half for it is useful when dealing with systems of multiple qubits coupled to the oscillator.

The zero point fluctuation of charge for the resonator we have calculated already earlier and it is $q_{\text{zpf}}^r = \sqrt{\hbar/(2\tilde{Z})}$, where $\tilde{Z} = \sqrt{L_r/\tilde{C}_r}$ is the renormalized resonator impedance. For the qubit we define it to be $q_{\text{zpf}}^q = 2eq_q^{01}$, where

$q_q^{01} = \langle 1|q_q|0\rangle/(2e)$ is the matrix element of the transmon charge operator between the qubit levels 0 and 1. An important figure of merit in cavity and circuit QED for the strength of the coupling is the ratio of the coupling constant to the oscillator frequency $g/\tilde{\omega}_r$. For this configuration it is given by [28]

$$\frac{g}{\tilde{\omega}_r} = \frac{2q_{zpf}^r q_{zpf}^q}{\hbar\tilde{\omega}_r\tilde{C}_g} = \frac{2e}{\tilde{\omega}_r\tilde{C}_g} \sqrt{\frac{2}{\hbar\tilde{Z}_r}} q_q^{01} = 2\sqrt{\frac{\pi Z_r}{R_Q}} \sqrt{\frac{C_r\tilde{C}_r^3}{\tilde{C}_g^4}} q_q^{01}, \quad (3.60)$$

where we have used $(\omega_r\sqrt{Z_r})^{-1} = C_r\sqrt{Z_r}$, ω_r and Z_r are the bare resonator frequency and impedance, respectively, and introduced the *Quantum resistance* $R_Q = h/(2e)^2 \approx 6453 \Omega$.

The frequency normalized coupling depends on three parts: there is a geometrical factor coming from the capacitances $\sqrt[4]{C_r\tilde{C}_r^3/\tilde{C}_g^4}$, which depends just on the ratios of the capacitances, it is limited from above by $C_r/(C_r + C_J) < 1$ and saturates this bound when the coupling capacitance C_g is the largest capacitance in the system. Then there is the qubit dependent part q_q^{01} which varies depending on the charge qubit type. We will come back to this shortly. Lastly there is the coupling method dependent part $\sqrt{\pi Z_r/R_Q}$. For the capacitive coupling scheme it scales with the root of the impedance due to the qubit coupling to the electric field, i.e. to the “voltage” of the resonator. Dividing this by the *LC* frequency gives the impedance. Thus reaching large coupling strengths requires *LC* resonators with impedances on the order of the quantum resistance R_Q . It turns out this is hard to achieve using geometrical capacitances and inductances. Stray capacitances in inductors tend to lower the value of the impedance to few tens or hundreds Ohm’s. In experiments oscillators with impedance $Z \sim 50 \Omega$ are usually deployed due to the availability of commercial coaxial cables in this impedance range. For this typical value of the impedance the coupling type dependent factor gives $\sqrt{\pi 50 \Omega/R_Q} \approx 0.156$. Thus, reaching extremely high values of $g/\tilde{\omega}_r$ is not trivial with capacitive coupling.

There are ways of manufacturing inductors where the inductance is in the order R_Q , so called “superinductors” [32, 87, 88]. These superinductors take advantage of linear arrays of Josephson junctions operated in a regime where the current through the array is extremely low compared to the critical current I_c , i.e. $I = I_c \sin(\Phi/\Phi_0) \ll I_c$, such that the sine term is, to a very good approximation, given by the lowest order Taylor expansion Φ/Φ_0 , rendering a linear behaviour, with inductance $L_J = \Phi_0/I_c$. In this case the Josephson inductance can be made very large without increasing the capacitance of the junction too much, yielding very high impedances. The draw back of this method is of course that the linear behaviour is just an approximation and there are also other modes in the Josephson junction array which might spoil the single mode behaviour of the system.

Let us come back to the qubit dependent part of the coupling q_q^{01} . For a transmon qubit, deep in the $E_J/E_C \ll 1$ regime, it would be approximately given by the harmonic oscillator charge zero point fluctuation $q_{zpf}^q = 2eq_q^{01} = \sqrt{\hbar\tilde{\omega}_q\tilde{C}_J}/2$ which depends on the qubit frequency. For a Cooper pair box qubit the charge matrix element is given by $q_q^{01} = 1/2$ and is roughly independent of the qubit frequency $\tilde{\omega}_q = E_J$. Another important figure of merit for the coupling strength is the combination

$$\zeta = \frac{g^2}{\tilde{\omega}_r\tilde{\omega}_q}. \quad (3.61)$$

For reasons that will become clear in [Chap. 4](#) the value of $\zeta = 1$ is regarded as the threshold for USC. Evaluating this parameter for the transmon gives [\[50, 68\]](#)

$$\zeta = \frac{2q_{zpf}^r q_{zpf}^q}{\tilde{C}_g} = \frac{\tilde{C}_J\tilde{C}_r}{\tilde{C}_g^2} = \frac{C_g^2}{(C_r + C_g)(C_J + C_g)} < 1. \quad (3.62)$$

Thus, with a weakly anharmonic qubit it is not possible to reach the USC threshold of one. This is of course due to the fact that the charge zero point fluctuation terms in g scale as $\sqrt{\tilde{\omega}_r/q}$. Instead for the Cooper pair box we obtain the relation [\[35, 50\]](#)

$$\zeta = \frac{\tilde{C}_J\tilde{C}_r}{\tilde{C}_g} \frac{4E_C}{E_J} = \frac{C_g^2}{(C_r + C_g)(C_J + C_g)} \frac{4E_C}{E_J}, \quad (3.63)$$

where $E_C = e^2/(2\tilde{C}_J)$ is the renormalized charging energy. The ζ parameter is enhanced by a factor of $4E_C/E_J$ compared to the transmon and can in principle have an arbitrary large value.

Let us make another note on the resonator frequency normalized coupling constant. It is easy to see that

$$\frac{g}{\tilde{\omega}_r} = \frac{2q_{zpf}^r q_{zpf}^q}{\hbar\tilde{\omega}_r\tilde{C}_g} = \frac{\tilde{C}_r}{\tilde{C}_g} \frac{q_{zpf}^q}{q_{zpf}^r} \leq \frac{q_{zpf}^q}{q_{zpf}^r}, \quad (3.64)$$

as follows from the definitions of \tilde{C}_r and \tilde{C}_g . Thus, the renormalized coupling strength depends on the size of the qubit induced charge on the resonator compared to the zero-point fluctuations of the oscillators charge. The typical q_{zpf}^r exceed the elementary charge by almost an order of magnitude, limiting the obtainable coupling strengths. High impedance resonators have $q_{zpf}^r \sim e$ such that the bound is increased to allow for larger couplings.

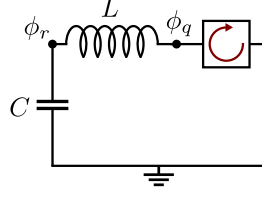


Figure 3.7: A 4-junction flux qubit inductively coupled to an LC -resonator. We use the box and arrow to represent the whole 4-junction flux qubit circuit diagram Fig. 3.4.

3.5.2 Inductive coupling

The second coupling scheme we review is the inductive coupling. In this situation the coupling element between the LC circuit and the qubit will be an inductor. Inductive coupling is used as a means to couple flux qubits to microwave resonances. In earlier works coupling between the qubit and to resonator was achieved through a mutual inductance. This is not as effective as sharing an inductor between the qubit and oscillator as we will present in the following.

The circuit we analyse is presented in Fig. 3.7. A tunable 4-junction flux qubit is coupled to an LC oscillator through its inductance L_r . The Lagrangian of the circuit becomes

$$\mathcal{L} = \frac{C_r \dot{\phi}_r^2}{2} - \frac{(\phi_r - \phi_q)^2}{2L_r} + \mathcal{L}_{4\text{jfq}}, \quad (3.65)$$

where $\mathcal{L}_{4\text{jfq}}$ is the 4-junction flux qubit Lagrangian and we have used ϕ_q for the flux $\tilde{\phi}_4$. Since this circuit does not involve any shared capacitances the derivation of the Hamiltonian is simple. We obtain

$$H = \frac{q_r^2}{2C_r} + \frac{\phi_r^2}{2L_r} + \tilde{H}_q + \frac{\phi_r \phi_q}{L_r}, \quad (3.66)$$

where $\tilde{H}_q = H_{4\text{jfq}} + \phi_q^2/(2L_r)$, $H_{4\text{jfq}}$ is the bare 4-junction qubit Hamiltonian, Eq. (3.48).

Let us now take a closer look at the coupling Hamiltonian

$$H_{\text{int}} = \frac{\phi_r \phi_q}{L_r} = \phi_q I_r. \quad (3.67)$$

We have introduced the resonator current operator $I_r = \phi_r/L_r$. It does not, however, correspond to the current flowing through the inductor L_r , which is given by $(\phi_r - \phi_q)/L_r$. This is an important fact to remember when interpreting

what a non-zero value of I_r means in terms of physical currents. The coupling is of the type magnetic field coupled to the magnetic dipole moment $B_r\mu$. In our case $I_r \propto B_r$ and $\phi_q \sim \mu$.

Let us introduce the dimensionless operators $a^{(\dagger)}$ for the oscillator as in [sub-Sec. 3.5.1](#) and use a two-level-approximation for the qubit. Using these variables the resonator Hamiltonian is given by $H_r = \hbar\omega_r a^\dagger a$, where $\omega_r = 1/\sqrt{L_r C_r}$ is the bare resonator frequency, i.e. there is no renormalization of the oscillator energy in this case. The qubit frequency is renormalized, due to the inclusion of the term $\phi_q^2/(2L_r)$, to the qubit Hamiltonian to $\tilde{\omega}_q$. The interaction Hamiltonian becomes

$$H_{\text{int}} = \frac{\hbar g}{2}(a^\dagger + a)\sigma^x, \quad (3.68)$$

where $\hbar g = 2\phi_{\text{zpf}}^r \phi_{\text{zpf}}^q / L_r$ is the coupling constant and we have included the factor of half, as in [sub-Sec. 3.5.1](#), for later convenience. The resonator zero-point flux fluctuations are given by $\phi_{\text{zpf}}^r = \sqrt{\hbar Z_r / 2}$ and for the qubit we use $\phi_{\text{zpf}}^q = \Phi_0 \varphi_{01}$, where $\varphi_{01} = \langle 1 | \phi_q / \Phi_0 | 0 \rangle$, analogously to [sub-Sec. 3.5.1](#).

Again we are interested in how the coupling constant g between the oscillator and the qubit scales with the system parameters, especially we take interest in the two parameter ratios g/ω_r and $g^2/(\omega_r \tilde{\omega}_q)$. Let us evaluate first the oscillator frequency normalized coupling constant

$$\frac{g}{\omega_r} = \frac{2\phi_{\text{zpf}}^q \phi_{\text{zpf}}^r}{\hbar\omega_r L_r} = \sqrt{\frac{2Z_r}{\hbar}} \frac{\Phi_0}{\omega_r L_r} \varphi_{01} = \sqrt{\frac{R_Q}{\pi Z_r}} \varphi_{01}, \quad (3.69)$$

where we have used $\sqrt{Z_r}/\omega_r = L_r/\sqrt{Z_r}$. In contrast to the capacitive coupling situation the dependence on the coupling type dependent factor is inverted to $\sqrt{R_Q}/(\pi Z_r)$. This gives a much more favourable scaling with Z_r regarding high coupling strengths. This factor alone for a typical resonator impedance of $Z_r = 50 \Omega$ is given by $\sqrt{R_Q}/(\pi 50 \Omega) \approx 6.41$ a very large value indeed (the inverse of this is ~ 0.16 , so an increase of a factor of 40). There is no geometrical factor in the qubit-resonator coupling in this case, but we will encounter also situations where one exists, see [Sec. 4.3](#). It will depend only on ratios of inductances in the system analogously to [sub-Sec. 3.5.1](#) where the geometric factor depended only on the capacitive elements. A geometric factor would be present e.g. when the coupling to the qubit does not happen through the resonator inductance, but a dedicated inductance [\[50\]](#). These types of factors can again be made at most of order one, as in the capacitive coupling case [\[50\]](#). The inverted scaling of the coupling constant can be understood from $I_r/\omega_r \propto 1/\sqrt{Z_r}$. Next we will consider the qubit dependent factor φ_{01} .

As explained in [sub-Sec. 3.4.2](#) the matrix element of the flux is given by half the distance between the two minima in the qubit potential landscape. For the

4-junction qubit it can be up to $\varphi_{01} = 1/2$, and for a flux qubit with almost a harmonic spectrum it would be given by the same expression as for the resonator. Thus, for a nearly harmonic qubit we obtain the bound

$$\zeta = \frac{g^2}{\omega_r \tilde{\omega}_q} \leq 1, \quad (3.70)$$

as we derived earlier for the capacitive coupling. For the anharmonic qubit the qubit frequency and the matrix element are not correlated like for the harmonic qubit and the bound of one can be broken. There is no simple expression for $\tilde{\omega}_q$ for the 4-junction qubit so we cannot write down a simple expression like we did for the capacitive coupling to a CPB.

In a similar manner to [sub-Sec. 3.5.1](#) we can derive a bound for the oscillator frequency normalized coupling strength

$$\frac{g}{\omega_r} = \frac{2\phi_{\text{zpf}}^r \phi_{\text{zpf}}^q}{\hbar \omega_r L_r} \leq \frac{\phi_{\text{zpf}}^q}{\phi_{\text{zpf}}^r}, \quad (3.71)$$

in complete analog to the capacitive coupling situation. The set up of [Fig. 3.7](#) saturates this bound, and any geometrical factors will only reduce the coupling. It is a coincidence that the flux quantum is very large compared to the zero-point flux fluctuations of typical electric circuits, yielding a large value for this bound.

It is interesting that the coupling to the magnetic field of the resonator can give a stronger coupling than coupling to the electric field. In experiments with real atoms instead of artificial ones, we are used to the situation that electric coupling dominates over the magnetic one unless some symmetries protect the atom against coupling to the electric field.

Chapter 4

Models of ultra-strong light-matter coupling

In this chapter we discuss the models of ultra-strong light-matter coupling. We begin by introducing the conventional models used in the literature, the Rabi and Dicke models. Then we show, with explicit examples, that the correct description of USC systems is given by the Extended Dicke model (EDM). This is done by carefully analyzing a generic light-matter system and proving that the EDM is the only model consistent with the two-level-approximation widely used in cavity/circuit QED.

4.1 Rabi model

The simplest model used to describe ultra-strongly coupled systems is the *Rabi model* [89, 90], or more correctly the quantum Rabi model. We will, however, use just Rabi model for brevity. It describes systems with a single mode ultra-strongly coupled to a two-level-atom. The Hamiltonian of the Rabi model is given by

$$H_{\text{rabi}} = \hbar\omega_r a^\dagger a + \frac{\hbar\omega_q}{2} \sigma^z + \frac{\hbar g}{2} (a^\dagger + a) \sigma^x, \quad (4.1)$$

where $a^{(\dagger)}$ is the annihilation (creation) operator of the field mode and σ^α , $\alpha = x, y, z, +, -$, are the Pauli matrices. For couplings in the strong coupling regime a RWA can be made and the “counter-rotating” terms, $a\sigma^-$, $a^\dagger\sigma^+$, of the interaction $(a^\dagger + a)\sigma^x$ can be dropped. In this case the Rabi model reduces to the Jaynes-Cummings model [91]. The full dipole interaction of the Rabi Hamiltonian, a small change in principle, makes the system however much more complicated. It is still exactly solvable, like the JC model, but the analytic solution was found only recently [92]. The reason is the lower symmetry of the Rabi Hamiltonian. The

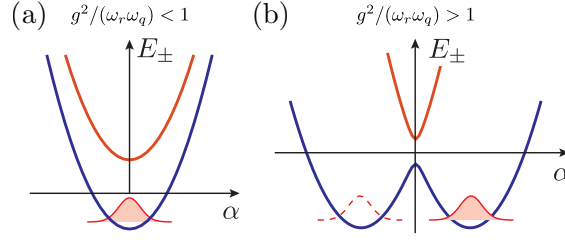


Figure 4.1: Effective potentials formed by the qubit for the resonator. In the semiclassical approximation the operator a can be replaced by a c-number α , which can be chosen real. The plotted curves E_{\pm} are the eigenvalues of the semiclassical Rabi Hamiltonian $H_{\text{Rabi}}(\alpha)$ as a function of α . (a) When $g^2 < \omega_r \omega_q$ the potentials only have a single minimum at $\alpha = 0$. (b) For $g^2 > \omega_r \omega_q$ the ground state potential curve develops a double-well structure with minima at $\alpha \neq 0$.

JC Hamiltonian has a continuous $U(1)$ symmetry compared to the \mathbb{Z}_2 symmetry of the Rabi Hamiltonian, corresponding to flipping the sign of $a^\dagger + a$ and σ^x simultaneously.

Now let us consider the ground state of the system in the ultra-strong coupling regime, $g/\omega_r, g^2/(\omega_r \omega_q) > 1$. Let us for simplicity at first set $\omega_q = 0$. Then the Rabi Hamiltonian can be diagonalized by the *polaron transformation* $\mathcal{U} = \exp[g(a^\dagger - a)\sigma^x/\omega_r]$, explained in detail in [App. A](#), which displaces the oscillator by a TLS-state dependent amount. The ground state of the system is doubly degenerate and the states are given by [\[45, 46\]](#)

$$|G_{\pm}\rangle = \frac{1}{\sqrt{2}} (|\leftarrow\rangle |\alpha\rangle \pm |\rightarrow\rangle |-\alpha\rangle) = \frac{1}{\sqrt{2}} (|\uparrow\rangle |\mathcal{C}_+(\alpha)\rangle \pm |\downarrow\rangle |\mathcal{C}_-(\alpha)\rangle), \quad (4.2)$$

where \leftarrow / \rightarrow and \uparrow / \downarrow refer to the σ^x and σ^z eigenstates, respectively, $|\beta\rangle$ is a coherent state of amplitude β and $|\mathcal{C}_{\pm}\rangle(\beta) = N_{\pm}^{-1}(|\beta\rangle \pm |-\beta\rangle)$ is a *Cat-state* of amplitude β . The normalization constants N_{\pm} are close to $1/\sqrt{2}$ for $\beta \gg 1$. A finite qubit frequency ω_q induces transitions between the two states and lifts the degeneracy. These solutions become possible classical ground states after $g^2/(\omega_q \omega_r) = 1$. Before this point the energy is always minimized by a wave function of the photons centred at $\alpha = 0$. In [Fig. 4.1](#) we show the effective potential created by the TLS's for the photons, see [Chap. 6](#). Below $g^2/(\omega_q \omega_r) = 1$ the effective potential has a single global minimum located at $\alpha = 0$. For $g^2/(\omega_q \omega_r) > 1$ the potential has two degenerate minima at a finite $\alpha \neq 0$. Due to quantum tunnelling through the barrier, driven by σ^z , the ground state is the superposition of the classical states centred in these minima, [Eq. \(4.2\)](#). The formation of these states is a precursor of the *superradiant phase transition* (SRPT) observed in the Dicke model, see [Sec. 4.2](#).

This analysis explains the boundary $g^2/(\omega_q\omega_r) = 1$ used for USC regime: the formation of new classical stable points in the phase space. For $g/\omega_r > 1$ the two coherent states in Eq. (4.2), $|\pm\beta\rangle$, are well separated and almost orthogonal.

4.2 The Dicke model

The Rabi model is a description of a single emitter coupled to a field. For multiple non-interacting emitters coupled to a single field mode the standard description is the Dicke model [35, 36]. It is a simple generalization of the Rabi model to N TLS's coupled to an oscillator. The Hamiltonian is given by

$$H_{\text{DM}} = \hbar\omega_r a^\dagger a + \hbar\omega_q S_z + \hbar g(a^\dagger + a)S_x, \quad (4.3)$$

where $S_x = \sum_{i=1}^N \sigma_i^x/2$ are collective spin operators. The model is named after R. Dicke, who studied in his seminal work collective effects in dense clouds of atoms emitting radiation [93]. He found that when the atomic cloud is prepared, e.g., with a single excitation, and the inter-particle spacings are smaller than the wavelength of the emitted radiation, the decay rate of the excitation is enhanced by the number of atoms from Γ to $N\Gamma$. This happens due to correlations building up between the emitting atoms. Enhancement factors that scale with N^2 are achievable, by preparing states near the equator of the Bloch-sphere of the atoms, e.g. a σ^x polarized state [94, 95].

The Dicke model has a \mathcal{Z}_2 symmetry like the Rabi model. The symmetry is reflected in the eigenstates as having a definite parity defined through (below the critical coupling introduced below) [35, 36]

$$\mathcal{P} = \exp \left[i\pi \left(a^\dagger a + S_z + \frac{N}{2} \right) \right]. \quad (4.4)$$

The RWA version of the DM is called the Tavis-Cummings (TC) model [96]. Analogously to the JC model the TC model is obtained from the Dicke model by neglecting the CR terms in the interaction Hamiltonian

$$H_{\text{TC}} = \hbar\omega_r a^\dagger a + \hbar\omega_q S_z + \frac{\hbar g}{2}(a^\dagger S_- + a S_+). \quad (4.5)$$

4.2.1 Superradiant phase transition

The Dicke Hamiltonian supports two distinct ground states as a function of the collective coupling strength $G = \sqrt{N}g$ [35, 36]. For weak coupling the ground state respects the \mathcal{Z}_2 symmetry and has, accordingly, $\langle a \rangle = \langle S_x \rangle = 0$. For large coupling the ground state breaks this symmetry. This allows for the system to be

in states for which $\langle a \rangle \neq 0$ and $\langle S_x \rangle \neq 0$. The transition to this symmetry broken regime is called the superradiant phase transition [47, 48].

The transition point can be obtained in multiple ways. We use here the equations of motion (e.o.m.). The e.o.m. for the field mode and the collective spin expectation values read [97]

$$\langle \dot{a} \rangle = -i\omega_r \langle a \rangle - i\frac{G}{2} \langle S_x \rangle, \quad (4.6)$$

$$\langle \dot{S}_x \rangle = -i\omega_q \langle S_y \rangle \quad (4.7)$$

$$\langle \dot{S}_y \rangle = i\omega_q \langle S_x \rangle - i\frac{G}{2} \langle (a^\dagger + a) S_z \rangle, \quad (4.8)$$

$$\langle \dot{S}_z \rangle = i\frac{G}{2} \langle (a^\dagger + a) S_y \rangle. \quad (4.9)$$

In the mean field description the expectation values of products of operators are factorized, e.g. $\langle a S_z \rangle \approx \langle a \rangle \langle S_z \rangle$. Using this approximation and solving for the steady-state of the the above equations gives

$$\langle a \rangle = \left(0, \pm \frac{G}{2\omega_r} \sqrt{1 - \left(\frac{G}{G_c} \right)^4} \right), \quad (4.10)$$

$$\langle S_x \rangle = \left(0, \mp \frac{G}{2\omega_r} \sqrt{1 - \left(\frac{G}{G_c} \right)^4} \right), \quad (4.11)$$

$$\langle S_y \rangle = (0, 0), \quad (4.12)$$

$$\langle S_z \rangle = \left(\pm \frac{N}{2}, 0 \right), \quad (4.13)$$

where the first, respectively second, elements in the parentheses denote the normal and superradiant phases. Of the two stationary states $\langle S_z \rangle = \pm N/2$ the state with a negative polarization is dynamically stable and the other unstable [97]. The superradiant states, $\langle a \rangle = \pm \frac{G}{2\omega_r} \sqrt{1 - \left(\frac{G}{G_c} \right)^4}$, become valid stationary points at the critical collective coupling [47, 48]

$$G > G_c = \sqrt{\omega_r \omega_q}, \quad (4.14)$$

or $g_c = \sqrt{\omega_q \omega_r / N}$ in terms of the single atom-photon coupling. Both of the possible solutions are dynamically stable [97]. The stationary points at $\langle S_z \rangle = \pm N/2$ survive in the superradiant phase, but are now both unstable fixed points [97]. The SRPT has been observed in driven-dissipative scenarios [98–101], but not as a standard ground state phase transition.

4.2.2 The A^2 -term and no-go theorems

The discussion of the SRPT was based on the DM Hamiltonian Eq. (4.3). Let us go back to the more fundamental Hamiltonian where it can be derived from. Our starting point is the Hamiltonian for N charged particles, with charge q and mass m , moving in one dimension in an electromagnetic (EM) field

$$H = \hbar\omega_r a^\dagger a + \sum_j \left[\frac{(p_j - qA)^2}{2m} + V(x_j) \right], \quad (4.15)$$

where $V(x)$ is an external potential confining the particles, $A = \mathcal{A}_0(a^\dagger + a)$ is the vector potential with zero-point amplitude \mathcal{A}_0 , $p - qA$ is the kinetic momentum and we have additionally used the dipole approximation $A(x) \approx A$ in the interaction of the field and the particle. Expanding the square of the kinetic momentum allows us to separate the Hamiltonian into three parts

$$H = \tilde{H}_{\text{mode}} + H_{\text{particle}} + H_{\text{int}}, \quad (4.16)$$

where

$$\tilde{H}_{\text{mode}} = \hbar\omega_r a^\dagger a + \frac{Nq^2 \mathcal{A}_0^2}{2m} (a^\dagger + a)^2, \quad (4.17)$$

$$H_{\text{particle}} = \frac{p^2}{2m} + V(x), \quad (4.18)$$

$$H_{\text{int}} = -\frac{q\mathcal{A}_0}{m} (a^\dagger + a)p. \quad (4.19)$$

The interaction with the particles renormalizes the bare Hamiltonian of the field by a term $\propto Nq^2 A^2$. This is the so called A^2 -term [59]. In the following we explore its consequences on the physics.

Let us start, however, by neglecting it altogether. This is a valid treatment if the coupling between the field and the particles, $\propto q\mathcal{A}_0$, is small since it appears quadratically in the A^2 -term. In the two-level-approximation (TLA) the full Hamiltonian H then reduces to the Hamiltonian of the DM. For large couplings also the A^2 -term becomes significant and it cannot be neglected anymore.

It is also possible to include the effect of the renormalization exactly. The modified field Hamiltonian can be diagonalized with a Bogoliubov-transformation [102, 103], resulting in a renormalized field mode frequency $\tilde{\omega}_r = \sqrt{\omega_r^2 + D^2}$ with $D^2 = 2Nq^2 \mathcal{A}_0^2 \omega_r / (\hbar m)$ [70]. Thus, the Hamiltonian in the two level description reduces again to that of the DM

$$H = \hbar\tilde{\omega}_r c^\dagger c + \hbar\omega_q S_z + \hbar\tilde{g}(c^\dagger + c)S_x, \quad (4.20)$$

where c are the new field operators and $\tilde{g} = g\sqrt{\omega_r/\tilde{\omega}_r}$ is the renormalized coupling. It can then be shown [59, 66, 70] that

$$\frac{\tilde{g}^2}{\omega_q \tilde{\omega}_r} < 1. \quad (4.21)$$

This means that the critical coupling of the Dicke model cannot be reached, such that the SRPT is not possible.

The above result is not the complete story though, as we show in Sec. 4.4. The no-go theorem does not hold in general for systems with non-convex potentials. The reason is the failure of the simple two-level-approximation we have used in this section in conjunction with the Coulomb gauge [70]. The qualitative result is, however, correct: for non-interacting TLSs interacting with a mode of the electromagnetic field there is no superradiant phase transition.

4.3 The Extended Dicke model

In the previous sections we have shortly reviewed the discussion on USC phenomena in the Rabi and Dicke models. For the rest of the chapter we focus on the *Extended Dicke model* [50, 51] which we develop in this section. We present the theory applied to superconducting circuits, but it is a more general theory applicable to all systems where a single EM mode is coupled to two-level-atoms, real or artificial [51]. We start by considering non-interacting qubits coupled to a mode of the electromagnetic field. Then we proceed to treat systems where the qubits additionally interact with each other through dipole-dipole couplings, either attractively or repulsively. An example circuit of each situation is given. Finally we show that the Dicke model does not give the correct description of USC light-matter systems.

4.3.1 Non-interacting qubits

Let us consider a system of comprising of an LC -resonator coupled to N superconducting charge qubits as presented in Fig. 4.2. In Chap. 3 we derived the Hamiltonian for a single charge qubit coupled to an LC -oscillator. The derivation for N qubits proceeds very much in the same manner, but with some important differences. The Lagrangian for the circuit is given by

$$\mathcal{L} = \frac{C_r \dot{\phi}_r^2}{2} - \frac{\phi_r^2}{2L_r} + \sum_{i=1}^N \left[\mathcal{L}_q(\phi_i, \dot{\phi}_i) + \frac{C_g}{2} (\dot{\phi}_r - \dot{\phi}_i)^2 \right], \quad (4.22)$$

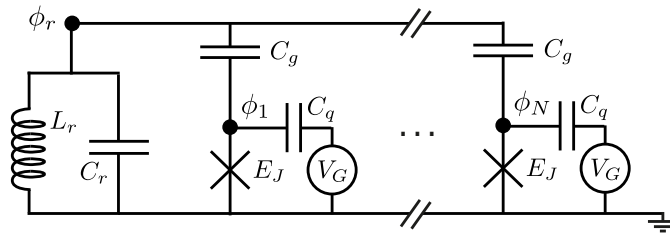


Figure 4.2: N charge qubits coupled to an LC resonator. The qubits can be CPB qubits or transmon qubits depending on the ratio chosen between E_C and E_J . The circuit is a prototype of non-interacting qubits coupled to a common resonator mode.

where the Lagrangian for a single qubit is given by

$$\mathcal{L}_q(\phi, \dot{\phi}) = \frac{C_q}{2}(\dot{\phi} - V_G)^2 + E_J \cos\left(\frac{\phi}{\Phi_0}\right). \quad (4.23)$$

Introducing the vector notation from Sec. 3.1 allows us to write the Hamiltonian of the circuit as

$$H = \frac{1}{2} \mathbf{q}^T \mathbf{C}^{-1} \mathbf{q} + E_{\text{pot}}(\phi_r, \{\phi_i\}) = H_r + \sum_i H_{q_i} + H_{\text{int}} + H_{qq}, \quad (4.24)$$

where the individual parts are given by

$$H_r = \frac{q_r^2}{2\tilde{C}_r} + \frac{\phi_r^2}{2L_r}, \quad (4.25)$$

$$H_{q_i} = \frac{\tilde{q}_i^2}{2\tilde{C}_q} - E_J \cos\left(\frac{\phi_i}{\Phi_0}\right), \quad (4.26)$$

$$H_{\text{int}} = \sum_i \frac{\tilde{q}_i q_r}{\tilde{C}_g}, \quad (4.27)$$

$$H_{qq} = \sum_{i,j \neq i} \frac{\tilde{q}_i \tilde{q}_j}{2C_{qq}}, \quad (4.28)$$

with $\tilde{q} = q + C_q V_G$ and the variables are now operators obeying $[\phi_r, q_r] = [\phi_i, \tilde{q}_i] = i\hbar$. The coupling results in renormalized capacitances $\tilde{C}_r = \tilde{C}^2 / (C_q + C_g)$, $\tilde{C}_q = \tilde{C}^2 / [C_r + C_g + (N-1)C_g C_q / (C_q + C_g)]$ and $\tilde{C}_g = \tilde{C}^2 / C_g$, with $\tilde{C}^2 = C_g C_r + C_q(C_r + N C_g)$, as in the single qubit case, now scaling with the number of qubits N . Especially the effective resonator capacitance $\tilde{C}_r \geq C_r$ which in turn leads to a *smaller* resonator frequency. This goes completely against the result for the

Dicke model including the A^2 -term where an increase of the mode frequency in the presence of the coupling is obtained. Lowering of the oscillator frequency would advance the possibility for a SRPT.

In addition, rather surprisingly, there appears coupling terms between the qubits in the Hamiltonian, with $C_{qq} = (C_g + C_q)\tilde{C}^2/C_g^2$. To add to the unusuality of this term it seems to be an all-to-all interaction with a constant strength. This should not be, however, interpreted as a direct static coupling. Writing down the equations of motion for ϕ_r and ϕ_i 's resulting from the Hamiltonian Eq. (4.24) gives

$$\dot{\phi}_r = \frac{q_r}{\tilde{C}_r} + \sum_i \frac{\tilde{q}_i}{\tilde{C}_g}, \quad (4.29)$$

$$\dot{\phi}_i = \frac{q_i}{\tilde{C}_q} + \frac{q_r}{\tilde{C}_g} + \sum_{j \neq i} \frac{\tilde{q}_j}{C_{qq}}. \quad (4.30)$$

Assuming a stationary oscillator $\dot{\phi}_r = 0$ gives

$$q_r = - \sum_i \frac{\tilde{C}_r}{\tilde{C}_g} \tilde{q}_i. \quad (4.31)$$

Plugging this into the equation for the qubit variable yields

$$\dot{\phi}_i = \left(\frac{1}{\tilde{C}_q} - \frac{\tilde{C}_r}{\tilde{C}_g^2} \right) \tilde{q}_i + \sum_{j \neq i} \left(\frac{1}{C_{qq}} - \frac{\tilde{C}_r}{\tilde{C}_g^2} \right) \tilde{q}_j = \frac{\tilde{q}_i}{C_q + C_g}, \quad (4.32)$$

and the coupling to other qubits has vanished. To obtain the above result we have used $C_{qq} = \tilde{C}_g^2/\tilde{C}_r$ and $\tilde{C}_q^{-1} - C_{qq}^{-1} = (C_q + C_g)^{-1}$. Thus, there are couplings between the qubits mediated by the dynamical resonator, and they do not exist if the resonator does not have dynamics of its own. Note that to arrive at this conclusion the qubit-qubit ‘‘interactions’’ have to be included in the Hamiltonian, since without them there would appear a static interaction due to relation Eq. (4.31). Another argument against interpreting the S_x^2 -term as direct qubit-qubit interactions is the fact that it could be removed by a gauge transformation [51, 70], as we discuss in Chap. 4. Thus, the appearance of the term is related to our choice of canonical variables, $\phi_{r/i}$ and $q_{r/i}$, rather than any physical interaction between the qubits.

Hamiltonian of Eq. (4.24) is defined in the full Hilbert space of the system. To proceed we apply the two-level-approximation to the charge qubits. In the TLA we can write for Cooper-pair-box qubits $H_{q_i} \approx \hbar\tilde{\omega}_q\sigma_i^z/2$, with $\hbar\tilde{\omega}_q \approx E_J$, and $\tilde{q}_i \approx e\sigma_i^x$ [25]. We also introduce the annihilation and creation operators of the

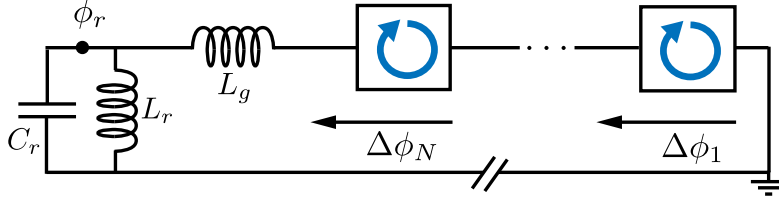


Figure 4.3: Flux qubits coupled to an LC -circuit. The flux quantization condition for the loop formed by the resonator inductor L_r , coupling inductor L_g and the qubits constrain the currents flowing through this loop. The constraint induces dipole-dipole interactions between the qubits, see text. Removing the resonator inductor removes the loop in which case the qubits would be non-interacting.

mode, defined through $\phi_r = i\sqrt{\hbar\tilde{Z}_r/2}(a^\dagger - a)$ and $q_r = \sqrt{\hbar/(2\tilde{Z}_r)}(a^\dagger + a)$. The Hamiltonian in the TLA then reads

$$H_{\text{EDM}} = \hbar\tilde{\omega}_r a^\dagger a + \hbar\tilde{\omega}_q S_z + \hbar g(a^\dagger + a)S_x + \frac{\hbar g^2}{\tilde{\omega}_r} S_x^2, \quad (4.33)$$

where $\tilde{\omega}_r = 1/\sqrt{L_r\tilde{C}_r}$ and $g = \sqrt{\pi\tilde{Z}_r/R_Q\tilde{C}_r/\tilde{C}_g}\tilde{\omega}_r$ which can be obtained easily from the result derived in [sub-Sec. 3.5.1](#). The $S_\alpha = \sum_m \sigma_m^\alpha/2$, $\alpha \in \{x, y, z\}$, are collective spin operators. The factor of the S_x^2 -term, coming from the H_{qq} term in the full Hamiltonian, follows due to the relation $C_{qq} = \tilde{C}_g^2/\tilde{C}_r$. The Hamiltonian we have derived is the Extended Dicke model Hamiltonian [50, 51]. In the following chapters we mostly drop the tilde-notation from the resonator and qubit frequencies for convenience.

4.3.2 Repulsive dipole-dipole interactions

We consider a system described by the circuit of [Fig. 4.3](#). Flux qubits are inductively coupled to an LC -oscillator through a dedicated coupling inductance L_g . We assume them to be 4-junction flux qubits as before for definiteness, but any flux qubit will do. The difference to the inductively coupled circuits we have looked at before is the inclusion of a dedicated resonator inductance L_r in the circuit, rather than letting the resonator inductor be also the coupling inductance.

Let us label the branch flux of the resonator inductor ϕ_r , for the branch flux through the coupling inductor we use ϕ_g , and $\Delta\phi_k$ is the flux jump over the qubit $k = 1, 2, \dots, N$ (for the 4-junction qubit it corresponds to $\tilde{\phi}_4$ of [Eq. \(3.48\)](#)). Without the dedicated resonator inductor the only closed loops in the circuit are the ones of the qubits'. However, with L_r included there is also a big loop formed

by L_r, L_g and the qubits. Thus, we need to apply the flux quantization condition to this loop

$$\phi_r + \phi_g + \sum_k \Delta\phi_k = 0, \quad (4.34)$$

where we have assumed the external flux threading the loop vanishes. This equation can be used to eliminate e.g. the flux through L_g : $\phi_g = -(\sum_k \Delta\phi_k + \phi_r)$. Up to the appearance of a qubit-qubit coupling term, the derivation of the Hamiltonian is identical to the single qubit circuit in [sub-Sec. 3.5.2](#). The resulting Hamiltonian is given by

$$H = H_r + \sum_k \tilde{H}_k + H_{\text{int}} + H_{qq}, \quad (4.35)$$

where

$$H_r = \frac{q_r^2}{2C_r} + \frac{\phi_r^2}{2\tilde{L}_r}, \quad (4.36)$$

$$\tilde{H}_k = H_{4jfq} + \frac{\Delta\phi_k^2}{2L_g}, \quad (4.37)$$

$$H_{\text{int}} = \frac{\phi_r}{L_g} \sum_k \Delta\phi_k, \quad (4.38)$$

$$H_{qq} = \sum_{k,l \neq k} \frac{\Delta\phi_k \Delta\phi_l}{2L_g}, \quad (4.39)$$

and H_{4jfq} is the bare Hamiltonian of a 4-junction flux qubit, [Eq. \(3.48\)](#). Due to the renormalization of the resonator inductance to $\tilde{L}_r = L_r L_g / (L_r + L_g)$ there will be a renormalization of its frequency, which, however, does not scale with the number of coupled qubits. The renormalized qubit and interaction Hamiltonians are the same as obtained in [sub-Sec. 3.5.2](#), with the replacement of $L_r \rightarrow L_g$. The qubit-qubit Hamiltonian is of the same form as we derived for the capacitive circuit in [Sec. 4.3](#), however now it also contains real DD interactions as opposed to [Sec. 4.3](#).

Quantizing this Hamiltonian, using the two-level-approximation for the flux qubits and introducing the annihilation and creation operators for the resonator, we obtain

$$H = \hbar\tilde{\omega}_r a^\dagger a + \tilde{\omega}_q S_z + \hbar g (a^\dagger + a) S_x + (1 + \varepsilon) \frac{\hbar g^2}{\tilde{\omega}_r} S_x^2. \quad (4.40)$$

The coupling $g = L_r / (L_r + L_g) \sqrt{R_Q / (\pi \tilde{Z}_r)} \tilde{\omega}_r \varphi_{01}$ is the same as in [sub-Sec. 3.5.2](#), replacing L_r with \tilde{L}_r , and also including a geometric factor $L_r / (L_r + L_g) \leq 1$. The

factor in front of the S_x^2 is however *not* equal to $g^2/\tilde{\omega}_r$ as before. Rather there is an additional $\varepsilon g^2/\tilde{\omega}_r$ term with $\varepsilon = L_g/L_r \geq 0$. This can be interpreted as a collective dipole-dipole interaction among the qubits, as we will demonstrate. The additional factor vanishes for $L_g/L_r \rightarrow 0$, i.e. if we remove the inductance L_r (in that case “ $L_r = \infty$ ”).

The interpretation of the $\varepsilon g^2/\omega_r S_x^2$ as a direct dipole-dipole interaction is corroborated by considering the e.o.m. for the system. Let us go back to the variables $q_{r(k)}, (\Delta)\phi_{r(k)}$. Writing down the equations for q_r and q_k and assuming a stationary oscillator, $\dot{q}_r = 0$, as in [sub-Sec. 4.3.1](#) we obtain the following equation for q_k

$$\dot{q}_k = -\frac{\partial H_{4jfq}}{\partial \Delta\phi_k} - \sum_l \frac{\Delta\phi_l}{L_r + L_g}. \quad (4.41)$$

The appearance of other qubits $l \neq k$ in the e.o.m. for qubit k indicates a static interaction between them not mediated by a dynamic field ϕ_r . The interaction term vanishes in the limit $L_r \rightarrow \infty$ as it should.

The direct dipole-dipole coupling originates from the flux quantization condition [Eq. \(4.34\)](#), which relates the currents flowing in the resonator and coupling inductors, and through the qubits. It constrains the current through the coupling inductor, which is a free variable if the dedicated resonator inductor, and thus also the loop, is missing. This constraint then leads to the observed direct interaction, which also explains the collective nature of the interaction: all of the qubits are equally represented in [Eq. \(4.34\)](#), necessitating a collective interaction.

4.3.3 Attractive dipole-dipole interactions

Using flux qubits it is also possible to create systems with attractive direct DD interactions between the qubits. We analyze here a setup from Ref. [\[104\]](#). Rather than coupling the qubits to the resonator through a single coupling inductor as previously, we couple them to the resonator in parallel through dedicated coupling inductors L_g for every qubit, see [Fig. 4.4](#). We have taken the qubits to be single Josephson junctions as in Ref. [\[104\]](#).

Every loop formed by the resonator inductor L , coupling inductor L_g and the junction are threaded by an external flux ϕ_e . For N qubits this gives rise to N flux quantization conditions

$$\phi_r + \phi_{g_i} + \psi_i = \phi_e, \quad \forall i = 1, 2, \dots, N, \quad (4.42)$$

where $\phi_{r(g_i)}$ is the flux jump across the resonator (coupling) inductor and ψ_i the flux jump across the junction. These equations are used to eliminate the N extra variables. In [\[104\]](#) the node fluxes ϕ_r, ϕ_i are chosen as the independent variables,

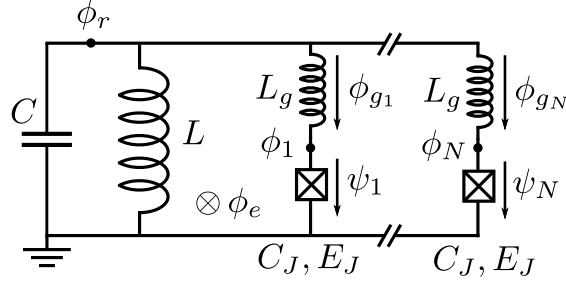


Figure 4.4: Flux qubit circuit implementing attractive dipole-dipole interactions. The N loops formed by the resonator inductor L_r , every coupling inductor L_g and the junction of the qubit give flux quantization conditions that couple the qubit variables together. The external flux ϕ_e is used to invert the cosine potential of the Josephson junctions.

where ϕ_i is the node flux in the node between the i th junction and coupling inductor, leading to

$$\phi_g = \phi_i - \phi_r, \quad (4.43)$$

$$\psi_i = \phi_e - \phi_i. \quad (4.44)$$

There are no capacitive couplings in the circuit such that the conjugate charges to ϕ_r and ϕ_i 's are just $q_r = C_r \dot{\phi}_r$ and $q_i = C_J \dot{\phi}_i$, respectively. The Hamiltonian then becomes [104]

$$H = \frac{q_r^2}{2C_r} + \frac{\phi_r^2}{2L_r} + \sum_i \left[\frac{q_i^2}{2C_J} + \frac{(\phi_i - \phi_r)^2}{2L_g} - E_J \cos \left(\frac{\phi_i + \phi_e}{\Phi_0} \right) \right]. \quad (4.45)$$

The external flux is chosen to have a value of $\phi_e/\Phi_0 = \pi$, such that the sign of the cosine potential is flipped for every qubit. Going to the annihilation and creation operators for the resonator and performing a two-level-approximation on the qubits¹ we obtain the Hamiltonian

$$H = \omega_r a^\dagger a + \omega_q S_z + g(a^\dagger + a)S_x. \quad (4.46)$$

The resulting Hamiltonian looks identical to that of the Dicke model. However, the interpretation of the Hamiltonian is not that simple due to Eq. (4.42) which couples the branch fluxes related to the coupling inductors and the Josephson junctions to that of the resonator. We can again gain intuition by looking at the

¹The TLA is not justified [104], but since we are only interested in the form of the Hamiltonian it is fine for the current analysis.

equations of motion for the circuit in the case of a static resonator, $\dot{q}_r = 0$. This gives the equations of motion for the qubit variables

$$\dot{q}_i = I_c \sin\left(\frac{\phi_i}{\Phi_0}\right) - \frac{\phi_i}{L_g} + \sum_{j \neq i} \frac{\tilde{L}_r}{L_g^2} \phi_j, \quad (4.47)$$

where $\tilde{L}_r = L_r L_g / (L_g + N L_r)$. In the e.o.m. there appear variables of the other qubits $\phi_{j \neq i}$ such that there are static dipole-dipole interactions between them, not dynamic ones mediated by a dynamic oscillator mode.

Based on the above considerations it is instructive to write the Hamiltonian Eq. (4.46) in the same form as Eq. (4.40)

$$H = \omega_r a^\dagger a + \omega_q S_z + g(a^\dagger + a)S_x + (1 + \varepsilon) \frac{g^2}{\omega_r} S_x^2, \quad (4.48)$$

where $\varepsilon \equiv -1$ is now fixed rather than tunable as in the case of the repulsive interactions. Thus, we can interpret the system as a collection of qubits coupled to a common resonator with attractive collective DD interactions. It is an interesting coincidence that the strength of the interactions is exactly such that the gauge dependent S_x^2 -term is cancelled, resulting in the Dicke model.

4.3.4 General description of qubits coupled to a single mode resonator

The treatment above can be generalized to describe a generic system of dipoles interacting with a single mode resonator through a dipole transition and with each other through dipole-dipole interactions [51]. The generic cavity/circuit QED Hamiltonian is then given by

$$H_{\text{cQED}} = \omega_r a^\dagger a + \sum_i \left[\frac{\omega_i}{2} \sigma_i^z + \frac{g_i}{2} (a^\dagger + a) \sigma_i^x + \frac{g_i g_j}{4\omega_r} \sum_j (1 + D_{ij}) \sigma_i^x \sigma_j^x \right]. \quad (4.49)$$

In the above equation we have allowed the two-level-systems to have different frequencies and interaction strengths with the field mode. The D_{ij} is the dipole-dipole interaction strength between qubits i and j . Note, the DD coupling strength is given in units of $g_i g_j / \omega_r$ and the D_{ij} are dimensionless. The dipole-dipole interactions D_{ij} do not have to have a r^{-3} dipole character, rather they depend on the boundary conditions for the field modes that mediate the interactions. In case of free-space the typical DD couplings would be recovered [51].

The above Hamiltonian also shows that the single mode approximation cannot be done in a simple minded way of just cutting the full radiative field to a single

mode. Rather, the other modes have to be carefully adiabatically eliminated, and they result in relevant interactions between the qubits [51].

The general Hamiltonian Eq. (4.49) is very complex. In order to simplify the discussion we need to make some simplifications. As before we assume that the qubits are identical, i.e. their transition frequencies are equal $\omega_i = \omega_q$ and the qubits couple to the resonator with the same coupling strength $g_i = g$. In the simplest approximation we take the dipole-dipole interactions into account only in an average way. This is achieved by introducing the averaged DD coupling strength

$$\varepsilon = \frac{1}{N} \sum_{i,j \neq i} D_{ij}, \quad (4.50)$$

which is equal for all of the qubits. Then we replace the DD interaction with a collective coupling

$$\sum_{i,j} D_{ij} \sigma_i^x \sigma_j^x / 4 \rightarrow \varepsilon S_x^2. \quad (4.51)$$

The general cQED Hamiltonian of Eq. (4.49) then reduces to that of the Extended Dicke model

$$H_{\text{EDM}} = \omega_r a^\dagger a + \omega_q S_z + g(a^\dagger + a)S_x + (1 + \varepsilon) \frac{g^2}{\omega_r} S_x^2. \quad (4.52)$$

This approximation captures the qualitative behaviour of the dipole-dipole interactions: with on average ferromagnetic interactions $\varepsilon < 0$ the qubits want to align themselves parallel in the x-direction, and for $\varepsilon > 0$, i.e. anti-ferromagnetic (averaged) interactions they prefer to be anti-aligned along x. Of course in this approximation the total angular momentum \mathbf{S} is conserved which is not true in the general case. Especially for larger DD coupling strengths this can cause inaccuracies. The value of ε is sensitive to the geometry of the qubit ensemble [51]. For example, if we have dipoles arranged in a lattice and the ensemble has a spherical shape the averaged dipole-dipole interaction strength vanishes $\varepsilon = 0$ [51].

This approximation can be made more rigorous. Let us take the dipole-dipole interaction matrix D_{ij} and diagonalize it. This gives us the N eigenmodes of the DD coupling matrix. The averaged interaction strength ε then corresponds to the totally symmetric mode of D_{ij} in which all of the qubits participate equally. The above approximation then consists of neglecting all other modes of the interaction matrix.

Clearly the Hamiltonians for the two circuits we have analysed above fall under this description. In the cases we have treated $g_i = g$ for all the qubits and also $D_{ij} = D$ for all different pairs of qubits. The DD interactions are given by $D =$

$L_g/((N-1)L_r)$ for repulsive DD interactions, and for the attractive couplings $D = -1/(N-1)$. Note that for the circuits we analysed the EDM Hamiltonian is not an approximation of the general Hamiltonian. In these setups the dipole-dipole interactions, if present, are naturally of collective type.

4.4 Justification of the EDM: Gauge non-invariance in the USC regime

The Hamiltonians we have derived in the previous section all are written in the *electric dipole gauge* (introduced below). In principle a gauge transformation could be performed on the Hamiltonian and a different looking, but equivalent Hamiltonian will be obtained. In the literature another widely used gauge is the *Coulomb gauge*. The equivalence of Hamiltonians in different gauges is, however, guaranteed only in the full Hilbert space of the system. We demonstrate that the electric dipole gauge, which leads to the Extended Dicke model after the two-level-approximation, is the gauge to use in the USC regime rather than Coulomb gauge.

4.4.1 Gauge freedom in cavity QED

Maxwell's equations of classical electrodynamics are invariant under the transformation of the scalar potential Φ_{el} and vector potential \mathbf{A} by [105]

$$\Phi_{el} \rightarrow \Phi_{el} + \frac{\partial f}{\partial t} \quad (4.53)$$

$$\mathbf{A} \rightarrow \mathbf{A} + \nabla f, \quad (4.54)$$

where f is a twice differentiable function of position and time. In the language of Lagrangians this freedom appears as a two Lagrangians differing by a total derivative giving the same equations of motions. For Hamiltonians gauge transformations can be performed with canonical transformations in the classical case and in the quantum realm by unitary transformations. In cavity QED mostly two gauges are used when performing calculations, the Coulomb gauge and the electric dipole gauge. Next we shortly review how they are defined.

Note, we are only treating systems in the dipole approximation and consider systems of non-interacting TLS's. Dipole-dipole interactions are gauge invariant and will not change the conclusions made in this section.

Coulomb gauge

The Coulomb gauge is defined by the condition [106]

$$\nabla \cdot \mathbf{A} = 0. \quad (4.55)$$

In this case we can use the well know minimal coupling replacement for a charged particle moving in an electromagnetic field

$$\mathbf{p} \rightarrow \mathbf{p} + q\mathbf{A}, \quad (4.56)$$

where q is the charge of the particle and p its momentum. Thus, the Hamiltonian for a single particle of mass m , moving in one dimension, coupled to a single mode of the electromagnetic field will have the form

$$H_C = \frac{(p - qA)^2}{2m} + V(x) + \hbar\omega_r a^\dagger a, \quad (4.57)$$

where $V(x)$ is the confining potential of the particle, ω_r the frequency of the field mode and $A = \mathcal{A}_0(a^\dagger + a)$, with \mathcal{A}_0 a zero-point amplitude. The interaction between the particle and the mode is of the form

$$H_{\text{int}}^C \propto p \times A. \quad (4.58)$$

Expanding the square gives also the infamous A^2 -term, $q^2/(2m)A^2$, which renormalizes the mode frequency to $\tilde{\omega}_r = \sqrt{\omega_r^2 + D^2}$ [59], with $D = 2q^2\mathcal{A}_0^2\omega_r/(\hbar m)$.

Electric dipole gauge

We can change from the Coulomb gauge to the electric dipole gauge by performing the unitary transformation [70]

$$\mathcal{U} = e^{-iqxA/\hbar}. \quad (4.59)$$

The Hamiltonian in the electric dipole gauge reads [70]

$$H = \frac{p^2}{2m} + \tilde{V}(x) + \hbar\omega_r a^\dagger a + i\omega_r q\mathcal{A}_0(a^\dagger - a)x, \quad (4.60)$$

where the potential of the particle has been renormalized to $\tilde{V}(x) = V(x) + mD^2x^2/2$ due to the coupling to the mode. The coupling is now of the form

$$H_{\text{int}}^D \propto x \times E, \quad (4.61)$$

where $E = i\omega_r\mathcal{A}(a^\dagger - a)$ is the electric field. Since H_D and H_C are connected by a unitary (i.e. gauge) transformation they share the same spectrum and are, thus, equivalent.

The equivalence of the Coulomb and dipole gauge Hamiltonians is no longer true when using a two-level-approximation for the matter system as discussed in detail in Ref. [70]. Here we present the analysis as it concerns superconducting quantum circuits, where different circuit variables can be connected by gauge transformations.

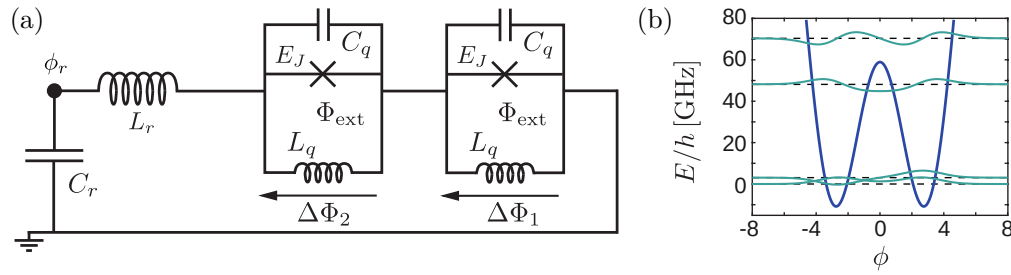


Figure 4.5: (a) Fluxonium qubits coupled to an LC -circuit. (b) The bare potential $V(\phi)$ of the fluxonium qubit. We choose the parameters $E_{L_q}/h = 7$ GHz, $E_{C_q}/h = 12$ GHz and $E_J/h = 50$ GHz for the qubit. These give $\omega_q/(2\pi) \approx 3$ GHz and anharmonicity $\omega_{12}/\omega_{01} \approx 15$, consistent with experimentally realized values [107].

4.4.2 Case study: flux qubits coupled to an LC-resonator

As an example we consider flux qubits coupled to an LC -resonator. We present the Hamiltonian in the Coulomb and electric dipole gauges.

Electric dipole gauge Hamiltonian

We consider the circuit of Fig. 4.5(a). The Hamiltonian for this system is given by [70]

$$H_\Phi = 4E_{C_r} n_r^2 + \frac{E_{L_r}}{2} \left(\varphi_r - \sum_i \varphi_i \right)^2 + \sum_i \left[4E_{C_q} n_i^2 + E_J \cos(\varphi_i) + \frac{E_{L_q}}{2} \varphi_i^2 \right], \quad (4.62)$$

where $E_{C_{r/q}} = e^2/(2C_{r/q})$ and $E_{L_{r/q}} = \Phi_0^2/L_{r/q}$ are the charging and inductive energies, and $\varphi_i = \Delta\phi_i/\Phi_0$, $\varphi_r = \phi_r/\Phi_0$ and $n_{i,r} = q_{i,r}/(2e)$ are the dimensionless flux and charge variables, respectively. This Hamiltonian is identical to the electric dipole gauge Hamiltonian Eq. (4.60): an effective particle moving in a potential $V(\varphi) = E_J \cos(\varphi_i) + E_{L_q} \varphi_i^2/2$, shown in Fig. 4.5(b), is coupled to a mode through its position variable φ_i .

Coulomb gauge Hamiltonian

From the electric dipole gauge Hamiltonian we can obtain the Coulomb gauge Hamiltonian by the inverse of the unitary transformation we introduced above, Eq. (4.59), with $A \rightarrow q_r$ and $x \rightarrow \phi_i$, plus a sum over the qubit variables i . The

Hamiltonian in the Coulomb gauge is given by [70]

$$H_Q = 4E_{C_r}n_r^2 + \frac{E_{L_r}}{2}\varphi_r^2 + \sum_i [4E_{C_q}(n_i - n_r)^2 + V(\varphi_i)]. \quad (4.63)$$

It can be readily seen that the Hamiltonian is equivalent to the Coulomb gauge Hamiltonian Eq. (4.57): an effective particle moving in a potential coupled to the field through its conjugate momentum.

4.4.3 Gauge non-invariance of the two level approximation

Now that we have obtained the full Hamiltonians in the electric dipole and Coulomb gauges we consider both of them in the two-level-approximation for the flux qubits.

4.4.4 TLA in Coulomb gauge

Let us start with the derivation of the two-level Hamiltonian in the Coulomb gauge. To start with expand the square $(n_i - n_r)^2$ and obtain an “ A^2 -term” for the oscillator mode which can be absorbed into the kinetic energy term to obtain a renormalized charging energy

$$E_{\tilde{C}_r} = E_{C_r} + NE_{C_q}. \quad (4.64)$$

Then we can introduce the creation and annihilation operators through $n_r = i\sqrt{E_{L_r}/(32E_{\tilde{C}_r})}(a^\dagger - a)$ and $\varphi_r = \sqrt{2E_{C_r}/E_{L_r}}(a^\dagger + a)$. The individual qubit Hamiltonian can be diagonalized to obtain the two lowest energy levels $|\psi_0\rangle$ and $|\psi_1\rangle$ and their splitting ω_q . Then the charge operator can be expressed using the eigenstates as $n = |\langle\psi_0|n|\psi_1\rangle|\sigma_x = n_{01}\sigma_x$. The two-level Hamiltonian then becomes

$$H_Q^{\text{TLA}} = \hbar\tilde{\omega}_r a^\dagger a + \hbar\omega_q S_z + i\hbar g_Q (a^\dagger - a)S_x, \quad (4.65)$$

with $\tilde{\omega}_r = \sqrt{8E_{\tilde{C}_r}E_{L_r}}/\hbar$ the renormalized cavity frequency and

$$g_Q = \frac{8E_{C_q}}{\hbar} \sqrt{\frac{\omega_r}{\tilde{\omega}_r}} \sqrt{\frac{E_{L_r}}{2E_{C_r}}} n_{01}, \quad (4.66)$$

the coupling. Above $\omega_r = \sqrt{8E_{C_r}E_{L_r}}/\hbar$ is the bare oscillator frequency. The obtained Hamiltonian is given by that of the Dicke model.

Consider now a situation with only a single flux qubit coupled to the LC -oscillator. The matrix element of the charge operator appearing in the definition

of the coupling constant can be turned into a flux matrix element by using the general relation

$$p_{nk} = im(\omega_n - \omega_k)x_{nk}, \quad (4.67)$$

between position and momentum matrix elements. Using this result we get [70]

$$\frac{g_Q^2}{\omega_q \tilde{\omega}_c} = \frac{E_{C_q}}{E_{C_r} + E_{C_q}} f, \quad (4.68)$$

where $f = 2C_q \Phi_0^2 \omega_q \varphi_{01}^2 / \hbar$ is the oscillator strength. Using the Thomas-Reiche-Kuhn (TRK) sum rule we can constraint $f \leq 1$, so that

$$\frac{g_Q^2}{\omega_q \tilde{\omega}_r} \leq 1. \quad (4.69)$$

This is the no-go result of the SRPT when including the A^2 -term, the critical coupling of the Dicke model cannot be reached.

4.4.5 TLA in electric dipole gauge

Now we repeat our derivation of the two-level Hamiltonian from the electric dipole gauge Hamiltonian Eq. (4.60). For the oscillator the annihilation and creation operators are as before with the replacement of the renormalized charging energy $E_{\tilde{C}_r}$ with the bare one E_{C_r} . The qubit eigenstates and energies are obtained using the renormalized potential $\tilde{V}(\varphi) = V(\varphi) + E_{L_r}/2\varphi^2$ resulting in a qubit frequency $\tilde{\omega}_q$ and we expand the flux operator using the two lowest energy states to $\varphi = |\langle \tilde{\psi}_0 | \varphi | \tilde{\psi}_1 \rangle| \sigma_x = \tilde{\varphi}_{01} \sigma_x$. The Hamiltonian becomes

$$H_{\Phi}^{\text{TLA}} = \hbar \omega_r a^\dagger a + \hbar \tilde{\omega}_q S_z + \hbar g_{\Phi} (a^\dagger + a) S_x + \frac{\hbar g_{\Phi}^2}{\omega_r} S_x^2, \quad (4.70)$$

with the coupling constant

$$g_{\Phi} = \omega_r \sqrt{\frac{E_{L_r}}{2E_{C_r}}} \tilde{\varphi}_{01}. \quad (4.71)$$

The obtained approximate Hamiltonian is that of the Extended Dicke model as expected based on Sec. 4.3.

Let us again consider a situation with a single qubit coupled with the resonator and evaluate the dimensionless coupling constant. We obtain

$$\frac{g_{\Phi}^2}{\omega_r \tilde{\omega}_q} = \frac{E_{C_q} E_{L_r}}{\hbar^2 \tilde{\omega}_q^2} \tilde{f}, \quad (4.72)$$

with the modified oscillator strength $\tilde{f} = 2C_q\tilde{\omega}_q|\tilde{\varphi}_{01}^2|/\hbar$. Again the oscillator strength is bounded from above using the TRK sum rule and we obtain

$$\frac{g_{\Phi}^2}{\omega_r\tilde{\omega}_q} \leq \frac{E_{C_q}E_{L_r}}{\hbar^2\tilde{\omega}_q^2}. \quad (4.73)$$

For an arbitrary potential, thus, the dimensionless coupling constant is not bound by unity, rather it can have *a priori* any value. It can be show [70], however, that in order for to obtain $g_{\Phi}^2/(\tilde{\omega}_q\omega_r) > 1$ the bare potential of the qubit $V(\varphi)$ must be non-convex at $\varphi = 0$. Thus, e.g. with a transmon qubit the critical Dicke coupling cannot be reached.

We have derived a two-level Hamiltonian in two gauges and shown that they result in different conditions on the dimensionless coupling constant $g^2/(\omega_q\omega_r)$. This implies differences in the physics predicted by the two Hamiltonians. This shows clearly that the two approximate Hamiltonians are not anymore equivalent in their spectra or other gauge invariant quantities.

For a multi-qubit system it can be shown [70] that the Coulomb and electric dipole gauge Hamiltonians both predict absence of superradiance. However, the mechanism is different. In the Coulomb gauge the absence of superradiance traces back to the limitation on the dimensionless single qubit-photon coupling strength, Eq. (4.69). In the electric dipole gauge it is rather the S_x^2 -term present in the Hamiltonian that prevents superradiance as we will shown in Chap. 5, while the dimensionless interaction strength is not constrained. These no-go theorems apply in systems of non-interacting qubits coupled to a field mode. As we will show in Chap. 5 attractive dipole-dipole interactions can cause an instability, in both gauges, and a transition into a superradiant phase. This is possible, however, only in specific situations and has nothing to do with the cavity [51].

4.4.6 Validity of the TLA

Now that we have established that the TLA Hamiltonians derived in different gauges predict different physics when the coupling is large, we need to ask which one gives accurate predictions, or if possibly both are inaccurate. To answer this question we compare the two approximate Hamiltonians Eq. (4.65) and Eq. (4.70) to the full Hamiltonian H_{Φ} of Eq. (4.62).

In Fig. 4.6(a) we compare the spectra from the approximate TLA Hamiltonians to the numerically exact spectrum of the full Hamiltonian. The eigenenergies are plotted against

$$g_0 = \omega_r \sqrt[4]{\frac{E_{L_r}}{2E_{C_r}}} |\langle \psi_0 | \varphi | \psi_1 \rangle|, \quad (4.74)$$

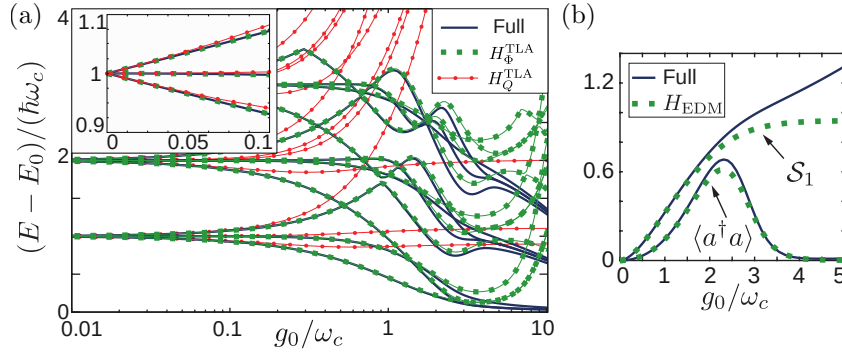


Figure 4.6: (a) Comparison between the spectra from the full Hamiltonian of Eq. (4.62), blue line, and the two-level truncated Hamiltonians Eq. (4.70), green square markers, and Eq. (4.65), red round markers. (b) The ground state photon number, $\langle \text{GS} | a^\dagger a | \text{GS} \rangle$, and entanglement entropy of a single qubit $\mathcal{S}_1 = -\text{Tr}[\rho_1 \log_2(\rho_1)]$, with $\rho_1 = \text{Tr}_{r,N-1}[\rho]$ the single qubit reduced density matrix, from the full Hamiltonian, solid blue line, and the electric dipole gauge TLA Hamiltonian, green square markers.

which is the coupling strength in the electric dipole gauge without including a modification of the flux matrix element coming from the harmonic renormalization term. We see that all of the spectra agree for small interaction strengths as one would expect. As the coupling increases, however, the spectrum calculated using the Coulomb gauge two-level Hamiltonian starts to deviate strongly from the exact spectrum, while the approximate electric dipole gauge Hamiltonian still agrees with it. For even stronger couplings, $g_0/\omega_r \sim 4$, also the TLA Hamiltonian in the electric dipole gauge breaks down and deviates strongly from the exact result.

This observation is not just specific to the chosen system of flux qubits and an LC -oscillator. Using the two-level-approximated versions of the generic Hamiltonians Eq. (4.57) and Eq. (4.60) with a double-well or box potential for the qubit gives the same result: for ultrastrong couplings the electric dipole gauge Hamiltonian in the two-level-approximation gives more accurate results than the corresponding Coulomb gauge Hamiltonian [70]. Intuition for why this is the case can be obtained from the relation Eq. (4.67). It shows that the matrix elements of the momentum operator, in circuit QED language the charge operator, are enhanced by the transition frequency of the transition. We plot the matrix elements of the flux and the charge operator for the flux qubit that we have used in Fig. 4.7(a) and (b), respectively. We see clearly that the matrix elements of the flux operator only weakly couples the two lowest states $|\psi_{0/1}\rangle$ to the rest of the spectrum. For the charge operator this is not true, the matrix elements of the qubit states to the other states tend to be larger than the coupling between the qubit states. Thus,

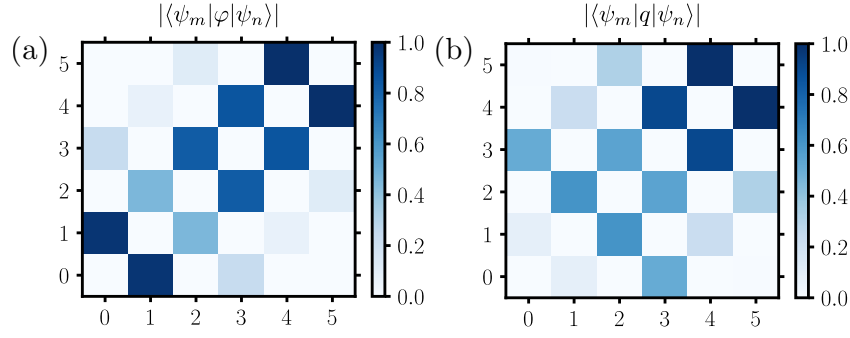


Figure 4.7: (a) Matrix elements of the flux φ between eigenstates $|\psi_n\rangle$ and $|\psi_m\rangle$ of the qubit. (b) Matrix elements of the charge operator q between eigenstates $|\psi_n\rangle$ and $|\psi_m\rangle$ of the qubit. In both plots we have normalized the magnitude of the matrix elements to one.

even though the anharmonicity of the flux qubit is large, $\omega_{12}/\omega_{01} \sim 15$ for the parameters we have chosen, the simple two-level-approximation is not valid in the Coulomb gauge due to large matrix elements of the charge operator coupling the two-level-subspace to the rest of the spectrum. In the electric dipole gauge the coupling of the qubit to the resonator happens through the flux operator which is well contained in the two-level-subspace. For a harmonic “qubit” the charge and flux, or more generally the momentum and position, variables are equivalent and there is no distinction between the Coulomb and electric dipole gauge, or any other gauge either, but of course the TLA is in this case not relevant since there is no separated transition to begin with.

In Fig. 4.6(b) we demonstrate that not only the spectrum is correctly reproduced by the electric dipole gauge TLA Hamiltonian. We plot the ground state photon number and the entanglement between the spins as a function of g_0 for the approximate and full Hamiltonians and observe good quantitative agreement for the photon number and qualitative agreement for the entanglement. The entanglement from the full Hamiltonian does not saturate since the two-level-subspace is not perfectly decoupled from the rest of the spectrum, a result which cannot be captured with the TLA Hamiltonian due to the maximal entanglement entropy of $\log_2(2) = 1$. However, qualitatively they both predict highly entangled qubit states. See Chap. 5 to how this behaviour comes about.

4.4.7 Remarks

We have demonstrated that the *simple* two-level-approximation cannot be performed equally accurately in the Coulomb gauge and the electric dipole gauge.

It is possible, however, to perform the TLA in a different way in the Coulomb gauge and obtain a two-level Hamiltonian that performs equally well as the electric dipole gauge Hamiltonian [108]. The resulting Hamiltonian, however, is not of the Rabi, Dicke or even extended Dicke model type. This Hamiltonian can also be obtained from the EDM Hamiltonian by a two-level truncated version of the full gauge transformation Eq. (4.59) [51, 108] which is equivalent to the polaron transformation, see App. A. In [108] the authors relate the failure of the simple two-level-approximation in the Coulomb gauge to an incomplete application of the minimal coupling replacement $p \rightarrow p - qA$ when using the simple TLA. In the two-level-approximation the potential of the qubit becomes non-local, which is equivalent to a momentum dependent potential energy [108]. The $p \rightarrow p - qA$ replacement has to be done also in the potential not just in the kinetic energy.

If one is only interested in producing the two lowest energy eigenvalues with the highest fidelity with a TLA Hamiltonian, it is possible that neither the Coulomb gauge nor the electric dipole gauge gives the best result [109]. In this situation a gauge which eliminates the counter rotating terms from the light-matter coupling can be the best choice, in Ref. [109] called the Jaynes-Cummings gauge. The rest of the spectrum naturally cannot be reproduced in this gauge since the spectrum will be that of the Jaynes-Cummings model.

In [110] the authors study a situation where the TLS is coupled strongly to not one but two modes simultaneously. In this case the best Rabi-type two-level Hamiltonian can be found with an intermediate gauge between the Coulomb and electric dipole gauges. For larger number of coupled modes it is still an open question what is the optimal gauge.

Finally, let us touch on a limitation of the discussion presented in this chapter. The analysis we have used, and also discussion in [108–110], assumes the TLSs to have non-compact support. That is, charge qubits capacitively coupled to resonator cannot be treated by the formalism presented. The failure in this situation comes about due to the different canonical commutation relation (CCR) Eq. (3.25). The modified CCR invalidates the relation Eq. (4.67) and also the TRK sum rule used to bound the oscillator strength.

Chapter 5

Physics of the Extended Dicke model

In this chapter we discuss the physics of the Extended Dicke model. We begin by analysing in detail the important case of non-interacting qubits coupled to a resonator mode. Then we expand the discussion to qubits who additionally have dipole-dipole interactions. A phase diagram of cavity QED is presented and the different phases are discussed.

Since the Hamiltonian of the EDM, Eq. (4.33), commutes with the total spin operator $[H_{\text{EDM}}, \mathbf{S}^2] = 0$, with $\mathbf{S}^2 = \sum_{\alpha} S_{\alpha}^2$. Thus, the Hilbert space factorizes into non-interacting blocks between subspaces of different spin quantum number s . This allows us to concentrate on a total spin subspace s which brings the number of qubit states down from 2^N to $2s + 1$, allowing to perform numerics for $N > 10$ qubits coupled to the mode.

5.1 Special case of non-interacting qubits

Let us start by considering the case of non-interacting qubits, $\varepsilon = 0$. In the next section we explore the phase diagram in the g, ε landscape.

5.1.1 Bosonization in the large N limit

To analyse the physics of the EDM we start by considering the limit of a large number of coupled qubits $N \gg 1$. In this situation it is beneficial to transform from the collective spin variables to bosonic operators with the *Holstein-Primakoff*

transformation [111]:

$$S_z = b^\dagger b - \frac{N}{2}, \quad (5.1)$$

$$S_+ = \sqrt{N} b^\dagger \sqrt{1 - \frac{b^\dagger b}{N}}, \quad (5.2)$$

$$S_- = \sqrt{N} \sqrt{1 - \frac{b^\dagger b}{N}} b. \quad (5.3)$$

This transformation is exact, the commutation relations of the spin operators are preserved. We can, however, make a simplification, when the number of qubits is large compared to $\langle b^\dagger b \rangle$, or, equivalently, the qubits are close to their collective ground state, $\langle S_z \rangle \approx -N/2$. This allows us to expand the square roots as a series in $b^\dagger b/N$ and only keep the leading order term. This results in the collective spin becoming a bosonic mode

$$S_z = b^\dagger b - \frac{N}{2}, \quad (5.4)$$

$$S_x \approx \frac{\sqrt{N}}{2} (b^\dagger + b). \quad (5.5)$$

The resulting Hamiltonian is ($\hbar = 1$)

$$H_{\text{HP}} = \omega_r a^\dagger a + \omega_q b^\dagger b + \frac{G}{2} (a^\dagger + a)(b^\dagger + b) + \frac{G^2}{4\omega_r} (b^\dagger + b)^2, \quad (5.6)$$

where we have introduced the collective coupling constant $G = \sqrt{N}g$, already familiar from previous sections. We call this Hamiltonian the Holstein-Primakoff Hamiltonian.

Hamiltonian Eq. (5.6) is quadratic in the bosonic operators $a^{(\dagger)}$ and $b^{(\dagger)}$. This means it can be diagonalized with a Bogoliubov-transformation. We denote by operators c_\pm the resulting upper and lower polariton modes with frequencies

$$\omega_\pm^2 = \frac{1}{2} \left[\omega_r^2 + \Omega_q^2 + \sqrt{(\omega_r^2 - \Omega_q^2)^2 + 4G^2\omega_r\omega_q} \right], \quad (5.7)$$

where $\Omega_q^2 = \omega_q^2(1 + G^2/(\omega_r\omega_q))$. The diagonal Hamiltonian is given by $H =$

$\sum_{\eta} \omega_{\pm} c_{\pm}^{\dagger} c_{\pm}$. The new operators written in terms of the old ones are

$$c_{+}^{\dagger} + c_{+} = \cos(\theta) \sqrt{\frac{\omega_{+}}{\omega_r}} (a^{\dagger} + a) + \sin(\theta) \sqrt{\frac{\omega_{+}}{\omega_q}} (b^{\dagger} + b), \quad (5.8)$$

$$c_{+}^{\dagger} - c_{+} = \cos(\theta) \sqrt{\frac{\omega_r}{\omega_{+}}} (a^{\dagger} - a) + \sin(\theta) \sqrt{\frac{\omega_q}{\omega_{+}}} (b^{\dagger} - b), \quad (5.9)$$

$$c_{-}^{\dagger} + c_{-} = -\sin(\theta) \sqrt{\frac{\omega_{-}}{\omega_r}} (a^{\dagger} + a) + \cos(\theta) \sqrt{\frac{\omega_{-}}{\omega_q}} (b^{\dagger} + b), \quad (5.10)$$

$$c_{-}^{\dagger} - c_{-} = -\sin(\theta) \sqrt{\frac{\omega_r}{\omega_{-}}} (a^{\dagger} - a) + \cos(\theta) \sqrt{\frac{\omega_q}{\omega_{-}}} (b^{\dagger} - b), \quad (5.11)$$

where the mixing angle θ is defined through

$$\tan(2\theta) = \frac{2G\sqrt{\omega_r\omega_q}}{\omega_r^2 - \Omega_q^2}. \quad (5.12)$$

A hall-mark of the SRPT in the Dicke model is the vanishing of the lower polariton mode frequency $\omega_{-}(G_c) = 0$ [65]. From Eq. (5.7) we can evaluate this condition:

$$\begin{aligned} \omega_{-} &= 0 \\ \Leftrightarrow \omega_r^2 + \Omega_q^2 &= \sqrt{(\omega_r^2 - \Omega_q^2)^2 + 4G^2\omega_r\omega_q} \\ \Leftrightarrow \omega_r^2\Omega_q^2 &= G^2\omega_r\omega_q \\ \Leftrightarrow \frac{G^2}{\omega_r} &= \omega_q + ND, \end{aligned} \quad (5.13)$$

where $D = g^2/\omega_r$ is the coefficient of the S_x^2 -term in Eq. (4.33). Thus, this condition can be fulfilled only in the special case of $\omega_q = 0$. For the Dicke model, however, we would have $D = 0$, and the critical coupling derived in Sec. 4.2 is recovered. Thus, we have shown that the SRPT is not present in the Extended Dicke model. It is prevented by the S_x^2 -term which is responsible for the D dependent terms in ω_{\pm} . It, thus, seems to be analogous to the A^2 -term of the Dicke model, since they both prevent the phase transition. However, in contrast to the A^2 -term, the S_x^2 -term is not present for a single qubit coupled to a resonator.

Expectation values of all desired operators can be obtained in the eigenstates of the normal modes $|n_{+}, n_{-}\rangle$ using $c_{\pm}^{(\dagger)} |n_{\pm}\rangle = \sqrt{n_{\pm}(\pm 1)} |n_{\pm} - (\pm 1)\rangle$ and the expressions of the old operators $a^{(\dagger)}$ and $b^{(\dagger)}$ as combinations of the new operators.

Inverting the relations (5.8 - 5.11) we obtain

$$a^\dagger + a = \cos(\theta) \sqrt{\frac{\omega_r}{\omega_+}} (c_+^\dagger + c_+) - \sin(\theta) \sqrt{\frac{\omega_r}{\omega_-}} (c_-^\dagger + c_-), \quad (5.14)$$

$$a^\dagger - a = \cos(\theta) \sqrt{\frac{\omega_+}{\omega_r}} (c_+^\dagger - c_+) - \sin(\theta) \sqrt{\frac{\omega_-}{\omega_r}} (c_-^\dagger - c_-), \quad (5.15)$$

$$b^\dagger + b = \sin(\theta) \sqrt{\frac{\omega_q}{\omega_+}} (c_+^\dagger + c_+) + \cos(\theta) \sqrt{\frac{\omega_q}{\omega_-}} (c_-^\dagger + c_-), \quad (5.16)$$

$$b^\dagger - b = \sin(\theta) \sqrt{\frac{\omega_+}{\omega_q}} (c_+^\dagger - c_+) + \sin(\theta) \sqrt{\frac{\omega_-}{\omega_q}} (c_-^\dagger - c_-). \quad (5.17)$$

For example, the expectation value of the number of photons $n = \langle a^\dagger a \rangle$ in the ground state is found to be [50]

$$\langle a^\dagger a \rangle = \frac{1}{8} (\cos(2\theta)\zeta_- + \zeta_+ - 4), \quad (5.18)$$

where we have defined $\zeta_\pm = (\omega_+\omega_- \pm \omega_r^2)(\omega_+ \pm \omega_-)/(\omega_r\omega_+\omega_-)$. This is a cumbersome expression in general, but for $G \ll \omega_r, \omega_q$ it can be simplified to

$$\langle a^\dagger a \rangle \approx \frac{G^2\omega_r}{4(\omega_r + \omega_q)^2[\omega_q + ND - G^2/\omega_r]}, \quad (5.19)$$

In our case $ND - G^2/\omega_r = 0$ and nothing special happens at the critical coupling G_c as expected. For the Dicke model, however, $D = 0$ and there would be a divergence at the critical coupling $\sqrt{\omega_r\omega_q}$. The above equation is of course only approximate, but this conclusion holds for the full photon number Eq. (5.18) as well. For extremely strong couplings we can derive the limit, to leading order in G^{-1} ,

$$\langle a^\dagger a \rangle \approx \frac{G}{4\omega_r\omega_q} - \frac{1}{2}, \quad (5.20)$$

that is the photon number is linear in the collective coupling for $G \gg \omega_r, \omega_q$. A result very different to what one expects from the DM, $\langle a^\dagger a \rangle \propto G^2$.

5.1.2 Light-matter decoupling: the subradiant phase

Taking $N \rightarrow \infty$ for the bosonization also implies that the single qubit-photon coupling $g \rightarrow 0$, in order to keep the collective coupling $G = \sqrt{N}g$ finite. In the following we are interested in $N > 1$ and $g > \omega_r, \omega_q$, where a few qubits and the resonator are ultra-strongly coupled in the single qubit-photon regime.

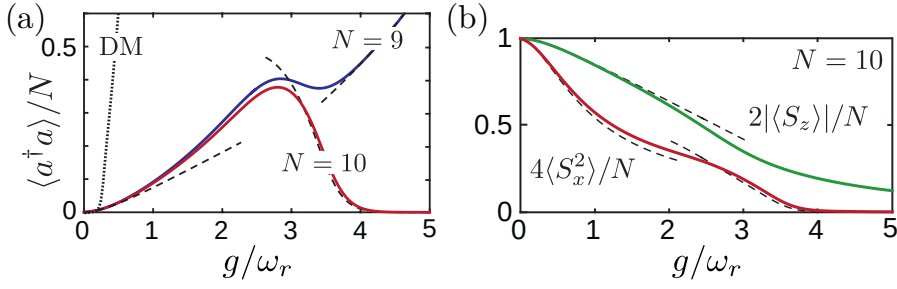


Figure 5.1: (a) Photon number per qubit $\langle a^\dagger a \rangle / N$ in the ground state of the EDM. The photon number is plotted against the coupling for $N = 10$ and $N = 9$ qubits. The dotted line is the DM prediction which diverges at the critical coupling g_c . The dashed lines are analytical predictions from the Holstein-Primakoff Hamiltonian, for small g , and the effective Hamiltonian Eq. (5.25) for large g . (b) The spin observables $2|\langle S_z \rangle| / N$ and $4\langle S_x^2 \rangle / N$ plotted as a function of the coupling for $N = 10$ qubits. The dashed lines are as in (a). For $\langle S_z \rangle$ the effective Hamiltonian Eq. (5.25) is inaccurate and also corrections to the eigenstates have to be taken into account in order to quantitatively match the $g \gg \omega_r$ result, see App. B. The behaviour of $\langle S_z \rangle$ and $\langle S_x^2 \rangle$ for $N = 9$ qubits is qualitatively same, the only difference being that $\langle S_x^2 \rangle \rightarrow 1/4$ rather than to 0 for large couplings g .

In this regime the non-linearity of the spins plays a central role in the physics and the Holstein-Primakoff Hamiltonian loses its applicability. In order to tackle the problem in this regime we use exact numerical diagonalization techniques and strong coupling perturbation theory.

In Fig. 5.1(a) we plot the ground-state photon number per qubit $\langle a^\dagger a \rangle / N$ for the EDM as a function of the coupling g . We plot it for $\omega_q / \omega_r = 0.5$ and for 9 and 10 qubits coupled to the resonator. The behaviour for small g , up to $g \approx \omega_r$, is well predicted by the linearised Holstein-Primakoff Hamiltonian Eq. (5.6). For larger couplings the behaviour for 9 and 10 qubits, surprisingly, start to deviate from each other. Especially, for 10 qubits the photon number reaches a maximum at a finite g and then *decreases* approaching 0 as $g \rightarrow \infty$. On the other hand, for 9 qubits there is a small plateau where the 10 qubit system reaches its maximum, but then the photon number increases again monotonically. This is completely unexpected from the perspective of the Dicke model, where there is no difference between an odd or even amount of coupled qubits, nor can the photon number decrease for increasing coupling.

How can these findings be understood? A rough argument can be made just based on the magnitudes of the coefficients of the different terms in the EDM Hamiltonian Eq. (4.33). When the coupling energy is the dominant energy scale

$g > \omega_r, \omega_q$ the S_x^2 -term in the Hamiltonian is the most dominant part. Since the eigenvalues of S_x^2 are positive the minimal energy penalty from this term comes from states with the minimal eigenvalue. For an even number of qubits this will be the eigenstate $|m_x\rangle$ of S_x for which $m_x = 0$, such that also $S_x^2|m_x = 0\rangle = 0$. However for an odd number of coupled qubits the total spin is a half-integer $s = N/2 = k + 1/2$ for some $k \in \mathbb{N}$, such that the possible values for m_x are also half integers $m_x = -s, \dots, -1/2, 1/2, \dots, s$ and there is no state for which $m_x = 0$. Thus, the energy is minimized by two states, namely $|m_x = \pm 1/2\rangle$. The coupling term between the resonator and the qubits then displaces the oscillator by an amount $\pm g(a^\dagger + a)/2$ depending on the qubit state. The ground state is, thus, an entangled state of the form $|\text{GS}\rangle \simeq (|\alpha, -1/2\rangle + |-\alpha, 1/2\rangle)/\sqrt{2}$, where $\alpha = g/(2\omega_r)$ is the amplitude of the resonator coherent state. The photon number of this state is $\langle a^\dagger a \rangle = |\alpha|^2 \propto g^2$ rather than g as we derived from the Holstein-Primakoff Hamiltonian for large G . This, difference is a signal of the non-linear effect of the TLSs. For an even qubit number the coupling to the resonator vanishes altogether $g(a^\dagger + a)m_x \rightarrow 0$. Thus, the ground state of the system will be a product state of the oscillator vacuum state and the $|m_x = 0\rangle$ state, $|\text{GS}\rangle \simeq |0, 0\rangle$, giving a zero photon number. Thus, we have given an intuitive explanation of the observed behaviour of the ground state photon number and the surprising difference for odd/even number of qubits.

The above argument is not quite the complete picture. In considering only the S_x^2 -term we have neglected the effect of the interaction term $H_{\text{int}}g(a^\dagger + a)S_x$. *A priori* it is possible that the lowering of the energy from this term, by displacing the resonator such that the expectation value of the coupling Hamiltonian becomes negative, could compensate the energy penalty compared to the eigenstate with minimal m_x , and lead to a different ground state. We will give the detailed explanation to why this is not the case later in this section. The free qubit Hamiltonian S_z will lead to mixing of different S_x eigenstates and could in principle also change the ordering of the energy levels. However, in the regime $g > \omega_r, \omega_q$ it is highly suppressed, and only weakly mixes the different m_x -states, not affecting the qualitative behaviour we have laid out. This will also be discussed later in the section.

The conclusions made from the simple considerations made above are corroborated by the spin observables shown in Fig. 5.1(b). We plot the expectation values $|\langle S_z \rangle|$ and $\langle S_x^2 \rangle$ normalized by $N/2$ and $N/4$, respectively, for 10 coupled qubits. The absolute value of the z -polarization and the square of the x -polarization both tend to zero for large couplings, as expected from our intuitive picture.

EDM in the polaron frame

It is instructive to move into the polaron frame for the EDM Hamiltonian where the bilinear interaction term is removed. The full derivation is presented in [App. A](#), here we give an outline of the treatment.

We apply the unitary transformation $\mathcal{U} = \exp[\gamma(a^\dagger - a)S_x]$ to [Eq. \(4.33\)](#), with $\gamma = g/\omega_r$. This displaces the annihilation and creation operators to $a^{(\dagger)} \rightarrow a^{(\dagger)} - \gamma S_x$. The S_x dependent parts do not change since $[S_x, \mathcal{U}] = 0$. The free qubit Hamiltonian is rotated by an amount dependent on the resonator to

$$S_z \rightarrow \cos(i\gamma(a^\dagger - a))S_z - \sin(i\gamma(a^\dagger - a))S_y. \quad (5.21)$$

Using these substitutions the transformed Hamiltonian is given by

$$H_{\text{pol}} = \omega_r a^\dagger a + \frac{\omega_q}{2} \left(\mathcal{D}(-\gamma)\tilde{S}_+ + \mathcal{D}(\gamma)\tilde{S}_- \right), \quad (5.22)$$

where $\mathcal{D}(\alpha) = \exp(\alpha a^\dagger - \alpha^* a)$ is the displacement operator and $\tilde{S}_\pm = S_z \pm iS_y$ are the ladder operators with respect to the S_x eigenbasis.

By moving into the polaron frame we have removed both the linear coupling to the cavity and the S_x^2 -term. Moreover, the free qubit Hamiltonian H_{pol}^z , second term in [Eq. \(5.22\)](#), is heavily suppressed for $g > \omega_r, \omega_q$, $H_{\text{pol}}^z \propto \omega_q e^{-\gamma^2/2}$. Thus, to lowest order in ω_q/g the resonator and the qubits are decoupled, and *all the 2^N qubit eigenstates are degenerate*. This is in conflict of our simple treatment where we concluded that the eigenstate, or states, with the minimal S_x quantum number will be the ground state. The reason for the exponential degeneracy is the interaction term H_{int} as we anticipated. However, this result is also in conflict with our numerical results for $\langle S_x^2 \rangle$, which shows clearly that the state of the qubits approaches the state with the minimal S_x eigenvalue.

Effective low-energy Hamiltonian

The reason for this discrepancy is the importance of quantum fluctuations due to H_{pol}^z [[50](#), [51](#)]. In [App. B](#) we calculate the effective Hamiltonian in the 0 photon subspace $\{|n=0, s, m_x\rangle\}_{s, m_x}$ for the EDM up to second order in the perturbation H_{pol}^z . The first order perturbative correction is exponentially suppressed in $\gamma = g/\omega_r$

$$H_{\text{eff}}^{(1)} = \omega_q e^{-\gamma^2/2} S_z. \quad (5.23)$$

Surprisingly the second order correction does not go exponentially in the coupling, rather it is polynomial in ω_q/g

$$H_{\text{eff}}^{(2)} = \frac{\omega_r \omega_q^2}{2g^2} (S_x^2 - \mathbf{S}^2), \quad (5.24)$$

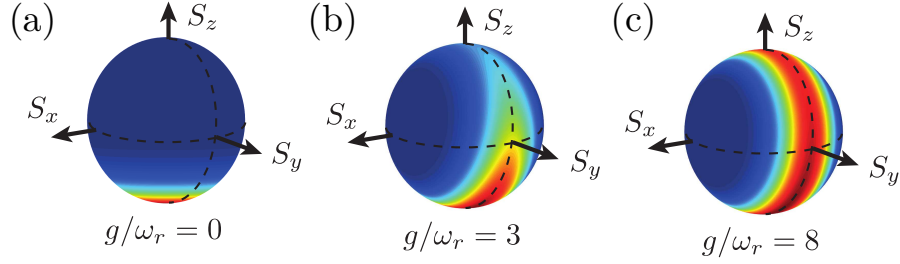


Figure 5.2: SU(2) Q -functions of the reduced qubit states $\rho_q = \text{Tr}_c[\rho]$. (a) For small couplings the qubit state is close to a coherent spin state at the south pole of the Bloch-sphere. (b) For increasing coupling the state is squeezed along x . (c) In the limit $g \rightarrow \infty$ the state approaches a narrow circle in the plane $S_x = 0$.

where \mathbf{S} is the total spin operator. In this result we have neglected an exponentially suppressed term that couples different m_x states, and assumed $\gamma \gtrsim 2$ in order to simplify $H_{\text{eff}}^{(2)}$ to the form given above, see [App. B](#).

Interestingly, coupling to the higher photon number manifolds $n \neq 0$ induces strong shifts of the energies of the spin states. Since the second order term is not exponentially suppressed, it determines the ordering of the energy levels rather than $H_{\text{eff}}^{(1)}$. The effective Hamiltonian describing the ground state photon manifold $n = 0$ is then

$$H_{\text{eff}} = \omega_q e^{-\gamma^2/2} S_z + \frac{\omega_r \omega_q^2}{2g^2} (S_x^2 - \mathbf{S}^2). \quad (5.25)$$

Thus, we see that our simple argument produced the correct result; the ground state of the system has a minimal S_x quantum number. Moreover, from $H_{\text{eff}}^{(2)}$ we see that the ground state is in the maximal total spin subspace $s = N/2$, which we could not deduce from our simple argument, but what we implicitly assumed anyway.

In the polaron frame the resonator and the qubits are decoupled in the low-energy sector of the Hilbert space and the ground state for a system with odd number of qubits is $|\text{GS}\rangle = (|s = N/2, m_x = -1/2\rangle + |s = N/2, m_x = 1/2\rangle) \otimes |n = 0\rangle / \sqrt{2}$ and for even qubit number $|\text{GS}\rangle = |s = N/2, m_x = 0\rangle \otimes |n = 0\rangle$. Moving back to the original frame with \mathcal{U}^{-1} gives the ground state deduced from the simple argument.

In [Fig. 5.2](#) we show the SU(2) Q -function of the reduced density matrix of the qubits, $Q(\hat{\mathbf{n}}) = \langle \hat{\mathbf{n}} | \rho_q | \hat{\mathbf{n}} \rangle$, where $\hat{\mathbf{n}}$ is a unit vector on the Bloch-sphere and $|\hat{\mathbf{n}}\rangle$ is the corresponding spin-coherent state. The plot is for $N = 10$ and shows three different couplings $g/\omega_r = 0, 3, 8$. As the coupling is increased the initial spin coherent state $|s = N/2, m_z = -N/2\rangle$ is squeezed along x , and approaches a ring

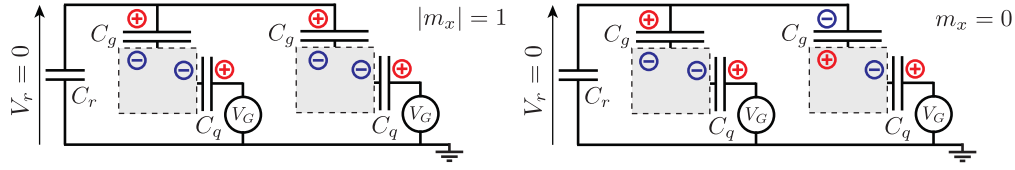


Figure 5.3: Charge configurations of Fig. 4.2 corresponding to a states $|m_x| = 1$, left, and $m_x = 0$ right. The DM would predict an energy difference for the presented configurations even though they differ only by the sign of the charge on the coupling capacitor C_g . In the EDM this energy difference is not present. The inductive parts of the circuit have been left out for clarity.

in the $x = 0$ plane for large couplings g .

Now that we have understood the behaviour of the ground state of the system for different couplings, we are in place to understand the importance of the S_x^2 term. Consider the e.g. the circuit of Fig. 4.2 in the regime where the inductive energies E_J and $E_L = \Phi_0^2/L$ are negligible compared to the capacitive contribution. If there would be no S_x^2 term in the Hamiltonian the charge configurations depicted in Fig. 5.3, corresponding to $m_x = 0$ and $|m_x| = 1$, would have different energies. In both of the configurations the energy is stored as the charging energy $Q^2/(2C_g)$ of the coupling capacitor C_g , and the charge on the resonator capacitor plate C_r vanishes, such that the voltage across it also vanishes. The only difference in the two configurations is the sign of the charge on one of the coupling capacitors. This however cannot lead to an energy difference since the charging energy is quadratic in the charge. Thus, the Dicke model is in conflict with basic electrostatic considerations by predicting an energy difference between these equivalent charge configurations. This, discrepancy is fixed by the inclusion of the S_x^2 term which correctly gives the degeneracy of all the charge configurations.

Even though we have derived the effective spin Hamiltonian Eq. (5.25) for the ground state manifold $n = 0$ it has predictive power also in the excited manifolds $n > 0$, see Fig. 5.4. We see that also in these manifolds 2^N fold degeneracies start to form when the coupling $g \gg \omega_r, \omega_q$. This means that for a few of the lowest excited manifolds the eigenstates will have the same form as in the ground state manifold $|\psi_{n,s,m_x}\rangle = |n\rangle |s, m_x\rangle$.

Ground state entanglement

It is interesting that, for an even number of qubits, increasing the qubit-oscillator coupling leads to a complete decoupling of the two. Even though the resonator and the qubits are not entangled, the state of the qubits' is highly entangled. Entanglement between subsystems A and B of a composite system $\mathcal{H}_A \otimes \mathcal{H}_B$

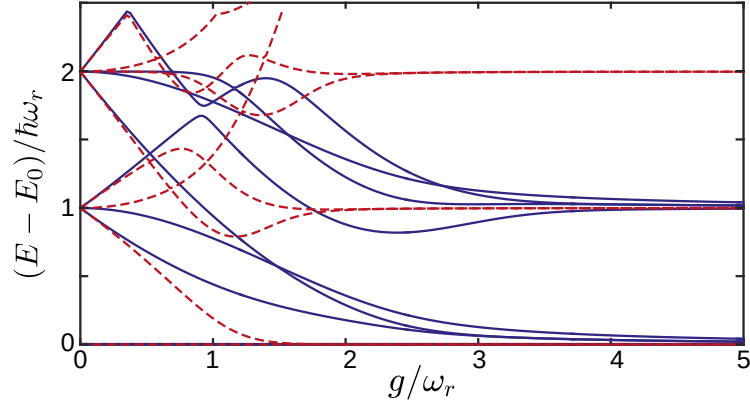


Figure 5.4: The spectrum of the EDM, solid blue lines, and the DM, red dashed lines, plotted against the coupling strength g . The behaviour of the spectrum in the single qubit-photon USC regime in the two models is completely different. Rather than forming degenerate manifolds of pairs of superradiant states, in the EDM manifolds of 2^N fold degeneracy are formed. The plot is for $N = 2$ qubits.

can be quantified with *entropy of entanglement* \mathcal{S}_E , defined as the *von Neumann* entropy of the reduced density matrix of one of the subsystems

$$\mathcal{S}_E = -\text{Tr}(\rho_A \log(\rho_A)) = -\text{Tr}(\rho_B \log(\rho_B)), \quad (5.26)$$

where $\rho_{A(B)} = \text{Tr}_{B(A)}(\rho)$ is the reduced density matrix of subsystem $A(B)$ and \log is the base two logarithm.

In Fig. 5.5 we plot the entanglement entropies of the reduced qubit density matrix $\rho_q = \text{Tr}_r(\rho)$ and the reduced single qubit density operator $\rho_1 = \text{Tr}_{N-1}(\rho_q)$, \mathcal{S}_q and \mathcal{S}_1 respectively, for a $N = 10$ qubit system. The entanglement entropy \mathcal{S}_q quantifies the entanglement of the spins with the resonator and \mathcal{S}_1 the entanglement among the qubits. (This is actually not quite true in the case $\mathcal{S}_q \neq 0$, due to the entropy of entanglement being a valid measure only for pure states $\rho = |\psi\rangle\langle\psi|$. We are however only interested in the entanglement between the qubits in the sub-radiant phase when $\mathcal{S}_q \approx 0$, such that \mathcal{S}_1 measures to a very good approximation only the entanglement among the spins.)

Let us first concentrate on \mathcal{S}_q . It follows qualitatively the behaviour of the ground state photon number shown in Fig. 5.1. First there is an increase in the amount of entanglement until at a finite g it reaches a maximum value, after which it decreases monotonously back towards zero as $g \rightarrow \infty$. The entanglement entropy of a single qubit, however, behaves rather differently. At first it increases at a much slower rate than \mathcal{S}_q , but \mathcal{S}_1 continues to increase even after \mathcal{S}_q has

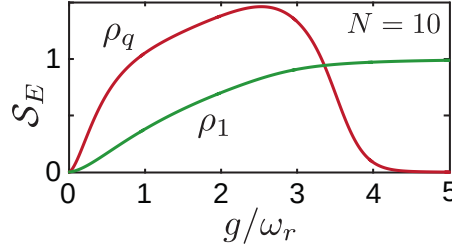


Figure 5.5: Entropy of entanglement for the EDM ground state. \mathcal{S}_q , red line, quantifies the entanglement between the oscillator and the qubits and \mathcal{S}_1 between a single qubit and the rest of the system. When $\mathcal{S}_q \approx 0$ a non-vanishing value of \mathcal{S}_1 signals entanglement among the qubits. For $g \rightarrow \infty$ the single qubit density matrix is a completely mixed state $\rho_1 = I_{2 \times 2}/2$ such that \mathcal{S}_1 saturates to 1.

started to decrease. For $g \rightarrow \infty$ it saturates to $\mathcal{S}_1 = 1$ which is the upper bound, logarithm of the single qubit Hilbert space dimension, $\mathcal{S}_1 = \log(2)$.

We call the regime of parameter space for which the resonator is in a low photon number state and the qubits are in the highly entangled state the *subradiant phase*, as opposed to superradiant phase. It is not, however, a phase in a rigorous sense, rather the transition from the normal phase is a smooth crossover without a closing of an energy gap. This is discussed in more detail in the next section.

5.2 Phase diagram of cavity QED

We want to explore the ground state physics of the cavity QED Hamiltonian Eq. (4.49) as a function of the coupling strength g and the DD coupling strengths D_{ij} . We do this qualitatively using the EMD Hamiltonian. In the previous section we analysed the ground state for non-interacting qubits, $\varepsilon = 0$, and saw that the ground state for large couplings is in the subradiant phase. Here we map the parameter space for arbitrary ε .

In Fig. 5.6 we plot the phase diagram of the cavity QED ground state, with numerical, black solid and dashed lines, and analytical, red dotted line, phase boundaries, for varying effective fine structure constant α and DD interaction strength ε . The effective fine structure constant is defined through

$$\frac{g}{\omega_r} = \sqrt{2\pi\alpha}. \quad (5.27)$$

This is motivated by the relation $g/\omega_r \leq \sqrt{2\pi\alpha_{fs}}$, with $\alpha_{fs} \simeq 1/137$ the fine structure constant, for regular cavity QED systems with atoms in cavities [7, 28,

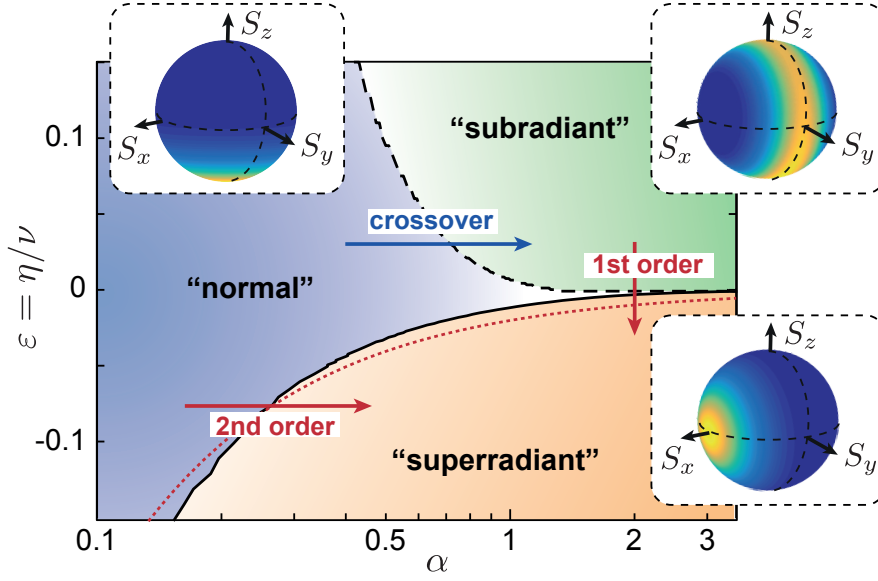


Figure 5.6: Ground state phase diagram of cavity QED. The black lines denote the numerically obtained phase boundaries, solid normal to superradiant and dashed normal to subradiant, and the red dotted line is the analytical phase boundary Eq. (5.35). The insets show the reduced qubit state in each phase, see Sec. 4.3 and Fig. 5.2. The numerical phase boundaries have been obtained for $N = 10$ qubits.

51]¹. Next we will go through the different phases of the ground state, starting with the normal phase.

5.2.1 Normal phase

In the limit of very small coupling $g \ll \omega_r, \omega_q$ the ground state will be the standard uncoupled vacuum state with $\langle a^\dagger a \rangle \simeq 0$ and $\langle S_z \rangle \simeq -N/2$, regardless of the average DD coupling strength. This is the so-called normal phase. Since the coupling is small, the terms proportional to g^2 in the EDM Hamiltonian can be neglected. Additionally a RWA can be performed such that the EDM Hamiltonian reduces to the TC Hamiltonian Eq. (4.5). All the phenomena of the strong coupling regime are then reproduced such as the vacuum Rabi splitting [112] and Rabi oscillations [106] between dressed states.

For couplings large enough to break the RWA we can use the Hollstein-Primakoff approximation to calculate properties of the ground state for finite coupling g , as was done in Sec. 4.3. The bosonic Hamiltonian corresponding to Eq. (4.52) is the

¹Note, that in [7, 28] a resonant coupling is assumed which alters the scaling with α_{fs}

same as Eq. (5.6) with the replacement $G^2/(4\omega_r) \rightarrow (1+\varepsilon)G^2/(4\omega_r)$, in accordance with the additional term $\varepsilon g^2/\omega_r$ in Eq. (4.52),

$$H_{\text{HP}} = \omega_r a^\dagger a + \omega_q b^\dagger b + \frac{G}{2}(a^\dagger + a)(b^\dagger + b) + (1 + \varepsilon) \frac{G^2}{4\omega_r} (b^\dagger + b)^2, \quad (5.28)$$

where we have again introduced the collective coupling $G = \sqrt{N}g$. From the above Hamiltonian we can again calculate e.g. the ground state photon number, which is for $G \ll \omega_r, \omega_q$ given by

$$\langle a^\dagger a \rangle \simeq \frac{Ng^2\omega_q}{4(\omega_q + \omega_r)^2(\omega_q + \varepsilon Ng^2/\omega_r)}, \quad (5.29)$$

in accordance with Eq. (5.19).

For positive ε the normal phase borders the subradiant phase, encountered already for $\varepsilon = 0$ in Sec. 5.1, and for $\varepsilon < 0$ to the superradiant phase. We will come back to the definition of these borders when discussing the respective phase.

5.2.2 Subradiant phase

For larger couplings and $\varepsilon \geq 0$ the system transitions into the subradiant phase with $\langle a^\dagger a \rangle = 0$, but $\langle S_z \rangle = 0$ and $\langle S_x^2 \rangle = 0$ for even number of qubits or $\langle S_x^2 \rangle = 1/4$ for odd numbers, as explained in Sec. 5.1. In the polaron frame we get the following Hamiltonian, see App. A

$$H = \omega_r a^\dagger a + \varepsilon \frac{g^2}{\omega_r} S_x^2, \quad (5.30)$$

where we have neglected the term coming from the free qubit Hamiltonian $\omega_q S_z$. From this Hamiltonian it is clear that the inclusion of repulsive interactions does not qualitatively change the ground state properties for finite coupling since the additional $\varepsilon g^2/\omega_r S_x^2$ term drives the qubits also to states with minimal S_x projection. However, for $g \rightarrow \infty$ the exponential ground state degeneracy is lifted due to the energy penalty to other S_x eigenstates.

In Fig. 5.6 we have used the condition (for even number of qubits)

$$\frac{\partial \langle a^\dagger a \rangle}{\partial g} = 0, \quad (5.31)$$

to define the boundary between the normal and subradiant phases, plotted as the black dashed line. This, condition is satisfied for $\alpha \approx O(1)$, i.e. when the dipole-field coupling becomes non-perturbative. It is interesting that also the linearised Holstein-Primakoff Hamiltonian Eq. (5.28) predicts a maximum of $\langle a^\dagger a \rangle$ at finite

g for $\varepsilon > 0$. In the limit $g \rightarrow \infty$ the ground state photon number of the bosonized Hamiltonian approaches [51]

$$\lim_{g \rightarrow \infty} \langle a^\dagger a \rangle_{\text{HP}} = \frac{1 + 2\varepsilon - 2\sqrt{\varepsilon(\varepsilon + 1)}}{4\sqrt{\varepsilon(\varepsilon + 1)}} > 0. \quad (5.32)$$

Thus, the reduction of the photon number of the full Hamiltonian below this value indicates the emergence of the entangled antiferromagnetic states of the qubits. These states decouple from the cavity much better than the two-mode squeezed states of the bosonic description, resulting in photon numbers well below Eq. (5.32).

Let us for a moment consider a circuit QED realization of Eq. (4.52). The two quadratures of the mode a are $q_r = q_r^{\text{zpf}}(a^\dagger + a)$ and $\phi_r = -i\phi_r^{\text{zpf}}(a^\dagger - a)$. For a charge qubit coupled to an LC -resonator these would correspond to the total resonator charge and its flux. As a more robust sign for the subradiant phase we consider the operator

$$V_r = V_r^{\text{zpf}} \left(a^\dagger + a + \frac{2g}{\omega_r} S_x \right), \quad (5.33)$$

where $V_r^{\text{zpf}} = q_r^{\text{zpf}}/C_r$ is a zero-point amplitude. This operator corresponds to the voltage measured across the resonator capacitor and V_r^{zpf} is the zero-point amplitude of it. The form of V_r follows from the definition

$$V_r = \dot{\phi}_r = -i [H_{\text{EDM}}, q_r], \quad (5.34)$$

where ϕ_r is the flux variable of the resonator. The difference between q_r and V_r is that V_r corresponds only to the charge on the resonator capacitor plate and q_r includes charges on all capacitor plates connected to the node of the resonator, see Fig. 5.3. Especially, considering the setup of Fig. 4.2, q_r includes the charges in the plates of the coupling capacitors C_g which do not create a voltage difference on the resonator capacitance C_r . The charges in the coupling capacitor are created by a finite polarization of the charge qubits, and, thus, the variable q_r contains both resonator and qubit degrees of freedom. A non-zero value of $\langle q_r \rangle$ does not, however, necessarily correspond to a current in the resonator inductor, this is the case only if also $\langle V_r \rangle \neq 0$.

In a more general setting V_r corresponds to the generalized velocity of the generalized coordinate ϕ_r of the electromagnetic mode. The mechanical analog is that V_r corresponds to the kinetic momentum of a particle, which does not have to equal the canonical momentum.

In Fig. 5.7 we plot the variance of V_r in the ground state $\Delta V_r^2 = \langle V_r^2 \rangle - \langle V_r \rangle^2 = \langle V_r^2 \rangle$, since expectation values of a , a^\dagger and S_x vanish due to the parity symmetry of the Hamiltonian. There is a peak in the variance for both even and odd number of

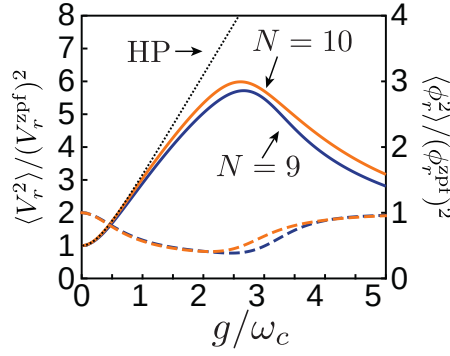


Figure 5.7: Plot of the resonator voltage, solid lines, and flux, dashed lines, fluctuations across the normal-to-subradiant phase boundary. Both odd and even number of qubits have the same qualitative behaviour. The linear Holstein-Primakoff Hamiltonian, black dotted line only for $\langle V_r^2 \rangle$, cannot reproduce the features of the full Hamiltonian for large single-atom photon coupling g .

qubits at $\alpha \approx 1$, and the position does not depend sensitively on ε or N [51]. The absence of even-odd effects in the variance makes it a good signature of reaching the subradiant regime. In Fig. 5.7 we plot also the variance of the resonator flux variable $\Delta\phi_r^2$. It displays a dip at the point of the voltage peak, however, the variances are larger than those for a minimum uncertainty state.

The transition from the normal phase to the subradiant phase is not a phase transition in the strict sense. There is no closing of an energy gap, in the thermodynamic limit, when passing to the subradiant phase. Rather the two phases are continuously connected to each other in a crossover manner. However, the two phases are clearly qualitatively different.

5.2.3 Superradiant phase

For on average attractive dipole-dipole interactions $\varepsilon < 0$ the normal phase becomes unstable for larger couplings, and the system enters into the superradiant phase. This transition is similar to the Dicke superradiant phase transition, however, the interpretation of the transition is different.

As in the Dicke model it is possible to quantify the phase transition using the bosonized Holstein-Primakoff Hamiltonian. The Hamiltonian is that of Eq. (5.28) with $\varepsilon < 0$. From the Hamiltonian we can obtain the normal mode frequencies ω_{\pm} as in Sec. 4.3. The condition for the superradiant phase transition from $\omega_- = 0$

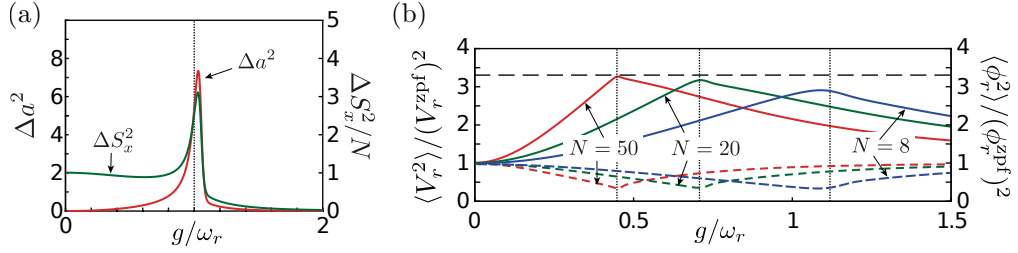


Figure 5.8: Superradiant phase (a) The fluctuations of the field, Δa^2 , and the spin, ΔS_x^2 , across the phase boundary. The peaks of the fluctuations are close to the analytical transition point, marked by the dotted line. (b) Fluctuations of the resonator voltage, $\langle V_r^2 \rangle$ solid lines, and flux, $\langle \phi_r^2 \rangle$ dashed lines, across the phase boundary for $N = 8, 20, 50$ qubits. The dashed horizontal line marks the analytical prediction Eq. (5.37) and matches the numerical result well for large N . For all of the plots we have used $\omega_q = \omega_r$, $\varepsilon = -0.1$ and a symmetry breaking field $\propto S_x$ of $10^{-3}\omega_q$.

becomes [51]

$$g > g_c = \sqrt{\frac{\omega_r \omega_q}{-\varepsilon N}}, \quad (5.35)$$

which is plotted as the red dotted line in Fig. 5.6. The transition point is qualitatively same as for the Dicke model, but has been scaled by a factor $(-\varepsilon)^{-1/2}$, and the transition is possible only for $\varepsilon < 0$, i.e. for attractive dipole-dipole interactions. As discussed in Sec. 4.2 the superradiant phase is characterized by finite expectation values of a and S_x

$$\langle S_x \rangle = \pm \frac{N}{2} \sqrt{1 - \left(\frac{g_c}{g}\right)^4}, \quad \langle a \rangle = -\frac{g}{\omega_r} \langle S_x \rangle. \quad (5.36)$$

The transition into the superradiant phase is signalled by a sharp peak in the variance of the qubit polarization $\Delta S_x^2 = \langle S_x^2 \rangle - \langle S_x \rangle^2$ and the field amplitude $\Delta a^2 = \langle a^\dagger a \rangle - |\langle a \rangle|^2$ as shown in Fig. 5.8(a). The fluctuations of the qubit polarization ΔS_x^2 are used in Fig. 5.7 to numerically obtain the phase boundary between the normal and superradiant vacuums. The discrepancy between the analytical and numerical phase boundaries in the limit of small single photon-atom coupling, but large collective coupling, $g \ll \omega_r, \omega_q$ is due to finite size effects and would go away in the thermodynamic limit. The discrepancy in the limit of large g is a quantum effect which we discuss in a moment.

In Fig. 5.8(b) we plot the fluctuations $\langle V_r^2 \rangle$ of the voltage operator, introduced in Eq. (5.33), and of ϕ_r . Again there is a peak in the voltage fluctuations, cor-

respondingly a dip in the flux fluctuations, and they coincides with the phase transition point. Note, however, that now the averages of S_x and a do not vanish, implying a finite value of q_r . Regardless of this the average value of V_r still vanishes due to Eq. (5.36), which means $\langle q_r \rangle \neq 0$ corresponds to a static charge not leading to a current in the resonator inductor. This means that the properties of the resonator alone, i.e. the voltage V_r and flux ϕ_r are not affected by the transition in the mean field level.

Unlike in the transition to the subradiant regime the peak of $\langle V_r^2 \rangle$ gets sharper for increasing qubit amount, turning into a cusp at the critical coupling g_c in the thermodynamic limit. The maximum of the voltage fluctuations can be calculated from the linearised theory to be

$$\frac{\langle V_r^2 \rangle}{(V_r^{\text{zpf}})^2} \approx \sqrt{1 + \frac{1}{|\varepsilon|} \left(\frac{\omega_q}{\omega_r} \right)^2}. \quad (5.37)$$

Surprisingly the maximum is independent of the number of qubits. For an interaction dominated system, $|\varepsilon| \rightarrow \infty$, the peak vanishes. Thus, it can be interpreted as a quantum signature of the phase transition which involves the dynamical cavity mode.

Based on our findings we can reinterpret the superradiant phase transition as an instability in the collection of qubits, driven by the attractive dipole-dipole interactions, which is there regardless of the presence of the field mode. This, interpretation is supported by the fact that the mean field properties of the mode alone do not change at the phase transition point. The presence of the mode can, however, affect the quantitative details of the precursor of the phase transition for moderate number of qubits N and strong single atom-photon coupling. To illustrate this we compare the EDM with the corresponding Lipkin-Meshkov-Glick (LMG) Hamiltonian [113]

$$H_{\text{LMG}} = \omega_q S_z + \varepsilon \frac{g^2}{\omega_r} S_x^2, \quad (5.38)$$

which presents a ferromagnetic phase transition at the critical coupling g_c of the DM in the thermodynamic limit. In Fig. 5.9(a) we plot the fluctuations ΔS_x^2 of the DM and LMG for different $|\varepsilon|N$ across the phase transition point. We see when $|\varepsilon|N \lesssim 1$, i.e. when the transition point requires a rather large g , that the coupling to the cavity in the Dicke model reduces fluctuations of the spin and stabilizes the ferromagnetic phase for smaller couplings than in the LMG. For larger $|\varepsilon|N$ the predictions from the two Hamiltonians become closer to each other as is expected due to the reduction of the importance of quantum effects and better validity of the mean field description, see Fig. 5.9(b). The cavity's tendency to reduce fluctuations is understood by the dressing of the spins by photons. The dressed

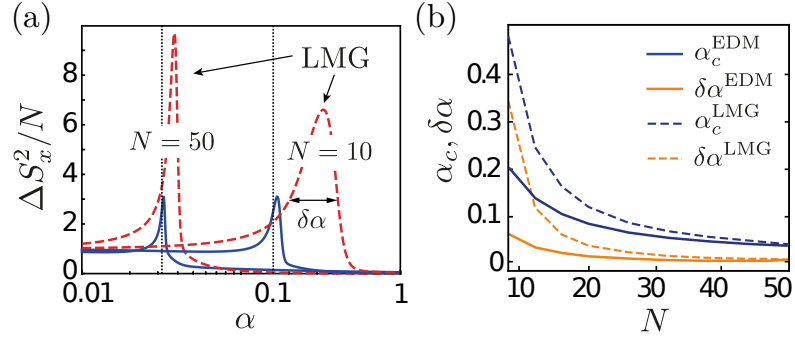


Figure 5.9: Comparison of the EDM and the corresponding LMG Hamiltonian. (a) The fluctuations of S_x from the EDM, solid lines, and the LMG, dashed lines, for $N = 10, 50$ as a function of the effective fine structure constant. (b) The critical coupling α_c and the width of the peak of the spin fluctuations of (a). For $N \rightarrow \infty$ the EDM and LMG model give the same results, indicating that the cavity mode has no effect on the spins. We have taken $\omega_q = \omega_r$ and $\varepsilon = -0.1$ for the plots. A bias field $H_{\text{bias}} = 10^{-3}\omega_q S_x$ is used to deterministically pick one of the degenerate minima.

spin effectively experiences a smaller ω_q reduced roughly by the overlap of the cavity states corresponding to the two superradiant spin states.

5.2.4 Super- to subradiant phase transition

In the previous section we saw that the subradiant and superradiant phase boundaries merge in the limit of strong couplings $g/\omega_r > 1$, resulting in a direct transition between the two phases. In this regime the mean field description is not valid anymore and we need to take into account the full non-linearity of the qubits. Consider the effective pure spin Hamiltonian for the low energy physics in the EDM

$$H_S = \omega_q e^{-g^2/(2\omega_r^2)} S_z + \frac{\omega_r \omega_q^2}{2g^2} (S_x^2 - \mathbf{S}^2) + \varepsilon \frac{g^2}{\omega_r} S_x^2. \quad (5.39)$$

In this Hamiltonian we clearly see the suppression of tunnelling due to the polaronic nature of the eigenstates, responsible for the reduced fluctuations in the EDM compared to the LMG model observed in the previous section. The interplay between the two S_x^2 terms in the Hamiltonian decides the ground state phase of the system. For $\varepsilon > 0$ the term will be positive resulting in a subradiant order. For attractive dipole-dipole interactions there is a competition between the two terms and a critical $\varepsilon_c < 0$ emerges at which the transition to the superradiant state takes place. We can use the Holstein-Primakoff approximation of the spin

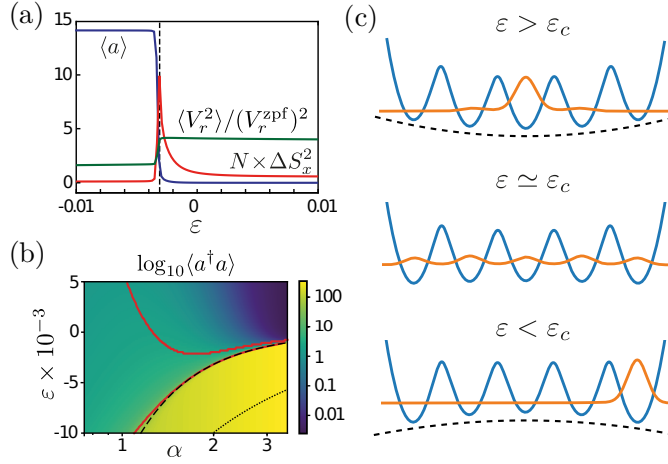


Figure 5.10: (a) The voltage and spin fluctuations and the mean cavity field across the super-to-subradiant phase transition. The effective fine structure constant is $\alpha = 2$. (b) Zoom of the phase diagram Fig. 5.6 around $\varepsilon = 0$. Red solid lines denote the numerical phase boundaries, the dashed line is the critical DD coupling strength Eq. (5.42), and the dotted line the standard phase boundary Eq. (5.35). (c) Born-Oppenheimer potentials of the oscillator for the ground state of the EDM, see Chap. 6. For $\varepsilon > \varepsilon_c$ the wave function of the oscillator is concentrated around $X = 0$. Around the critical point the state spreads to occupy all of the different degenerate minima. For $\varepsilon < \varepsilon_c$ the wave function randomly collapses to one of the two degenerate minima corresponding to the superradiant qubit states $|m_x = \pm N/2\rangle$. We have used a symmetry breaking field $\propto S_x$ of $10^{-3}\omega_q$ in all plots and $\omega_q = \omega_r$. For (a) and (b) we have used eight qubits and for (c) four.

Hamiltonian H_S to obtain the condition for the phase transition

$$\omega_q e^{-g^2/(2\omega_r^2)} + N \left(\varepsilon \frac{g^2}{\omega_r} + \frac{\omega_r \omega_q^2}{2g^2} \right) = 0. \quad (5.40)$$

We can now explain the discrepancy observed in the previous between the numerically obtained and analytic phase boundary of the superradiant regime. By neglecting the second term in the parentheses we get a critical coupling

$$g_c = \sqrt{\frac{\omega_r \omega_q}{-\varepsilon N}} e^{-g^2/(4\omega_r^2)}, \quad (5.41)$$

which corresponds to the previously obtained critical coupling but with an exponentially suppressed qubit frequency. This leads to a much smaller critical coupling for $g/\omega_r > 1$. Neglecting the exponentially suppressed qubit frequency gives us a

critical DD coupling strength

$$\varepsilon_c = -\frac{\omega_q^2 \omega_r^2}{2g^4}, \quad (5.42)$$

which is independent of N . For large couplings at this point the system transitions directly from the superradiant to the subradiant phase. For smaller couplings the transition happens through the normal phase. In Fig. 5.10(b) we plot a zoom of the phase diagram around $|\varepsilon| \ll 1$ and for $\alpha \gtrsim 1$ and compare the analytic expression Eq. (5.42) to the numerically obtained one. The agreement is very good for sufficiently strong couplings and we see clearly that the subradiant vacuum extends to negative values of ε as predicted by Eq. (5.42). Thus, the fluctuations induced by coupling of the spin states to higher photon manifolds $n > 0$ stabilize the subradiant state against small attractive DD interactions. In Fig. 5.10(a) we show $\langle a \rangle$, $\langle V_r^2 \rangle$ and ΔS_x^2 along a sweep in ε for large g/ω_r . All of the expectation values show a discontinuous behaviour at the boundary of the two phases, reminiscent of a first order phase transition. However, the situation is more complex in our case. In a first order phase transition there are two minima which cross each other at the critical point resulting in a discontinuous behaviour. In the super-to-subradiant transition there are $2s + 1 = N + 1$ minima involved in the process. In Fig. 5.10(c) we plot the adiabatic Born-Oppenheimer potential $V_{\text{BO}}(X) = X^2/2 + E_0(X)$, where $X = (a^\dagger + a)/\sqrt{2}$ and $E_0(X)$ is the ground state of the spin part

$$H_{\text{EDM}}(X) = \omega_q S_z + \sqrt{2}gX S_x + (1 + \varepsilon) \frac{g^2}{\omega_r} S_x^2, \quad (5.43)$$

for different ε . At ε_c all of the different minima become degenerate.

Chapter 6

Ultra-strong coupling radio-frequency circuit QED

In the previous chapters we have mainly explored the ground state properties of USC systems. In this chapter we expand our analysis to excited states. Another drastic difference is the parameter regime we are considering. Previously the cavity mode and the qubits have had comparable frequencies, $\omega_r \sim \omega_q$. In this chapter however we consider the extremely dispersive limit $\omega_q \gg \omega_r$ while maintaining strong interactions $g^2/\omega_r \sim \omega_q$. In this regime the mode can be treated adiabatically and described as an effective particle moving in a potential created by the qubits. In the Rabi- and Dicke model this regime has already been studied in previous works [114–122], but the emphasis has been on the ground state potential. It has been shown that already for a single qubit coupled to a low-frequency mode a ground-, excited- and dynamical phase transitions can be obtained in the limit of $\omega_r \rightarrow 0$ [119–122]. In studying only the ground-state potential, the energy scales at which the physics takes place is given by that of ω_r which is the smallest energy scale in the problem. Probing the system at this small energy scale can be challenging. For example, in circuit QED standard measurement techniques work efficiently only for frequencies $\gtrsim 1$ GHz. By considering physics in the excited qubit potentials, we gain the benefit of being able to utilize standard measurements and techniques in probing the system.

We consider a generic circuit- or cavity-QED system described by the general Hamiltonian Eq. (4.49) ($\hbar = 1$)

$$H_{\text{cQED}} = \omega_r a^\dagger a + \sum_i \frac{\omega_i}{2} \sigma_i^z + \frac{g_i}{2} (a^\dagger + a) \sigma_i^x + \sum_j \frac{g_i g_j}{4\omega_r} (1 + D_{ij}) \sigma_i^x \sigma_j^x. \quad (6.1)$$

For concreteness imagine, for example, an *LC*-resonator coupled to flux qubits, see Fig. 6.1(a). The dipole-dipole interactions can arise, for example, from placing the flux qubits near each other such that they have mutual inductance, or by coupling

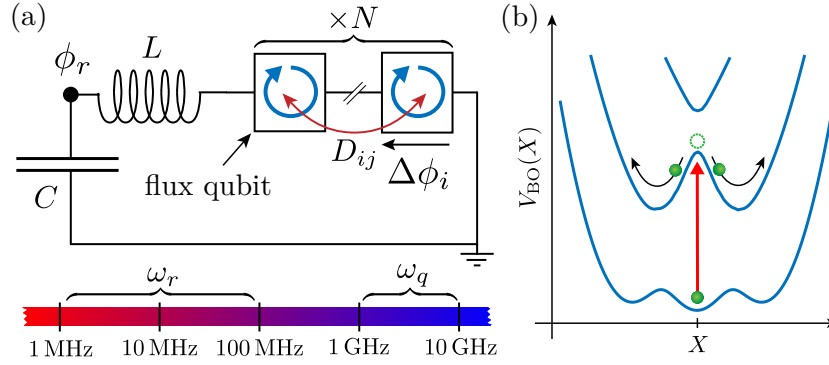


Figure 6.1: (a) Multiple flux qubits coupled to an LC -oscillator. Additional direct dipole-dipole interactions can be engineered by coupling the qubits to SQUID loops. (b) When $\omega_r \ll \omega_q$ the dynamics of the electromagnetic mode are identical to a particle moving in an effective potential created by the qubits.

them to auxiliary SQUIDS [123]. The sign and magnitude of D_{ij} can be tuned *in situ* in the latter case by bias currents applied to the SQUIDS [123]. In what follows we assume for simplicity that the qubits are identical and that they couple to the cavity with a uniform strength. We treat the dipole-dipole interactions in the collective approximation and replace them by their average as in Chap. 5. The resulting Hamiltonian is that of the extended Dicke model

$$H_{\text{EDM}} = \omega_r a^\dagger a + \omega_q S_z + g(a^\dagger + a)S_x + (1 + \varepsilon) \frac{g^2}{\omega_r} S_x^2. \quad (6.2)$$

Note, the qualitative results presented in the following do not require perfectly identical qubits. However, we do require that the \mathbb{Z}_2 symmetry of the Hamiltonian, $a \rightarrow -a$ and $\sigma_i^x \rightarrow -\sigma_i^x$, is preserved by any imperfections.

6.1 Born-Oppenheimer approximation

In the regime $\omega_q \gg \omega_r$ the qubit variables are fast and respond adiabatically to the slowly varying field of the oscillator. The concept of a photon and Fock-states are not useful in this regime anymore, and it is beneficial to use a particle in a potential picture for the resonator, see Fig. 6.1(b).

To describe the system we introduce the rescaled quadratures

$$X = \sqrt{\frac{\omega_r}{2\omega_q}}(a^\dagger + a), \quad P = i\sqrt{\frac{\omega_q}{2\omega_r}}(a^\dagger - a), \quad (6.3)$$

for the oscillator mode which correspond to the standard position and momentum operators of the harmonic oscillator. The EDM Hamiltonian written in the quadrature variables and renormalized by the qubit frequency, $\tilde{H}_{\text{EDM}} = H_{\text{EDM}}/\omega_q$, becomes

$$\tilde{H}_{\text{EDM}} = \frac{P^2}{2\mu} + \frac{X^2}{2} + \tilde{H}_q(X), \quad (6.4)$$

where $\mu = (\omega_q/\omega_r)^2$ is the effective mass of the oscillator and

$$\tilde{H}_q = S_z + \sqrt{2}\lambda X S_x + (1 + \varepsilon)\lambda^2 S_x^2. \quad (6.5)$$

Above we have defined the dimensionless coupling constant $\lambda = g/\sqrt{\omega_q\omega_r}$. For large frequency ratios ω_q/ω_r , i.e. large effective mass, Eq. (6.4) shows that the kinetic energy term $\sim P^2$ is much smaller than the other terms in the Hamiltonian. Thus, in analogy to electron-nucleus systems we can employ the Born-Oppenheimer (BO) approximation [124] to separate the fast dynamics of the qubits from that of the slow oscillator. In the BO limit the eigenstates of the system are given by [116, 117]

$$|\psi\rangle_{n,k} = \int dX \phi_{n,k}(X) |X\rangle |\chi_n(X)\rangle, \quad (6.6)$$

where $|\chi_n(X)\rangle$ is the adiabatic eigenstate of the qubit which solves the Schrödinger equation

$$\tilde{H}_q |\chi_n(X)\rangle = \tilde{E}_n(X) |\chi_n(X)\rangle, \quad (6.7)$$

for every value of X . Since the adiabatic eigenvalue $\tilde{E}_n(X)$ depends on the oscillator coordinate X it provides an additional effective potential to the resonator who follows the Schrödinger equation

$$\left[-\frac{1}{2\mu} \frac{d^2}{dX^2} + \tilde{V}_n(X) \right] \phi_{n,k} = \epsilon_{n,k} \phi_{n,k}. \quad (6.8)$$

Above $\tilde{V}_n(X) = X^2/2 + \tilde{E}_n(X)$ is the total BO potential of the mode resulting from qubit eigenstate n . The BO potentials are even functions of X due to the \mathbb{Z}_2 symmetry of the Hamiltonian.

In the Born-Oppenheimer approximation the coupling of the adiabatic qubit eigenstates $|\chi_n(X)\rangle$ are neglected. The leading coupling terms, which couple Eq. (6.8) for different n , are given by

$$C_{n,m} = \frac{1}{\mu} \frac{\partial \phi_{n,k}}{\partial X} \frac{\langle \chi_m(X) | \sqrt{2}\lambda S_x | \chi_n(X) \rangle}{\tilde{E}_n(X) - \tilde{E}_m(X)}, \quad (6.9)$$

where we have used $\langle \chi_m(X) | \partial_X | \chi_n(X) \rangle = \langle \chi_m(X) | \partial_X \tilde{H}_q | \chi_n(X) \rangle / [\tilde{E}_n(X) - \tilde{E}_m(X)]$ with $\partial_X = \partial/(\partial X)$. Near the potential minimum we can approximate the eigenstates $\phi_{n,k}(X)$ with harmonic oscillator eigenfunctions, such that $\partial_X \phi_{n,k} \sim \sqrt{\mu}$ resulting in a scaling $C_{n,m} \sim \lambda/\sqrt{\mu}$.

As we will show, for larger couplings some of the excited state effective potentials are separated by higher-order avoided crossings, in which case the energy difference $|\tilde{E}_n(X) - \tilde{E}_m(X)| \ll 1$. In these cases corrections beyond the BO treatment may become relevant. In situations we are interested in, however, the BO approximation is well-satisfied, which we have confirmed by comparison to the numerically exact solution.

6.2 Adiabatic potential structures

In this section we explore the potential structures resulting from $H_q(X)$ as a function of the coupling parameters λ and ε and the number of qubits N .

6.2.1 Ground state instability

We start with the simplest situation of a single qubit coupled to the resonator. In this case H_{EDM} reduces to the quantum Rabi Hamiltonian. In Fig. 6.2(a) and (b) we plot the BO potentials $V_{0/1}(X)$ for two different coupling strengths. For small couplings the potentials are almost harmonic and only slightly perturbed by the coupling to the qubit. For larger couplings the ground state potential becomes flatter and flatter, and at a critical coupling $\lambda_c = 1$ it transforms into a double-well, with minima at $X_{\text{min}} = \pm \sqrt{\lambda^4 - \lambda_c^4}/(\sqrt{2}\lambda_c^2\lambda)$. The same qualitative behaviour occurs also in the N -qubit Dicke model, see Fig. 6.2(c) for $N = 2$, which is obtained by setting $\varepsilon = -1$ in the Hamiltonian. In this setting of strong attractive DD interactions the potentials have an analytic form given by [97, 116]

$$\tilde{V}_{s,m_z}^{\text{DM}}(X) = \frac{X^2}{2} + m_z \sqrt{1 + 2(\lambda X)^2}, \quad (6.10)$$

and are labelled by the total spin quantum number $s = 0, 1, \dots, N/2$ and the z -projection $m_z = -s, -s + 1, \dots, s - 1, s$. As can be seen from Eq. (6.10) the ground state, $m_z = -N/2$, is the first one to become unstable for any N at a critical coupling $\lambda_c = 1/\sqrt{N}$. This change in the stability of the ground state potential is just the manifestation of the superradiant phase transition that we have discussed before in the approximately resonant case.

Above the transition point we can obtain the tunnel-splitting of the lowest resonator states by approximating the full potential $V_{N/2,-N/2}^{\text{DM}}(X)$ by a quartic double-well potential with the correct barrier height $V_{N/2,-N/2}(0)^{\text{DM}} - V_{N/2,-N/2}(X_{\text{min}})^{\text{DM}}$ and

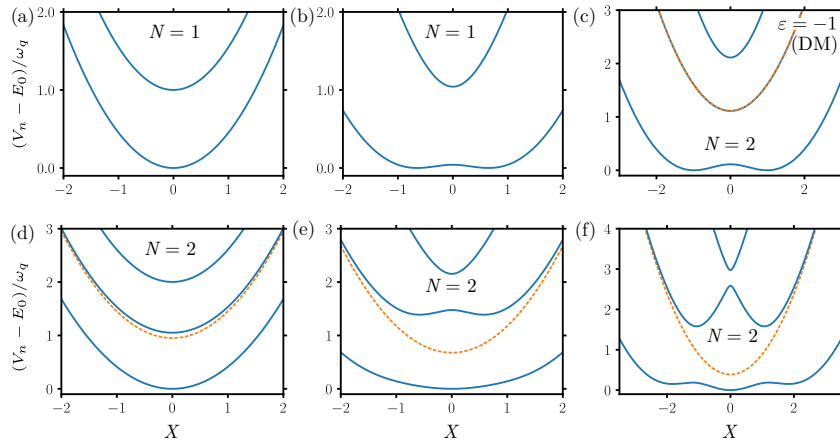


Figure 6.2: BO potentials for one and two coupled qubits. (a) and (b) $N = 1$, the Rabi model. In (a) $\lambda^2 = 0.1$ is below the critical coupling and (b) $\lambda^2 = 1.5$ above it. (c) Dicke model, i.e. $\varepsilon = -1$, for $N = 2$ and $\lambda^2 = 0.8$ above the transition point. The potentials are qualitatively identical to the Rabi model BO potentials. (d-f) $\varepsilon = 0$, i.e. non-interacting qubits for $N = 2$ and (d) $\lambda^2 = 0.1$, (e) $\lambda^2 = 0.8$ and (f) $\lambda^2 = 2.1$. In (c-e) the orange dashed line denotes the singlet state and blue solid lines are for the triplet states. We have plotted the potentials with respect to the minimum of the ground state potential, i.e. $E_0 = \min\{V_0(X)|X\}$.

location of the minima X_{\min} . We obtain [125]

$$\Delta\tilde{\epsilon}_{\lambda>\lambda_c} \approx \frac{8}{\sqrt{\pi}} A e^{-S_0}, \quad (6.11)$$

with a prefactor $A = \sqrt[4]{(\lambda^2 - \lambda_c^2)^5 / [\mu(\lambda^2 + \lambda_c^2)]} / (\lambda_c^2 \lambda)$ and exponent $S_0 = 2\sqrt{\mu(\lambda^2 - \lambda_c^2)^3(\lambda^2 + \lambda_c^2)} / (3\lambda_c^4 \lambda^2)$. For couplings far above the transition point the tunnelling is suppressed by $\Delta\tilde{\epsilon} \sim e^{-2\sqrt{\mu}(N\lambda)^2/3}$. At the critical coupling when the potential is almost purely quartic the energy splitting is given by [126]

$$\Delta\tilde{\epsilon}_{\lambda=\lambda_c} = c \sqrt[3]{\frac{\lambda^2}{\mu^2}}, \quad (6.12)$$

with a prefactor $c \approx 1.1$. Thus, at the transition point the density of states (DOS) $\tilde{\rho}_{\lambda=\lambda_c} = \Delta\tilde{\epsilon}_{\lambda=\lambda_c}^{-1} \sim \sqrt[3]{N\mu^2}$ which diverges in the classical limit $\mu \rightarrow \infty$. Compared to DOS of the bare harmonic potential of the oscillator $\tilde{\rho}_{\lambda=0} = \sqrt{\mu}$, the scaling is only weakly enhanced.

6.2.2 Non-interacting qubits

We move now to non-interacting or only weakly interacting qubits $\varepsilon \simeq 0$. In [Fig. 6.2\(d-f\)](#) we plot the potential curves for this case for three different coupling strengths, again for $N = 2$ qubits. There is a qualitative difference in that the ground state potential remains stable at $X = 0$, while developing additional minima at $X \approx 2$ for $\lambda \gtrsim 1$. More interestingly for us, the potential corresponding to the first qubit excited state develops a double-well structure already at an intermediate interaction strength.

It is not possible to obtain an analytic expression for the effective potentials in the non-interacting case, however, we can calculate analytically the transition point for the first excited state potential using fourth order perturbation theory. At $X = 0$ we can diagonalize \tilde{H}_q exactly for two qubits, since the triplet state $|s = 1, m_z = 0\rangle \equiv |T\rangle$ is decoupled from the other states $|s = 1, m_z = \pm 1\rangle \equiv |\pm 1\rangle$. The eigenenergies and states are given by

$$\tilde{E}_T^{(0)} = \bar{\varepsilon}\lambda^2, \quad |\chi_T\rangle = |T\rangle, \quad (6.13)$$

and

$$\begin{aligned} \tilde{E}_{\pm}^{(0)} &= \frac{1}{2} \left(\bar{\varepsilon}\lambda^2 \pm \sqrt{4 + \bar{\varepsilon}^2\lambda^4} \right), \\ |\chi_{\pm}\rangle &= N_{\pm}^{-1} \left[\left(2\bar{\varepsilon}^{-1}\lambda^{-2} \pm \sqrt{1 + 4\bar{\varepsilon}^{-2}\lambda^{-4}} \right) |1\rangle + |-1\rangle \right], \end{aligned} \quad (6.14)$$

with the normalization constant $N_{\pm} = \sqrt{1 + (\sqrt{1 + 4\bar{\varepsilon}^{-2}\lambda^{-4}} \pm 2\bar{\varepsilon}^{-1}\lambda^{-2})^2}$ and we have introduced the abbreviation $\bar{\varepsilon} = 1 + \varepsilon$. The singlet state $|S\rangle \equiv |s = 0, m_z = 0\rangle$ is decoupled from the cavity so that its energy is given by $\tilde{E}_S = 0$ regardless of λ . Thus, even at $X = 0$ where the field of the resonator vanishes there is an energy splitting between the singlet and triplet states given by

$$\Delta\tilde{E}_{TS} = (1 + \varepsilon)\lambda^2, \quad (6.15)$$

for any $\varepsilon \neq -1$, i.e. the DM. At first this seems odd, but recalling, e.g., a flux qubit realization of this Hamiltonian, it becomes clear. The interaction Hamiltonian between the qubits and the resonator is given by $H_{\text{int}} \propto (\phi_r + \sum_i \phi_i)^2$, where $\phi_{r/i}$ are the flux variables of the resonator and the qubits, see [Fig. 6.1\(a\)](#). At $X = 0$, i.e. $\phi_r = 0$ there is an energy penalty for states for which $\sum_i \phi_i \sim S_x \neq 0$, see [Sec. 4.3](#), which is the case for the triplet state, however, for the singlet this contribution vanishes.

In order to obtain the instability point of the $|\chi_T\rangle$ state we calculate corrections to the $X = 0$ eigenenergy due to the resonator field term $\sqrt{2}\lambda X S_x$. Up to fourth

order in X we obtain [127]

$$\tilde{E}_T^{(2)} = -2X^2\bar{\varepsilon}\lambda^4, \quad (6.16)$$

$$\tilde{E}_T^{(4)} = 4X^4\bar{\varepsilon}\lambda^6(1 + \bar{\varepsilon}^2\lambda^4), \quad (6.17)$$

so that the effective potential is given by

$$\tilde{V}_T(X) = \bar{\varepsilon}\lambda^2 + \frac{X^2}{2}(1 - 4\bar{\varepsilon}\lambda^4) + 4X^4\bar{\varepsilon}\lambda^6(1 + \bar{\varepsilon}^2\lambda^4). \quad (6.18)$$

From the above equation we see that \tilde{V}_T transitions from a single-well to a double-well potential when the quadratic term in X vanishes, that is at

$$4\bar{\varepsilon}\lambda_c^4 = 1 \leftrightarrow \lambda_c = \frac{1}{\sqrt{2\sqrt{1+\bar{\varepsilon}}}}. \quad (6.19)$$

In Fig. 6.2 we have used $\varepsilon = 0$, such that the transition point is given by $\lambda_c = 1/\sqrt{2}$.

6.2.3 General structure

For increasing number of qubits the potential structure becomes more complicated with various global and local minima, and local maxima depending on λ and ε . In Fig. 6.3(a) and (b) we demonstrate this for $N = 3$ and $\varepsilon = 0.02$. In this situation the adiabatic potential corresponding to the first excited state develops a triple-well structure. However, in contrast to the ground state effective potential of the two qubit system, the minima at $X \neq 0$ can become lower in energy than the original global minimum at the origin as λ increases. This situation is reminiscent of a first order phase transition point in which there is a discontinuous jump of the global minimum of the free-energy, see Fig. 6.3(b). In addition to this the ground and second excited state BO potentials exhibit a double-well transition.

To obtain a better intuition about the possible potential structures let us consider the limit $\lambda \gg 1$. In this case the terms proportional to S_x are dominant compared to the S_z term. As a first approximation neglecting the bare qubit Hamiltonian gives the eigenstates $|\chi_{s,m_x}(X)\rangle \equiv |\chi_{s,m_x}(0)\rangle$ which are specified by the total spin s and its projection m_x along x . The corresponding adiabatic potentials are

$$\tilde{V}_{s,m_x}^{(0)}(X) = \frac{1}{2} \left(X + \sqrt{2}\lambda m_x \right)^2 + \varepsilon\lambda^2 m_x^2. \quad (6.20)$$

They are parabolas centred at m_x with a minimum of $\varepsilon\lambda^2 m_x^2$. The resulting total eigenstates $|\phi_{s,m_x,k}(X)\rangle |\chi_{s,m_x}(0)\rangle$ are the semiclassical analogs of the displaced states of Sec. 4.3. In Fig. 6.3(c) they are plotted as the dotted lines. Analogously

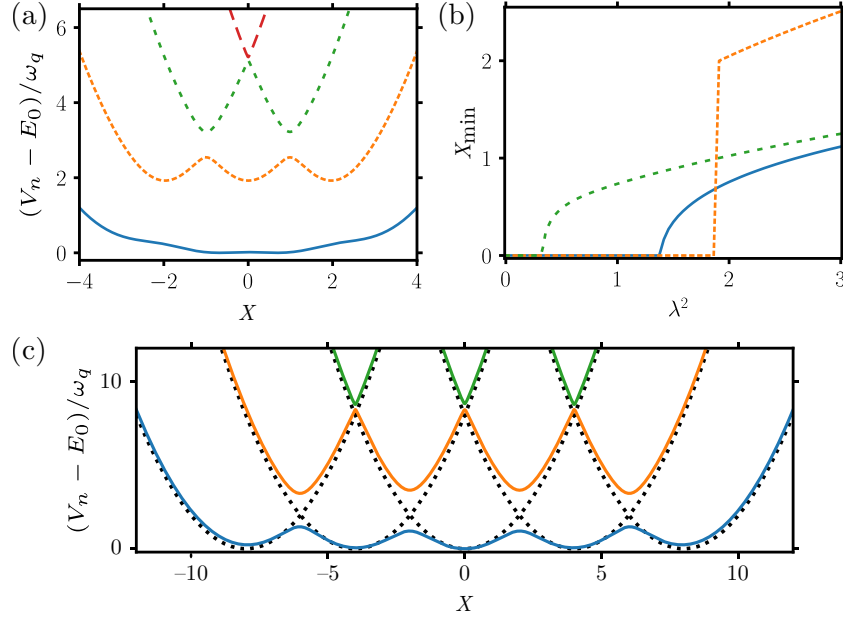


Figure 6.3: Multi-qubit BO potentials. (a) Effective potentials for $N = 3$, $\varepsilon = 0.02$ and $\lambda^2 = 1.86$. The first excited state potential has three degenerate minima at the chosen λ, ε , reminiscent of a first order phase transition. (b) Location of the global minima of the potentials in (a) as a function of λ . The highest potential surface has been omitted since its minimum is at $X = 0$ for all couplings due to symmetry. We have omitted the degenerate minima at $-X_{\min}$. (c) Three lowest potentials for $N = 4$ and $\lambda \gg 1$ for non-interacting qubits. The bare potentials Eq. (6.20) are plotted as the dotted lines. We have only plotted the $s = N/2$ potential curves in all plots for better visibility.

to Sec. 4.3 we can calculate perturbatively the corrections arising from the bare qubit Hamiltonian S_z to these bare potentials. At the minima of each potential $\tilde{V}_{s,m_x}(X_{\min})$, with $X_{\min} = -\sqrt{2}\lambda m_x$ the S_z term induces a second order shift due to coupling to neighbouring states $m_x \pm 1$ given by [127]

$$\begin{aligned} \Delta\tilde{V}_{s,m_x} &= \sum_{m'_x \neq m_x} \frac{|\langle m'_x | S_z | m_x \rangle|^2}{\tilde{V}_{s,m_x}(X_{\min}) - \tilde{V}_{s,m'_x}(X_{\min})} \\ &= -\frac{1}{4\lambda^2} \left(\frac{s_+^2(m_x)}{1 + (2m_x + 1)\varepsilon} + \frac{s_-^2(m_x)}{1 - (2m_x - 1)\varepsilon} \right), \end{aligned} \quad (6.21)$$

where $s_{\pm}(m_x) = \sqrt{s(s+1) - m_x(m_x \pm 1)}$. For weak interactions $\varepsilon \ll 1$ we obtain

$$\Delta\tilde{V}_{s,m_x} \approx \frac{(1 - 3\varepsilon)m_x^2 - (1 - \varepsilon)s(s+1)}{2\lambda^2}, \quad (6.22)$$

and at $\varepsilon = 0$ we reproduce exactly the result of the full quantum calculation of [Sec. 4.3](#). At the points where two neighbouring parabolas meet $X_{\text{deg}} = -(1 + \varepsilon)(2m_x + 1)\lambda/2$ we can exactly diagonalize the 2×2 Hamiltonian describing the states $m_x, m_x + 1$ to obtain the splitting between the resulting potential curves. The effective Hamiltonian for the two states is given by

$$\tilde{H}_{X_{\text{deg}}} = \tilde{V}_{s,m_x}^{(0)}(X_{\text{deg}})I_{2 \times 2} + \frac{s_+(m_x)}{2}\sigma_x, \quad (6.23)$$

where $I_{2 \times 2}$ is the 2×2 identity matrix. The eigenvalues of the effective Hamiltonian are

$$\tilde{E}_{\pm} = \tilde{V}_{s,m_x}^{(0)}(X_{\text{deg}}) \pm \frac{s_+(m_x)}{2}, \quad (6.24)$$

which leads to a splitting $\Delta = s_+(m_x)$. There are also higher order avoided crossings between adiabatic potentials corresponding to states m_x and $m_x \pm n$. In [Fig. 6.3\(c\)](#) the resulting potentials are plotted with solid lines. For a general λ and ε the effective potentials are smooth transformations of the stacked parabolas $\tilde{V}_{s,m_z} = X^2/2 + m_z$ in the uncoupled case, all the way to the degenerate parabolas of [Eq. \(6.20\)](#).

6.3 Probing the spectrum

In traditional circuit QED systems both the qubits and the resonator are in the GHz regime and they can be efficiently probed using electronic readout techniques. However, in the rf-regime this is no longer feasible with usual methods. Thus, all the information about the oscillator mode has to be deduced from measurements on the qubits.

As a first example we consider the single-qubit excitation spectrum $S(\omega)$ given by [\[112\]](#)

$$S(\omega) = \frac{\Gamma}{2} \Re \int_0^{\infty} d\tau \langle \sigma_x(\tau) \sigma_x(0) \rangle e^{i\omega\tau}, \quad (6.25)$$

where the expectation value is taken with respect to the equilibrium state of the system. Due to the assumption of identical qubits, any of them can be chosen to be excited, all giving the same result. Above we have introduced a characteristic decay rate Γ of the correlation function. In the parameter regime we are considering the qubits are not so strongly affected by the resonator, such that Γ will be close to the bare decay rate of the qubit. In the numerical calculations that follow we have assumed rather large values $\Gamma \sim \omega_r$ for the decay rate, compared to the achievable rates in state-of-the-art flux qubits [\[33\]](#).

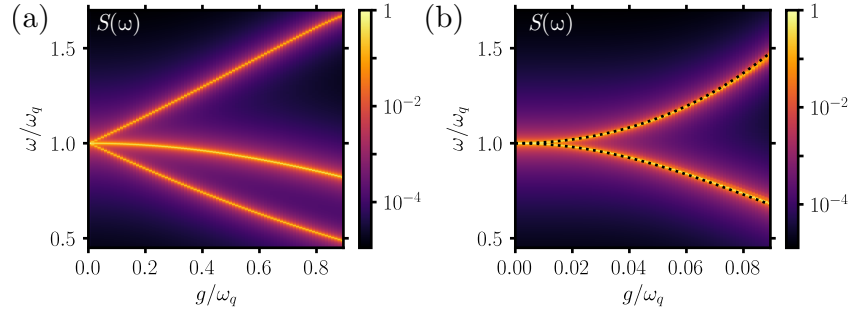


Figure 6.4: Single qubit excitation spectrum $S(\omega)$ for $N = 2$ qubits on resonance (a) and for $\mu = 10^4$ (b). The black dotted lines in (b) are the energies of the triplet and singlet state potentials relative to the ground state at $X = 0$. We have used $\varepsilon = 0$ and $\Gamma/\omega_q = 5 \times 10^{-3}$ in both plots.

6.3.1 Strong-coupling condition

Let us assume the qubit-resonator system has been initialized close to the ground-state $|\text{GS}\rangle$ of the system, which can be achieved e.g. by cooling [128]. In this situation we can express $S(\omega)$ as

$$S(\omega) = \frac{1}{4} \sum_f \frac{\Gamma^2 |\langle f | \sigma_x | \text{GS} \rangle|^2}{(\omega - \omega_f)^2 + \Gamma^2/4}, \quad (6.26)$$

where the sum goes over the final states $\langle f |$ separated from the ground state by ω_f . In Fig. 6.4 we plot the excitation spectrum for a standard resonant cavity QED system, (a), and for a low frequency resonator, (b). We have taken $N = 2$ for both plots, and plot them against g rather than λ as is common practice.

In the resonant case the vacuum Rabi splitting $\Omega_R = \sqrt{2}g$ is visible in the plot, resulting from the hybridisation of the resonator and the triplet state $|T\rangle$ of the qubits. The strong coupling regime for a resonant cavity QED system is then reached when the splitting exceeds the linewidth $\Omega_R > \Gamma$. The resonance in between the Rabi-split lines is the antisymmetric singlet state $|S\rangle$ of the qubits, which does not couple to the cavity. Its frequency with respect to the ground state does however change, visible as the bending down of the line for larger interaction strengths.

In the rf-domain, $\mu = 10^4$, the frequency of the resonator cannot be seen on the scale of the plot. The interaction between the mode and the qubits nevertheless has a strong influence on the spectrum. The coupling induced splitting between the singlet and tripled states, Eq. (6.15), can be seen, and a strong coupling condition

for the radio-frequency regime can be formulated as

$$g > \sqrt{\frac{\Gamma\omega_r}{1+\varepsilon}}, \quad (6.27)$$

i.e. when ΔE_{TS} exceeds the linewidth.

The excitation frequencies obtained from the BO potentials at $X = 0$ are plotted in Fig. 6.4(b) as the dashed lines. The agreement with the main peaks of the excitation spectrum demonstrates that at low temperatures the single qubit spectrum probes the BO potentials at $X = 0$. This can be understood considering the wave function of Eq. (6.6). For moderate couplings the qubit states are only weakly dependent on X such that they can be approximated by $\chi_n(X = 0)$ where the ground state wave function is concentrated. With these approximations the spectrum is given by

$$S(\omega) \simeq \frac{|\langle \chi_1(0) | \sigma_x | \chi_0(0) \rangle|^2}{4} \sum_k \frac{\Gamma^2 |\langle \phi_{1,k} | \phi_{0,0} \rangle|^2}{(\omega - \omega_{k0})^2 + \Gamma^2/4}, \quad (6.28)$$

where $\omega_{k0} = \epsilon_{1,k} - \epsilon_{0,0}$. From the above formula we see that states with big overlap with the resonator ground state wave function, extending $\sim 1/\sqrt{\mu}$ around $X = 0$ in the harmonic approximation, are most relevant for the spectrum. Due to this fact there is no special feature at the transition point $\lambda_c = 1/\sqrt{2}$, which corresponds to $g/\omega_q \simeq 0.07$ in Fig. 6.4(b).

6.3.2 Detecting the change in the stability of the excited state

In order to pin point signatures of the symmetry breaking transition, we show in Fig. 6.5(a) and (b) zoom of the triplet resonance and cuts of $S(\omega)$ for various coupling strengths below and above the transition point λ_c , respectively. For couplings below the critical value the height of the resonance peak decreases slightly, which is mostly attributable to a decrease in the matrix element $\langle \chi_1(0) | \sigma_x | \chi_0(0) \rangle$. At the transition point, however, there is a rapid decrease in the height of the spectral line. Moreover, for $\lambda > \lambda_c$ the lines get significantly broader and start to exhibit additional structure. These features can be, again, understood based on the resonator states. At the critical coupling the BO potential corresponding to the triplet state becomes quartic, as we have shown, such that the lowest resonator wave function $\phi_{1,0}$ corresponding to it broadens significantly, reducing the overlap to the ground state wave function $\phi_{0,0}$. For couplings above the transition point $V_1(X)$ is a double-well potential, such that the amplitudes of the energetically lowest wave functions at $X = 0$ are further reduced. Thus, the main contribution to the spectral line comes from eigenstates close to energy $V_1(X = 0)$, whose wave

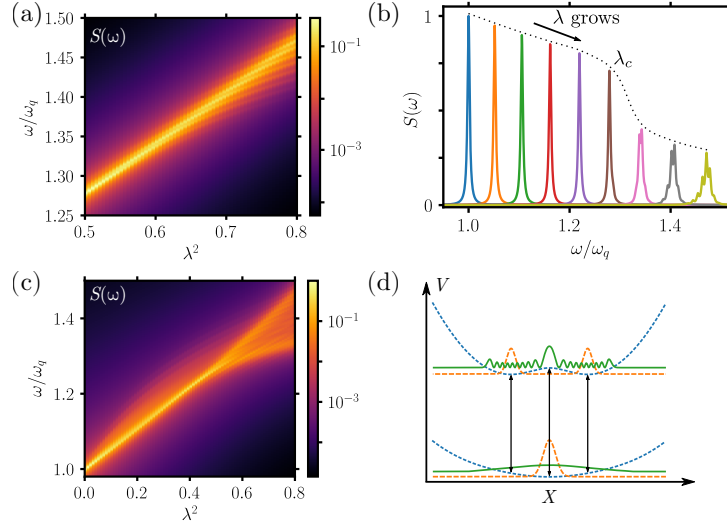


Figure 6.5: Probing the symmetry breaking transition. (a) Zoom of the triplet resonance of $S(\omega)$ from Fig. 6.4 (b) for $\lambda > \lambda_c$. Note, here we plot the spectrum against $\lambda^2 \propto g^2$ and the resonance line is linear in λ^2 . (b) Cuts of $S(\omega)$ for different $\lambda^2 \in [0.1, 0.8]$ in steps of 0.1. The black dotted line is a guide to the eye. (c) Spectrum for a finite temperature $k_B T/\omega_q = 0.1$. Only the triplet resonance is shown. (d) A finite temperature enables transitions between the ground state potential and the lowest states in the double-well of the excited states, upper dashed orange line, due to the wider spread of the thermal state, lower green solid line. We have used $\mu = 10^4$, $\varepsilon = 0$ and $\Gamma/\omega_q = 5 \times 10^3$ for all plots.

functions are more concentrated around $X = 0$. Other smaller amplitude peaks are generated by states living in the two wells of $V_1(X)$ which are resolved only for sufficiently small Γ .

A clearer signature of the change in the stability of the triplet state is obtained from the spectrum at finite temperature T , which we show in Fig. 6.5(c). To calculate the thermal spectrum, Eq. (6.28) has to be averaged over a thermal distribution of initial states $\phi_{0,k}$. The excited oscillator states of the ground state allow transitions to states farther away from $X = 0$, such that the spectrum probes the triplet potential on a broader range of X . We consider a temperature of $k_B T/\omega_q = 0.1$, for which the qubits are still in the ground state with a high probability, but several resonator states $\sim k_B T/\omega_r = 10$ are occupied. In this situation the triplet-state resonance splits into two for $\lambda > \lambda_c$. They can be identified with the energy separations between the ground and triplet potentials at $X = 0$ and $X = X_{\min}$ of the triplet potential. This is illustrated in Fig. 6.5(d). This measurement does not require any cooling of the rf-mode offering a simple

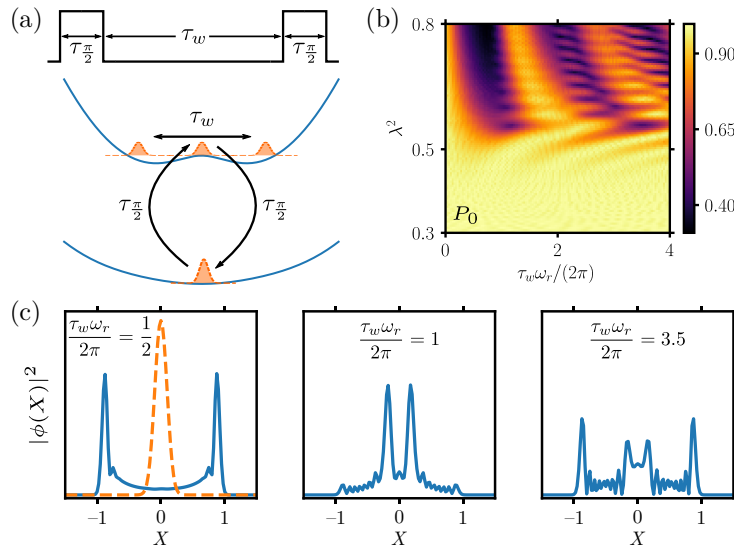


Figure 6.6: Ramsey protocol. (a) Sketch of the protocol for detecting the wave packet dynamics. The resonator state is prepared in a superposition between two effective potentials and is let to evolve freely for a variable time τ_w . After a $\pi/2$ -pulse the return probability $P_0(\tau_w)$ to the qubit ground state is measured. (b) The return probability P_0 as a function of the coupling strength λ^2 and the waiting time τ_w . (c) The resonator wave function conditioned on the qubit excited state $|\chi_1(0)\rangle$ during the free evolution and $\lambda^2 = 0.8$. The initial wave packet, orange dashed line in the first panel, is a superposition of many eigenstates $\phi_{1,k}$ of $V_1(X)$, and, thus, starts to spread. After reaching the classical turning points it returns back. We have used $\varepsilon = 0$ for all plots and have not included qubit decoherence.

path for observing signatures of the change in the triplet-potential structure.

6.4 Wave-packet dynamics

Another way to probe the excited state transition is through dynamics. The basic idea is to perform a Ramsey-type measurement [129] illustrated in Fig. 6.6(a). In the beginning of the protocol the system is prepared in the absolute ground state. Then a single qubit is driven creating an equal superposition between the qubit excited and ground states, while keeping the resonator state fixed. After creating the superposition the resonator state is let to evolve in the superposition potential. After some waiting time the system is driven back, and the overlap between the two wave packets that have evolved in the two potentials can be determined by measuring the qubit polarization.

We apply this protocol to an $N = 2$ qubit system as in the previous section. The system is prepared in the ground state $|\Psi(t = 0)\rangle \simeq |\phi_{0,0}\rangle |\chi_0(0)\rangle$ e.g. by cooling. A microwave field of frequency ω_d is used to drive the system to a 50-50 superposition between the qubit ground state and the triplet state. During this time the system evolves according to the Hamiltonian $H = H_{\text{EDM}} + H_{\Omega}(t)$, with

$$H_{\Omega}(t) = \Omega \cos(\omega_d t + \theta) \sigma_x, \quad (6.29)$$

and σ_x is a single qubit operator for an arbitrary qubit. For the first pulse we set the phase $\theta = 0$ and optimize the pulse time $\tau_{\frac{\pi}{2}} \sim \Omega^{-1}$ for every λ . The driving can be done in a time much smaller than the characteristic time of the oscillator, such that its state does not evolve during the pulse time. In the second step we let the system evolve under the free Hamiltonian H_{EDM} for a waiting time τ_w . The resonator wave packet propagates in two different potentials $V_0(X)$ and $V_1(X)$ during this time. Finally, a second $\pi/2$ -pulse is applied this time with an optimized phase θ to counteract any trivial phase differences accumulated between the states. For $\lambda = 0$ the qubits would be driven perfectly back into the ground state. For a general λ the return probability $P_0(\tau_w) = \text{Tr} [\rho(t_f) |\chi_0(0)\rangle \langle \chi_0(0)|]$, with $\rho(t_f)$ the density operator at the final time $t_f = 2\tau_{\frac{\pi}{2}} + \tau_w$, can be used to probe the dynamics of the resonator wave packet during the free evolution. The ground state probability can be measured e.g. by dispersively coupling the qubits to another GHz resonator [25].

The return probability $P_0(\tau_w)$ is plotted in Fig. 6.6(b) for varying τ_w and λ . We see a clear difference in P_0 above and below the critical coupling $\lambda_c = 1/\sqrt{2}$. For couplings smaller than λ_c the ground and triplet state potentials are both approximately harmonic, such that the resonator wave packet remains localized around the origin in both potentials, resulting in a near perfect return to the initial state. Above the transition point the wave packet starts to oscillate in the double-well potential of the triplet state, resulting in oscillations in the return probability. We have confirmed that the oscillation frequency matches the dynamics of a wave packet initialized in the centre of the triplet state BO potential. Thus, the Ramsey-sequence probes the overlap between the time-evolved wave packet in the excited state potential and the Gaussian ground state. In Fig. 6.6(c) we plot a few snapshots of the resonator state $\phi(X)$ conditioned on the qubit excited state $|\chi_1(0)\rangle$. For $\tau_w = 0$ the state is the Gaussian ground state wave packet centred at $X = 0$. After waiting time of $1/(2\nu_r)$ almost all of the wave packet has left the central region and arrived at the classical turning points. For a longer waiting time the wave packet returns, but due to the non-linearity of the triplet potential a perfect revival is not possible. In the simulations we have not considered qubit decoherence, thus in order to observe these effects the qubit coherence time T_2 has to be longer than $\tau_w \sim \omega_r^{-1}$. This is not a stringent requirement, even for $\omega_r/(2\pi) \approx 10$ MHz it can be fulfilled with realistic coherence times of $T_2 \sim 1 - 100 \mu\text{s}$ [33].

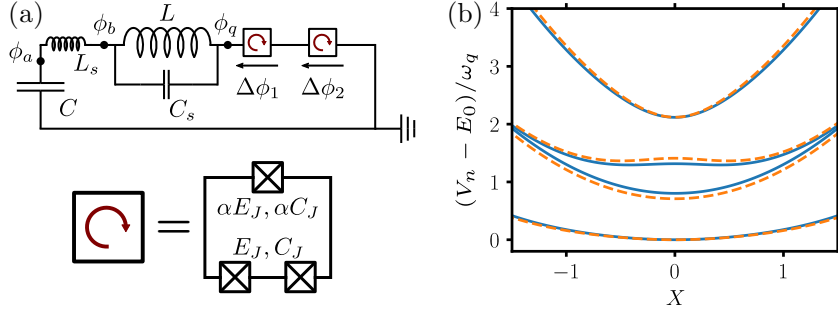


Figure 6.7: (a) More realistic circuit, including the self-reactances L_s and C_s of C and L , respectively. Using this circuit we can estimate the effect of a higher mode $\omega_{ex} \sim 1/\sqrt{L_s C_s}$ on the physics. The qubits are taken to be three junction flux qubits. (b) The BO potentials of the LF mode resulting from the two-mode circuit of (a), blue solid lines, are compared to the ideal potential curves of the corresponding EDM, orange dashed lines. The parameters used for the two-mode circuit are given in Tab. 6.1. Note that we have adjusted the capacitance C_J in order to maintain the same qubit frequency for the single and two-mode circuits ($C_J \approx 3.5$ fF for the single-mode circuit).

6.5 Circuit QED implementation

As we mentioned in the beginning of the chapter the physics described above could be probed with flux qubits coupled inductively to an LC -resonator. In traditional circuit QED systems with $\omega_r \sim \omega_q$ the higher resonances of the LC -circuit can be made much higher than ω_r/q such that even in the USC regime $\omega_{ex} \gg \omega_r, \omega_q, g$ [41]. In the low frequency oscillator parameter regime this is not, however, clear and we need to analyse the validity of the single mode approximation more carefully.

In Fig. 6.7(a) we show a more realistic model for a system with two flux qubits coupled to an LC -oscillator. We take into account the self-capacitance C_s of the inductor and the self-inductance of L_s of the capacitor [130]. This gives rise to a second mode $\omega_{ex} \sim 1/\sqrt{L_s C_s}$ with a frequency much above the resonator. For concreteness we take the flux qubits to be three-junction qubits [67, 131–133].

We choose the flux variables as indicated in Fig. 6.7. The Lagrangian of the two-mode circuit then becomes

$$\mathcal{L} = \frac{C\dot{\phi}_a^2}{2} + \frac{C_s(\dot{\phi}_b - \sum_k \Delta\dot{\phi}_k)^2}{2} - \frac{(\phi_a - \phi_b)^2}{2L_s} - \frac{(\phi_b - \sum_k \Delta\phi_k)^2}{2L} + \sum_k \mathcal{L}_{q_k}, \quad (6.30)$$

where the qubit Lagrangian is given by

$$\mathcal{L}_{q_k} = \frac{C_q \Delta \dot{\phi}_k^2}{2} + \frac{C_- \dot{\phi}_{-,k}^2}{2} + E_J \left[\alpha \cos \left(\frac{\Delta \phi_k + \Phi_e}{\Phi_0} \right) + 2 \cos \left(\frac{\Delta \phi_k}{2\Phi_0} \right) \cos \left(\frac{\phi_{-,k}}{2\Phi_0} \right) \right], \quad (6.31)$$

and the additional qubit variable $\phi_{-,k}$, not coupled to the LC -circuit, corresponds to the generalized flux between the two junction in the lower arm of the qubit. The qubits are biased with an external magnetic flux Φ_e , and the effective capacitances are given by $C_q = C_J(\alpha + 1/2)$ and $C_- = C_J/2$. After introducing the conjugate charges $q_{a/b} = \partial_{\phi_{a/b}} \mathcal{L}$, $q_k = \partial_{\Delta \phi_k} \mathcal{L}$ and $q_{-,k} = \partial_{\phi_{-,k}} \mathcal{L}$ the Hamiltonian becomes

$$H = H_{LC} + H_{\text{int}} + H_q, \quad (6.32)$$

where $H_q = \sum_k [H_{q_k} + \sum_l \Delta \phi_k \Delta \phi_l / (2L)]$ and

$$H_{q_k} = \frac{q_k^2}{2C_q} + \frac{q_{-,k}^2}{2C_-} - E_J \left[\alpha \cos \left(\frac{\Delta \phi_k + \Phi_e}{\Phi_0} \right) + 2 \cos \left(\frac{\Delta \phi_k}{2\Phi_0} \right) \cos \left(\frac{\phi_{-,k}}{2\Phi_0} \right) \right] \quad (6.33)$$

is the single flux-qubit Hamiltonian. The LC -circuit is described by the two-mode Hamiltonian

$$H_{LC} = \frac{q_a^2}{2C} + \frac{q_b^2}{2C_b} + \frac{(\phi_a - \phi_b)^2}{2L_s} + \frac{\phi_b^2}{2L}, \quad (6.34)$$

and

$$H_{\text{int}} = \frac{q_a q_b}{C_q} + \frac{\phi_q \phi_b}{L} \quad (6.35)$$

is the qubit-resonator interaction Hamiltonian. In Eq. (6.34) we have introduced the effective capacitance $C_b = C_s C_q / (C_s + 2C_q)$ of the b -mode.

As a next step we diagonalize the LC Hamiltonian to $H_{LC} = \sum_{\eta=\pm} \omega_\eta c_\eta^\dagger c_\eta$ with the normal mode frequencies

$$\omega_\pm^2 = \frac{1}{2} \left(\omega_a^2 + \omega_b^2 \pm \sqrt{(\omega_a^2 - \omega_b^2)^2 + 4g_{ab}^2 \omega_a \omega_b} \right), \quad (6.36)$$

where the bare frequencies are given by $\omega_a = 1/\sqrt{L_s C}$, $\omega_b = 1/\sqrt{L_b C_b}$ and $g_{ab} = \sqrt{Z_b/Z_a} \omega_a$ is the coupling between them. The impedances of the bare modes are $Z_{a/b}$ and $L_b = L_s L / (L_s + L)$ is the effective inductance of mode b . In terms of the normal modes the coupling Hamiltonian H_{int} becomes

$$H_{\text{int}} = \sum_{k,\eta=\pm} i \frac{g_{q,\eta}}{2} (c_\eta^\dagger - c_\eta) n_k + \frac{g_{\phi,\eta}}{2} (c_\eta^\dagger + c_\eta) \varphi_k, \quad (6.37)$$

where we have used the dimensionless qubit variables $n_k = q_k/(2e)$ and $\varphi_k = \Delta\phi_k/\Phi_0$. The couplings are given by

$$g_{q,+} = 2\sqrt{\frac{\pi Z_b C_b}{R_Q C_q}} \sqrt{\frac{\omega_+}{\omega_b}} \sin(\xi)\omega_b, \quad (6.38)$$

$$g_{q,-} = 2\sqrt{\frac{\pi Z_b C_b}{R_Q C_q}} \sqrt{\frac{\omega_-}{\omega_b}} \cos(\xi)\omega_b, \quad (6.39)$$

$$g_{\phi,+} = \sqrt{\frac{R_Q}{\pi Z_b}} \sqrt{\frac{\omega_b}{\omega_+}} \sin(\xi)\omega_b, \quad (6.40)$$

$$g_{\phi,-} = \sqrt{\frac{R_Q}{\pi Z_b}} \sqrt{\frac{\omega_b}{\omega_-}} \cos(\xi)\omega_b, \quad (6.41)$$

where the mixing angle ξ is defined through

$$\tan(2\xi) = -\frac{2g_{ab}\sqrt{\omega_a\omega_b}}{\omega_a^2 - \omega_b^2}. \quad (6.42)$$

In the limit $L_s \ll L$, $C_s \ll C$ the normal mode frequencies reduce to $\omega_- \approx 1/\sqrt{LC} = \omega_r$ and $\omega_+ \approx 1/\sqrt{L_s C_b}$ and the couplings can be simplified to

$$\frac{g_{\phi,-}}{\omega_-} = \sqrt{\frac{R_Q}{\pi Z}}, \quad \frac{g_{q,-}}{\omega_-} = 2\sqrt{\frac{\pi Z C_b}{R_Q C_q}}, \quad (6.43)$$

$$\frac{g_{\phi,+}}{\omega_+} = \sqrt{\frac{R_Q L_s}{\pi Z_b L}}, \quad \frac{g_{q,+}}{\omega_+} = 2\sqrt{\frac{\pi Z_b C_b}{R_Q C_q}}, \quad (6.44)$$

where $Z = \sqrt{L/C}$ is the impedance of the low frequency mode. From the above definitions we see that for a typical $Z \approx 50\Omega$ resonator the charge coupling is negligible. Moreover, for the high-frequency mode the dimensionless inductive coupling is reduced by a factor $L_s/L \ll 1$, assuming $Z_b \sim Z$.

We continue by introducing the rescaled quadratures, Eq. (6.3), and arrive at the renormalized Hamiltonian $\tilde{H} = H/\omega_q$

$$\tilde{H} = \frac{P^2}{2\mu} + \frac{X^2}{2} + \tilde{H}_h(X, P), \quad (6.45)$$

with ω_q the characteristic qubit frequency and effective mass $\mu = (\omega_q/\omega_-)^2$. Note, that the Hamiltonian for the high-frequency physics now also includes the high-frequency mode c_+

$$H_h(X, P) = \omega_+ c_+^\dagger c_+ + H_{\text{int}}(X, P) + H_q, \quad (6.46)$$

Qubit	Resonator
$C_J = 2.21$ fF	$C = 79.58$ pF
$E_J/h = 336.8$ GHz	$L = 127.3$ nH
$\alpha = 0.74$	$C_s = 1.06$ fF
	$L_s = 1.27$ nH

Table 6.1: The set of circuit parameters for the qubits and the LC -resonator, which are used for the numerical simulations shown in Fig. 6.7(b).

and depends also on the momentum P of the low-frequency mode due to the presence of the charge coupling.

In Tab. 6.1 we give the set of parameters that we consider. The parameters for the LC -circuit are comparable to what can be achieved in state-of-the-art experiments [134–137]. The high-frequency Hamiltonian \tilde{H}_h is then diagonalized, without using a TLA for the qubits, and BO potentials for the low-frequency mode are obtained. We compare the effective potentials from the full two-mode circuit to the ideal BO potentials from the corresponding single-mode circuit, by neglecting the self-capacitance and self-inductance of the resonator inductor and capacitor, respectively. The parameters of Tab. 6.1 give $\omega_q/(2\pi) \approx 8$ GHz, $\omega_-(2\pi) = 50$ MHz, such that the effective mass is $\mu \approx 2.5 \times 10^4$. The coupling constants are given by $g_{\phi,-}/\omega_- \approx 7.15$ and $g_{q,-} \approx 0.06$, which would translates to $\lambda \approx 0.84$ in a single mode setup. For the high-frequency mode we obtain $\omega_+/(2\pi) \approx 160$ GHz, safely above the qubit, and the couplings are $g_{q,+}/\omega_+ \approx 0.37$ and $g_{\phi,+}/\omega_+ \approx 0.01$.

In Fig. 6.7(b) we show the comparison of the BO potentials from the single- and two-mode circuits. The potentials are qualitatively similar, with only small shifts near $X = 0$. The appearance of the momentum P in $\tilde{H}_h(X, P)$ in principle changes the effective potential picture. However, the charge coupling $g_{q,-}$ is very small and only contributes a second order term $\sim (g_{q,-}/\omega_-)^2 P^2$, resulting in a small renormalization of the effective mass, which for the current set of parameters is negligible. Thus, we conclude that the presence of other resonances does not change the physics as long as they are above the qubit frequency.

Chapter 7

Generating multi-qubit entanglement from the subradiant vacuum

In the previous chapters we have concentrated on the basic description of ultra-strongly coupled light-matter systems. In this chapter we explore how the strong coupling can be used as a resource.

In [Chap. 5](#) we have shown that in a system of N non-interacting qubits coupled to a common oscillator mode the qubits become highly entangled in the USC regime. More specifically the ground state of the system, for N even, is given by $|\text{GS}\rangle \simeq |0\rangle |N/2, 0\rangle$, where $|n\rangle$ is a Fock state of n photons and $|s, m_x\rangle$ is an angular momentum eigenstate of total angular momentum s and x-projection m_x . The Dicke state $|N/2, 0\rangle$ is highly entangled, but since the system is strongly interacting this entanglement among the qubits is not useful. We present a protocol to prepare the system in the entangled ground state $|\text{GS}\rangle$ starting from the uncoupled standard vacuum state $|n = 0\rangle |s = N/2, m_z = -N/2\rangle$ and then bring the entangled qubit state back into the non-interacting regime. As a possible realization of the presented protocol we envision flux qubits coupled to a lumped element *LC*-resonator, see e.g. [Fig. 4.3](#).

7.1 General description of the protocol

As we have shown in [Chap. 5](#), the system of non-interacting qubits coupled to a common resonator mode is described by the Hamiltonian ($\hbar = 1$)

$$H_{\text{EDM}} = \omega_r a^\dagger a + \omega_q S_z + g(a^\dagger + a)S_x + \frac{g^2}{\omega_r} S_x^2. \quad (7.1)$$

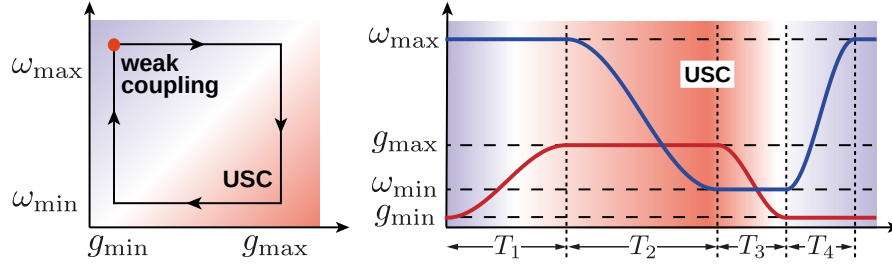


Figure 7.1: The general entanglement extraction protocol. The system parameters $\omega_q(t)$ and $g(t)$ are varied adiabatically and diabatically to first prepare a given state, determined by the initial state, and then extract it to a non-interacting regime, respectively.

We assume that the qubit frequency ω_q and the light-matter coupling strength g can be tuned by changing some underlying system parameters. The parameters are initialized in the beginning of the protocol to $\omega_q(t=0) = \omega_{\max} \gg \omega_r$, $g(t=0) = g_{\min} \ll \omega_r$. In this regime the eigenstates of the system are to a good approximation given by the uncoupled eigenstates $|n\rangle |s, m_z\rangle$. The system is initialized to a chosen eigenstate or any superposition or incoherent mixture, such as a thermal state see [sub-Sec. 7.3.1](#), of the eigenstates, ρ_i . By *adiabatically* adjusting $\omega_q(t)$ and $g(t)$ the system is tuned into the USC regime in two steps: First the coupling strength is tuned from the initial value in time T_1 to $g(T_1) = g_{\max} \gg \omega_r$, while $\omega_q(t)$ is kept constant. Second the qubit frequency is tuned in time T_2 from the initial value to $\omega_q(T_1 + T_2) = \omega_{\min} \sim \omega_r$ and the coupling strength is kept constant during this time. In a perfectly adiabatic situation the state of the system will evolve adiabatically into a final state ρ_f completely determined by the initial state that was chosen, and the values ω_{\min}, g_{\max} . At this point the steps taken are executed again in a reverse manner, but in a diabatic way: First the coupling is ramped quickly back to its initial value in time T_3 , $g(t = T_1 + T_2 + T_3) = g_{\min}$, and then the qubit frequency is switched in time T_4 back, $\omega_q(T_1 + T_2 + T_3 + T_4) = \omega_{\max}$. Since these changes in the system parameters are done in a diabatic manner, the system does not have time to respond to these changes, and the state of the system stays ideally unchanged during the last two steps. Thus, at the end of the protocol the system is in the state ρ_f that was prepared during the first half of the protocol, but the system is brought back into the non-interacting regime. Since the qubits do not anymore interact strongly with the resonator they can be manipulated separately and the entanglement can be used, e.g., in a quantum information protocol. The basic idea is illustrated in [Fig. 7.1](#).

Due to the large qubit frequency $\omega_{\max} \gg \omega_r$ the resonator and the qubits are highly off-resonant in the beginning of the protocol. Thus, the ramp-up of the cou-

pling needs to be slow only compared to this fast time scale set by the initial qubit frequency. In the second step the coupling is already large, such that when the qubit and resonator frequencies become comparable the non-adiabatic state transitions are reduced by the exponentially suppressed qubit frequency $\omega_{\min} e^{-g_{\max}^2/(2\omega_r)}$, see Sec. 5.1. Thus, ramping the qubit frequency has to be slow only compared to the fast time scale g_{\max}^{-1} . In the same spirit the diabatic steps, switching of the coupling strength and the qubit frequency, have to be fast only compared to the slow time scales $\omega_r^{-1}, \omega_{\min}^{-1}$ and g_{\min}^{-1} . This is very important so that the ramping times are experimentally feasible and consistent with the two-level-approximation that we have used for the qubits.

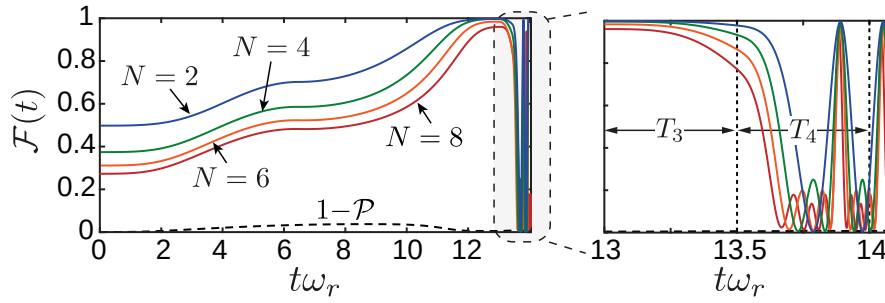


Figure 7.2: Fidelity of the state of the system to the entangled qubit state $|N/2, 0\rangle$ during the protocol. The oscillations after the end of the protocol are trivial and can be undone by single qubit rotations. The parameters we have used are $\omega_{\max}/\omega_r = 20$, $\omega_{\min}/\omega_r = 0.5$, $g_{\max}/\omega_r = 4.5$, $g_{\min}/\omega_r = 0.1$ and the time intervals are $T_1 = T_2 = 6.5\omega_r^{-1}$ and $T_3 = T_4 = 0.5\omega_r^{-1}$, which are all same for the different qubit numbers. The impurity $1 - \mathcal{P}$ is plotted only for $N = 4$.

7.2 Extracting the ground state entanglement

In order to extract the entanglement in the ground state of the system we choose the uncoupled ground state $|0\rangle |N/2, m_z = -N/2\rangle$ as the initial state. By virtue of the adiabatic theorem [138] the system will stay in the instantaneous ground state during the adiabatic steps T_1 and T_2 of the protocol. Thus, after these two steps the system has been prepared in the qubit-entangled USC ground state $|\text{GS}\rangle$. After ramping down the coupling and ramping up the qubit frequency the qubits are in the entangled USC ground state, but do not anymore strongly interact with the resonator.

We quantify the effectiveness of the protocol by using the fidelity of the prepared qubit state to the ideal state $|s = N/2, m_x = 0\rangle$ defined through $\mathcal{F}(t) =$

$\text{Tr}[\rho(t) |N/2, 0\rangle \langle N/2, 0|]$, where $\rho(t)$ is the density operator of the system. The total duration of the protocol is given by $T_f = \sum_{i=1}^4 T_i$. As a figure of merit for the whole protocol we use the entanglement extraction fidelity (EEF) $\mathcal{F}_E = \max\{\mathcal{F}(t) | t \geq T_f\}$, i.e. the maximum fidelity after the protocol has been run. In Fig. 7.2 we plot the fidelity $\mathcal{F}(t)$ during the protocol. The protocol is run for four different number of qubits $N = 2, 4, 6, 8$, all of which use the same values for the parameters, see Fig. 7.2 caption. The obtainable EEFs are all near perfect $\mathcal{F}_E \approx 0.95 - 0.99$ without fine-tuning the protocol for different qubit numbers. The oscillations in $\mathcal{F}(t)$ after finishing the protocol are due to trivial phase factors from the evolution of the entangled state under the free qubit Hamiltonian $H_{\text{free}} = \omega_q S_z$, and can be undone by local qubit rotations.

We also plot $1 - \mathcal{P}$ where \mathcal{P} is the purity $\mathcal{P} = \text{Tr}[\rho_q(t)^2]$ of the reduced qubit state $\rho_q(t) = \text{Tr}_r[\rho(t)]$ in Fig. 7.2, black dashed line. The purity of the qubit state at the end of the protocol is essentially one. During the protocol the qubits and the resonator entangle, but when the USC ground state is reached the purity of the qubit state is regained. The purity plot is for the case of $N = 4$ qubits.

As a possible experimental realization of the protocol we consider qubits with a maximal energy gap $\omega_{\text{max}}/(2\pi) \approx 10$ GHz coupled to an LC -resonator of frequency $\omega_r/(2\pi) \approx 500$ MHz. Then the maximal required coupling in the protocol $g_{\text{max}} = 4.5\omega_r \approx 2\pi \times 2.25$ GHz is consistent with experimentally demonstrated values in flux qubits [41, 42]. The required amount of tunability of the qubit frequency and the coupling is demonstrated in Sec. 7.4. The diabatic switching times we have assumed are $T_{3,4} = 0.5\omega_r^{-1} \approx 0.16$ ns. Sinusoidal modulation of flux qubits on these time scales has already been demonstrated [139] and they are within reach of state-of-the-art waveform generators. The duration of the protocol $T_f = 14\omega_r^{-1} \approx 5$ ns is much smaller than coherence times of flux qubits $\sim 1 - 100$ μs [33].

Modifications of this scheme can be used to prepare also other entangled qubit states. For example a singlet state of the qubits characterized by total angular momentum $s = 0$ and zero projection along all axes $S_{x/y/z} |S\rangle = 0$ can be prepared. The biggest difference to the presented scenario is that the s conserving nature of the Hamiltonian has to be broken during the protocol in order for the qubits to evolve out of the maximal spin subspace $s = N/2$ to the singlet subspace $s = 0$. The singlet preparation scheme is inherently robust against disorder in the qubit frequencies. Retaining a coupling $g(T_f) \gtrsim \omega_r$ at the end of the protocol, which can be done since the singlet states are decoupled from the cavity, energetically separates the $s = 0$ subspace from the other total spin subspaces. The reason is the finite energy splitting between the singlet and triplet states, see Chap. 6. If this energy gap is larger than the spread in the qubit frequencies, transitions away from the singlet subspace are energetically suppressed [58].

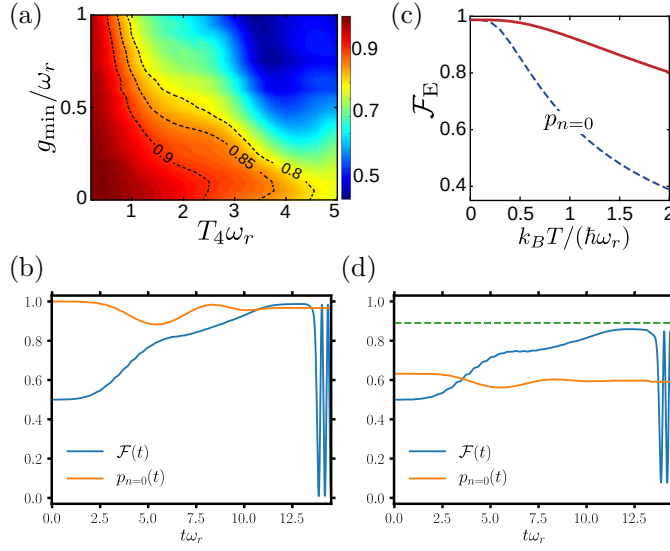


Figure 7.3: (a) The EEF for different g_{\min} and $T_4 (= T_3)$ for a system of $N = 4$ qubits. High EEFs, $\mathcal{F}_E \geq 0.9$, are obtained in a sizeable range of parameters, such that limitations in the switching times and obtainable minimal coupling strengths do not render the protocol useless. (b) $\mathcal{F}(t)$ during the protocol including resonator decay and a $T = 0$ K bath. The quality factor of the oscillator is taken to be $Q = 100$ and $\omega_{\max} = 10\omega_r$. (c) The EEF, red solid line, as a function of the temperature of the initial state of the system, when the oscillator is taken to be in a thermal state in the beginning of the protocol. The blue dashed line gives the occupation probability of the ground state. (d) as (b), but with a finite temperature bath $k_B T = \hbar\omega_r$. Green dashed line denotes the performance of the protocol neglecting the resonator decay. Parameters not explicitly specified are as in Fig. 7.2.

7.3 Experimental imperfections

In experimental realizations of the protocol there might be limitations on the tunability of the parameters $\omega_q(t)$ and $g(t)$ or the diabatic switching times obtainable are longer than what we have assumed. In Fig. 7.3(a) we plot the entanglement extraction fidelity for $N = 4$ qubits as a function of g_{\min} and T_4 . Let us first consider fast switching time $T_4\omega_r < 1$. In this case EEFs of $\mathcal{F}_E \approx 0.8$ can be obtained up to very large $g_{\min} = \omega_r$. Vice versa, for small minimal couplings $g_{\min}/\omega_r \lesssim 0.1$ switching times up to $T_4\omega_r \approx 4.5$ result in EEFs of $\mathcal{F}_E = 0.8$. In the next section we consider the performance of the protocol when the qubit frequency and the coupling are not independently tunable using a flux qubit implementation of the protocol.

Up to now we have not considered dissipative processes during the entanglement extraction protocol. Next we consider the effect of cavity dissipation on the performance of our protocol. Since the qubits and the oscillator are ultra-strongly coupled we cannot use the standard quantum optical master equation [140]. Rather, the coupling has to be taken into account in the derivation of the master equation such that correct jump operators are used. After obtaining the correct jump operators we can move back to the composite basis $|n\rangle |s, m_z\rangle$ with a unitary transformation. During the protocol the qubit frequency and the coupling are changed in time, and, thus, we have to calculate the jump operators at every time step. See App. C for details of the derivation of the master equation and how the time-dependent couplings are handled. In Fig. 7.3(b) we plot the fidelity $\mathcal{F}(t)$ during the protocol for $N = 4$ qubits and a cavity of quality factor $Q = 100$. Even for this extremely low quality factor the protocol is essentially not affected by the resonator decay. This can be understood based on the adiabatic nature of the protocol. During the preparation the system stays at all times in the instantaneous ground state defined by $H(t)$. During the last two steps the cavity decay could in principle have an effect, but these steps take such a short time ω_r^{-1} such that the resonator decay does not have time to have any effect.

We have assumed that the qubits are all identical in our protocol. This is not, however, a strict requirement. A considerable amount of disorder, $\sim \pm 10\%$, in both the frequencies ω_q^i of the qubits and the couplings g_i can be tolerated without losing much of the EEF. In the case of disordered qubit frequencies this is easily understood since the coupling is the dominant energy scale when the qubit entangled ground state is reached. Deviations in the qubit frequencies do not matter since the bare qubit Hamiltonian is irrelevant at that point [58].

7.3.1 Extracting entanglement from a thermal state

In order to reach the large detuning assumed between the qubits and the resonator $\omega_{\max}/\omega_r \approx 20$ the oscillator has to have a rather low frequency $\omega_r/(2\pi) \sim 500$ MHz. This means that even in the ~ 10 mK temperatures of dilution refrigerators the resonator will be thermally occupied. This can be in principle counteracted with cooling methods [128]. However, it is not even necessary. In Fig. 7.3(c) we plot the EEF starting from an initial state where the oscillator is in a thermal state at temperature T as a function of the initial state temperature. For temperatures $k_B T/(\hbar\omega_r) \leq 0.5$ there is essentially no degradation of the achievable EEF. Even for $k_B T/(\hbar\omega_r) = 2$ we obtain $\mathcal{F}_E \simeq 0.8$. Note that only the coherent dynamics has been simulated and the EEF has been obtained by averaging the EEFs for different initial states according to a thermal distribution at the corresponding temperature. The EEF decays much slower than the population of the ground state, blue dashed line in Fig. 7.3(c), showing that the qubit state is effectively mapped to the en-

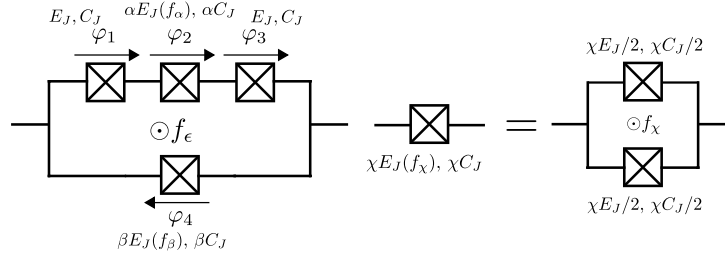


Figure 7.4: Circuit diagram of the tunable four-junction flux qubit. The frequency of the qubit and its coupling to the LC -resonator can be tuned by changing the external fluxes, $f_{\alpha/\beta}$, threading the two SQUID-loops.

tangled $|N/2, 0\rangle$ -state also in the higher Fock-state manifolds. Fig. 7.3(d) shows a master equation simulation at a finite temperature of $k_B T / (\hbar \omega_r) = 1$. The dashed green line shows the obtained EEF neglecting the resonator decay. Even for the very low quality factor $Q = 100$ assumed the difference to the unitary evolution is only $\sim 3.5\%$. The full master-equation simulation justifies the approximate treatment used in Fig. 7.3(c). The robustness against resonator decay is due to the short time of the entire protocol. Even for $Q = 100$ the length of the protocol is only a fraction of the resonator decoherence time $T_f \sim 0.1 \kappa^{-1}$.

Why the protocol works so well, even in the presence of thermal photons in the resonator, can be understood from the effective USC Hamiltonian Eq. (5.25)

$$H_{\text{eff}} = \omega_q e^{-g^2/(2\omega_r^2)} S_z + \frac{\omega_r \omega_q^2}{2g^2} (S_x^2 - \mathbf{S}^2). \quad (7.2)$$

As we have shown numerically it can also qualitatively describe the higher photon manifolds $n > 0$, see Sec. 5.1 and Fig. 5.4. Thus, when the resonator starts in a thermal state the prepared state will be approximately given by

$$|\Psi(T_f)\rangle = \rho_{\text{therm}}^c \otimes |N/2, 0\rangle \langle N/2, 0|, \quad (7.3)$$

such that to a first approximation the qubits and the resonator do not entangle. The quantitative agreement of the effective Hamiltonian in the $n > 0$ manifolds is not as good as in the ground state manifold, such that the obtained EEF is reduced compared to the resonator prepared in its ground state.

7.4 Circuit QED implementation

In this section we present an example implementation of the protocol in circuit QED using flux qubits coupled to a lumped-element LC -circuit. We take the flux

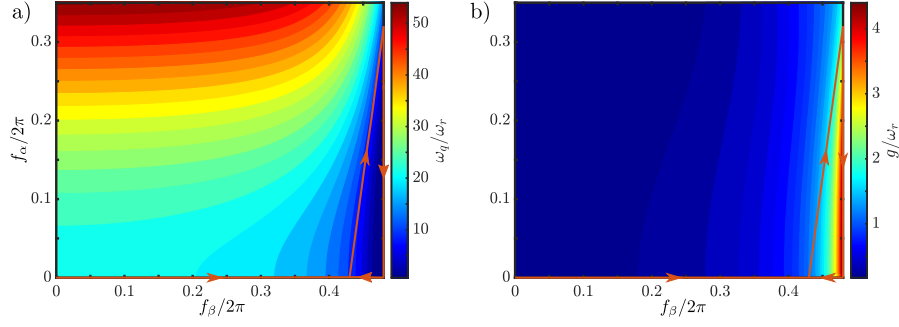


Figure 7.5: Tunability of the qubit. Qubit frequency (a) and coupling (b) as a function of the external fluxes $f_{\alpha/\beta}$. The path that we take in the (f_α, f_β) -space is marked with the orange line and the arrows show the direction in which it is traversed. The parameters for the qubit are given in the main text.

qubits to be the tunable four-junction flux qubit, see Fig. 7.4, we have introduced in Chap. 3. The tunability of the qubit frequencies and couplings is implemented by changing the external fluxes $f_{\alpha/\beta} = \phi_{\alpha/\beta}/\Phi_0$.

We consider the parameters $E_C/h = 4.99$ GHz, $E_J/h = 99.7$ GHz, $\alpha = 0.6$ and $\beta = 6$ for the qubit, and $C = 1.59$ pF and $L = 63.7$ nH for the resonator in the numerical simulations below. These parameters give an LC -oscillator frequency of $\omega_r/(2\pi) = 500$ MHz. The qubit frequency ω_q and the coupling constant g are plotted in Fig. 7.5(a) and (b), respectively, together with the path taken in the (f_α, f_β) -landscape, orange solid line. The starting point is at $(f_\alpha, f_\beta) = (0, 0)$ where the maximal qubit frequency, $\omega_{\max} = 22.8\omega_r$, and the minimal coupling, $g_{\min} = 0.25\omega_r$, are obtained. In the adiabatic stage the fluxes are tuned to $(0, 0.96\pi)$ where the minimal qubit frequency, $\omega_q = 0.7\omega_r$, and maximal coupling, $g = 4.5\omega_r$, are reached. Finally f_β is switched diabatically back to 0.

The pulse shapes for $\omega_q(t)$ and $g(t)$ obtained using the path in Fig. 7.5 are shown in Fig. 7.6(a). We see that the qubit frequency and the coupling cannot be independently tuned using this simple qubit. However, it is important to evaluate the performance of the protocol using this qubit design close to what has been implemented in experiments [39, 41, 42]. The lack of independent tunability reduces the adiabaticity of the protocol due to a different path taken in the (ω_q, g) -landscape, such that the total protocol time is longer than that of the ideal protocol. The fidelity during the protocol is plotted in Fig. 7.6(b) for $N = 4$ qubits. Even with these non-ideal pulse shapes the obtained EEF for four qubits is very good $\mathcal{F}_E > 0.9$ and for two qubits it goes up to $\mathcal{F}_E \approx 0.96$ (not shown). Thus, the protocol performs very well even under these non-ideal conditions.

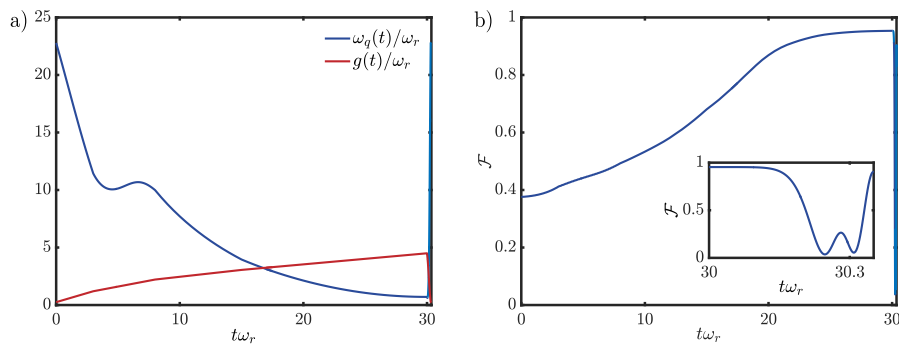


Figure 7.6: The protocol as implemented using tunable flux qubit of [sub-Sec. 3.4.2](#). (a) Pulse shapes of $\omega_q(t)$ and $g(t)$ obtained by the path marked in [Fig. 7.5](#). (b) The fidelity during the entanglement extraction protocol using the pulse shapes of (a). The plot is for $N = 4$ qubits and parameters are given in the text. Inset: a zoom to the end of the protocol.

Chapter 8

Simulating non-perturbative cavity QED

In the previous chapters we have considered the EDM as a fundamental description of physical systems. However, experimentally realizing systems in the USC regime with multiple two-level-systems is challenging, and, thus, so far only systems with a single two-level-system ultra-strongly coupled to a mode have been realized [41, 42]. Quantum simulation, digital and analog, is a powerful method to simulate quantum systems [141, 142]. In a digital simulation the dynamics of a system or its quantum ground state are approximated by applying gates on a system of qubits. In analog simulation, on the other hand, the Hamiltonian of another quantum system is implemented as the effective Hamiltonian of the simulator, possibly in some rotating frame.

Trapped ions [143] are a well developed platform for quantum simulation [144–146]. In this chapter we propose to simulate, in an analog manner, non-perturbative light-matter systems with trapped-ions. We begin by showing how to implement the general cavity QED Hamiltonian ($\hbar = 1$)

$$H_{c\text{QED}} = \omega_r a^\dagger a + \omega_q S_z + g(a^\dagger + a)S_x + \frac{g^2}{\omega_r} S_x^2 + \sum_{i,j} \frac{D_{ij}}{4} \sigma_i^x \sigma_j^x \quad (8.1)$$

with the trapped-ion quantum simulator. Note, in this chapter we assume an independent scaling of the P^2 -term and the dipole-dipole interactions D_{ij} in contrast to Chap. 5. We take for simplicity the qubits to be identical and the couplings homogeneous. The other half of the chapter is devoted to possible applications and experiments that could be performed with the system. Trapped-ion systems have already been used to simulate the Rabi model [147, 148] and the Dicke model [149–151], and the dynamics of the Rabi model in the USC regime has been simulated also digitally using SC qubits [152]. The Dicke SRPT has been realized

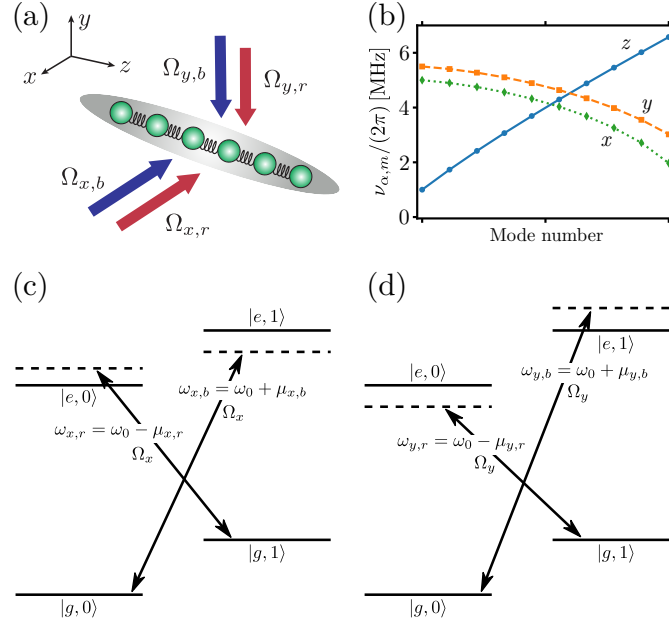


Figure 8.1: The setup: (a) A sketch of the setup. (b) Normal mode frequencies of the crystal. The trap is taken to be stiffest along the y -axis and softest along longitudinal z -axis, $\nu_z < \nu_x < \nu_y$. Specifically we consider $\nu_z = 2\pi \times 1$ MHz, $\nu_x = 2\pi \times 5$ MHz and $\nu_y = 2\pi \times 5.5$ MHz. (c) Detunings of the driving lasers along x -axis, and (d) y -axis.

in driven-dissipative scenarios with atoms in cavities [98–101, 153]. Proposals for simulating the Rabi- and Dicke-models with cold neutral atoms trapped near to tapered optical fibres also exist [154].

8.1 Trapped-ion implementation of the EDM

We consider a chain of ions trapped in a linear Paul trap, Fig. 8.1(a). The axis of the chain is assumed to be directed along the z -axis. The trapping frequency along the z -axis is smaller than in the two orthogonal directions. We take the x - and y -axes trap frequencies to be off-resonant to avoid any accidental resonances. Fig. 8.1(b) shows the normal mode frequencies. The ions are driven with pairs of lasers along the x - and y -axes, with frequencies $\omega_{\alpha,l}$, amplitudes $\Omega_{\alpha,l,i}$ and phases $\phi_{\alpha,l}$, with $\alpha = x, y$ labelling the axis and $l = r, b$ the laser. The Hamiltonian of the system in a frame rotating with the free-ion Hamiltonian $H_0 = \sum_i \omega_0 \sigma_i^z / 2$ is

given by [143]

$$H_I = \sum_{\alpha,l,i} \frac{\Omega_{\alpha,l,i}}{2} \left[\sigma_i^+ e^{i(k_{\alpha,l} r_{\alpha,i} + \delta_{\alpha,l} t - \phi_{\alpha,l})} + \text{H.c.} \right], \quad (8.2)$$

where $\delta_{\alpha,l} = \omega_q - \omega_{\alpha,l}$ and we have used the optical RWA to neglect terms $\propto e^{\pm i(\omega_0 + \omega_{\alpha,l})t}$. The ions are treated as two-level-systems with frequency ω_0 and the frequencies of the normal modes of the ions' motion are $\nu_{\alpha,m}$. In the above equation $r_{\alpha,i} = \sum_m r_{\alpha,i,m}^{\text{zpf}} u_{\alpha,i,m} (b_{\alpha,m}^\dagger + b_{\alpha,m})$ is the position operator of ion i around the equilibrium position $r_{\alpha,i}^{(0)}$ on axis α . The zero-point amplitude for mode m along α is $r_{\alpha,i,m}^{\text{zpf}} = \sqrt{\hbar/(2M\nu_{\alpha,m})}$, with M the mass of the ion, and $u_{\alpha,i,m}$ is the envelope of the normal mode m at the position of the ion n .

8.1.1 Collective TLS-field coupling

Let us start by engineering the collective Dicke coupling $H_{\text{int}} = g(a^\dagger + a)S_x$ between the qubits and the mode. The normal modes in the x-axis will be used for this purpose, and the centre of mass (COM) mode in the x-axis plays the role of the photonic mode a . In order to realize H_{int} we choose the laser frequencies as in Fig. 8.1(c). The ions are driven near the first red and blue COM side-band resonances $\omega_{x,l} = \omega_0 \pm (\nu_{x,c} - \Delta_{x,l})$, where $\Delta_{x,l} \ll \nu_{x,c}$ is a small detuning from the exact resonance and $\nu_{x,c} = \nu_x$ is the COM mode frequency. The plus sign corresponds to the blue laser $l = b$ and minus for the red laser $l = r$. The amplitudes of the red and blue lasers are chosen to be equal and homogeneous $\Omega_{x,r,n} = \Omega_{x,b,n} = \Omega_x$ and the phases are also set to be equal $\phi_{\alpha,1} = \phi_{\alpha,2} = \pi/2$. The Hamiltonian in the Lamb-Dicke (LD) regime and in a RWA keeping only the COM first side-band transitions the Hamiltonian becomes [147]

$$H_{I,x} = \sum_n \frac{\Omega_x \eta_{x,c} u_{x,c}}{2} \left[\sigma_n^+ (b_{x,c}^\dagger e^{i\Delta_{x,b}} + b_{x,c} e^{i\Delta_{x,r}}) + \text{H.c.} \right], \quad (8.3)$$

where $b_{x,c}^{(\dagger)}$ is the annihilation (creation) operator of the COM mode and $\eta_{x,c} = k_x r_{x,c}^{\text{zpf}}$ is the Lamb-Dicke parameter for COM mode, which in the LD regime satisfies $\eta_{x,c} \sqrt{\langle (b_c^\dagger + b_c)^2 \rangle} \ll 1$. Additionally we have moved to a rotating frame with respect to the x-modes of the crystal. The COM mode has a uniform mode envelope $u_{x,c,i} = 1/\sqrt{N} \equiv u_{x,c}$. By introducing the effective frequencies [147]

$$\begin{aligned} \omega_r &= \frac{1}{2}(\Delta_{x,b} + \Delta_{x,r}) \\ \omega_q &= \frac{1}{2}(\Delta_{x,b} - \Delta_{x,r}) \\ g &= \Omega_x \eta_x u_{x,c} \end{aligned} \quad (8.4)$$

and after performing a unitary transformation $\mathcal{U}(t) = \exp[-i(\omega_q S_z + \omega_r a^\dagger a)t]$ to eliminate the time-dependence we obtain the effective Hamiltonian

$$H_x^{\text{eff}} = \omega_r a^\dagger a + \omega_q S_z + g(a^\dagger + a)S_x, \quad (8.5)$$

where we have renamed $b_{x,c}$ to a . Thus, the effective Hamiltonian implemented by the x-modes is that of the Dicke model and we have a collective coupling of the ions to the COM mode in that axis. The effective parameters Eq. (8.4) are easily tunable by the laser detunings $\Delta_{x,r/b}$ and amplitude Ω_x .

8.1.2 The P^2 -term

We proceed with the y-modes, which will be used to implement the collective S_x^2 -term. The detunings of the driving lasers are set to $\delta_{y,l} = \pm\mu_y - \omega_q$, where $\mu_y = \nu_{y,c} + \Delta_y$, $\nu_{y,c}$ is the COM frequency in the y-direction and the plus and minus signs correspond to the blue, $l = b$, and red, $l = r$, lasers, respectively, see Fig. 8.1(d). The ω_q dependence of the driving laser frequencies are needed due to the effective field ω_q created using the transverse x-modes. The Hamiltonian for the y-driving lasers in the Lamb-Dicke regime after neglecting other terms than the first side-band transition in a RWA is given by [155, 156]

$$H_{I,y} = \sum_{i,m} \frac{\Omega_y \eta_{y,m} u_{y,i,m}}{2} (\sigma_i^+ e^{i\omega_q t} + \text{H.c.}) \sin(\mu_y t) (b_{y,m}^\dagger e^{i\nu_{y,m} t} + \text{H.c.}), \quad (8.6)$$

where $\eta_{y,m} = k_y r_{y,m}^{\text{zpf}}$ is the Lamb-Dicke parameter for y-mode m . We have assumed the driving lasers to have equal and homogeneous amplitude $\Omega_{y,l,i} = \Omega_y$ and the phases have been set to $\phi_{y,b} = 0$, $\phi_{y,r} = \pi$. Without the external field ω_q the time-evolution created by Eq. (8.6) can be calculated exactly using a Magnus expansion [155, 156]. In the presence of ω_q we can calculate it to second order and obtain the following time-evolution operator

$$U(t) = \exp \left[-i \sum_{i,m} (\beta_{i,m}(t) b_{y,m}^\dagger + \text{H.c.}) \sigma_i^x - i \sum_{i,j} \frac{\phi_{ij}}{4} \sigma_i^x \sigma_j^x \right], \quad (8.7)$$

where

$$\beta_{i,m}(t) = \Omega_y \eta_{y,m} u_{y,i,m} \frac{\mu_y - e^{i\nu_{y,m} t} (\mu_y \cos(\mu_y t) - i\nu_{y,m} \sin(\mu_y t))}{\mu_y^2 - \nu_{y,m}^2}, \quad (8.8)$$

$$\phi_{ij} = \sum_m \frac{2\Omega_y^2 \eta_{y,i,m} \eta_{y,j,m}}{\mu_y^2 - \nu_{y,m}^2} \left[\nu_{y,m} t - \frac{\nu_{y,m} \sin(2\mu_y t)}{2\mu_y} + \frac{\sin((\mu_y + \nu_{y,m})t)}{\mu_y + \nu_{y,m}} - \frac{\sin((\mu_y - \nu_{y,m})t)}{\mu_y - \nu_{y,m}} \right]. \quad (8.9)$$

The presence of the local field generates a term $\propto b_{y,m}^\dagger b_{y,m} \sigma_n^z$ which is, however, suppressed by a factor $\omega_q/(\mu_y - \nu_{y,m})$ and can be neglected in the parameter regime of interest [157]. The first term in Eq. (8.7) coherently displaces the modes by an amount $\sum_i \beta_{i,m}(t) \sigma_i^x$ depending on the ions' state, which leads to entanglement between the ions and the modes. In order to create pure spin-spin interactions we, thus, require $\beta_{i,m}(t) \ll 1$, such that the modes are only virtually excited. The second term gives a conditional phase between two ions i and j . In the limit of long evolution times $t\nu_{y,m} \gg 1$ the phase factor is given by the secular term, $\propto t$, in Eq. (8.9). Thus, the time-evolution at long times is created by the effective Hamiltonian

$$H_y^{\text{eff}} = \sum_{i,j} \frac{D_{ij}}{4} \sigma_i^x \sigma_j^x, \quad (8.10)$$

where the dipole-dipole coupling strength is given by [158–163]

$$D_{ij} = \sum_m \frac{2\Omega_y^2 \eta_{y,m}^2 u_{y,i,m} u_{y,j,m} \nu_{y,m}}{\mu_y^2 - \nu_{y,m}^2}. \quad (8.11)$$

The shape of D_{ij} can be tuned by choosing μ_y close to a specific mode $\nu_{y,m}$. Then the mode function $u_{y,i,m}$ of that mode will be reflected in the DD interaction matrix D_{ij} [164]. We choose the detuning close to the COM mode, such that the dipole-dipole couplings will be mainly homogeneous

$$D_{ij} \simeq \frac{(\Omega_x \eta_{x,c} u_{y,c})^2}{\Delta_y} \quad (8.12)$$

for all i, j with smaller corrections coming from the far off-resonant modes. By choosing μ_y in the middle of the band one obtains couplings with alternating signs, leading to frustration and related effects [161].

8.1.3 Dipole-dipole interactions

In order to implement the short-range dipole-dipole interactions present in the EDM, we generalize the scheme from above to laser beams with multiple sidebands with different frequencies. This can be taken into account by replacing

$$\Omega_y e^{i\delta_{y,l} t} \rightarrow \sum_n \Omega_{y,n} e^{i\delta_{y,l,n} t} \quad (8.13)$$

in Eq. (8.2). The Hamiltonian is then given by that of Eq. (8.6) with a sum over the different sidebands n . Asserting that the detunings between different sidebands remain large, $\eta_{y,m} \Omega_{y,n} \ll |\delta_{y,l,n} - \delta_{y,l,n'}|$, the cross terms from lasers with

different sideband frequencies that are created are rapidly oscillating and, thus, can be safely neglected. The spins are then described by the effective Hamiltonian of Eq. (8.10), and the generalized dipole-dipole matrix is given by

$$D_{ij} = \sum_{m,n} 2 (\Omega_{y,n} \eta_{y,m})^2 \frac{\nu_{y,m} u_{y,i,m} u_{y,j,m}}{\mu_{y,n}^2 - \nu_{y,m}^2}. \quad (8.14)$$

It can be engineered by combining multiple near-resonant and/or far-detuned lasers. The short-range dipole-dipole interactions can then be implemented by adding a laser which is far detuned from all of the modes [158, 160], adding a component to D_{ij} which decays roughly as $\sim |i - j|^{-3}$ for very large detuning.

8.1.4 Accessible parameter regimes

In summary, we have show that by addressing different phonon branches of the ion chain, collective spin-mode and dipole-dipole interactions can be engineered. Thus, by combining the schemes, we obtain

$$H_{\text{cQED}} = H_{\text{eff}}^{(x)} + H_{\text{eff}}^{(y)} \quad (8.15)$$

with a dipole-dipole interaction matrix given by

$$J_{ij} = D_{ij} - \frac{g^2}{\omega_c}. \quad (8.16)$$

This completes our goal of engineering Eq. (8.1) as the effective Hamiltonian of the ions. In theory this approach gives us full control over the model parameters, but the hierarchy of frequency scales and the single-mode addressability assumed in the derivation, impose limitations on the accessible parameter regimes. This will be discussed next.

Ultra-strong coupling regime

As a concrete example we consider a chain of $N = 10$ trapped $^{40}\text{Ca}^+$ ions with a phonon spectrum of Fig. 8.1(b). The LD parameter for the x -motion is $\eta_{x,c} = 0.043$, and for $\Omega_x = 2\pi \times 15.4$ kHz, $\Delta_{x,b} = 2\pi \times 0.41$ kHz and $\Delta_{x,r} = 0$ we obtain $\omega_r = \omega_q = 2\pi \times 0.21$ kHz and a coupling parameter of $g/\omega_r = 1$. The P^2 -term is implemented by the scheme discussed above and we use a pair of lasers with Rabi-frequency $\Omega_{y,1} = 2\pi \times 139$ kHz to drive the COM mode with detuning $\Delta_{y,1} = 2\pi \times 14$ kHz. For LD parameter $\eta_{y,c} = 0.041$ this gives us a collective S_x^2 -coupling of magnitude $g^2/\omega_c = D = 2\pi \times 0.21$ kHz. Since the driving laser couples to all other y -modes as well, the exact evaluation of the coupling matrix D_{ij} in Eq. (8.14)

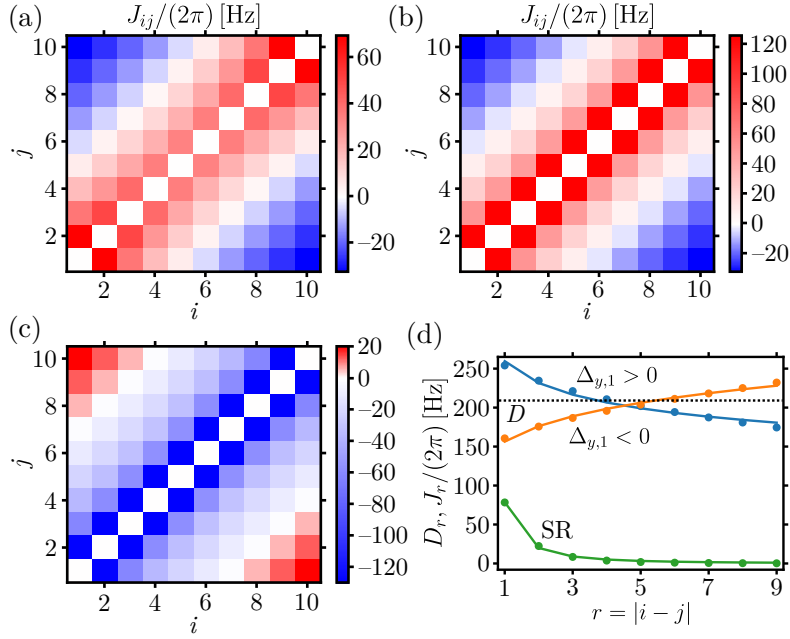


Figure 8.2: Engineered dipole-dipole interactions for $N = 10$ ions. (a) The residual dipole-dipole interaction matrix of the non-interacting system. The case of repulsive (b) and attractive (c) dipole-dipole interactions. (d) The distance dependence $D_{r=|i-j|}$ of the interaction matrix elements for a single near-resonant pair of lasers, two upper solid lines with markers, averaged over the chain. The lowest line with markers shows the distance dependence of the dipole-dipole interactions for the far-detuned laser pair. The solid lines are fits to the markers giving $\alpha \approx \pm 0.16$ for the upper lines and $\alpha \approx 2$ for the lowest line. The black dotted line gives the value of D specified in the text.

results in small spatial variations, $D_{ij} \sim |i - j|^{-0.16}$. The resulting residual dipole-dipole interactions, J_{ij} , are shown in Fig. 8.2(a). Each dipole feels a residual field $\bar{J}_i = \sum_{j \neq i} J_{ij}$ on average, whose variance is $(\Delta \bar{J})^2 = \sum_n (\bar{J}_i)^2 / N$. For the parameters we consider $\Delta \bar{J} / \omega_q \approx 0.19$, such that the qubits are approximately non-interacting. Since the P^2 -term scales as $\propto g^2$ the imperfections J_{ij} share this scaling, and become negligible for small g .

To add the short-range dipole-dipole interactions, we use another pair of lasers along the y -axis with Rabi-frequency $\Omega_{y,2} = 2\pi \times 1.0$ MHz and detuning $\Delta_{y,2} = 2\pi \times 1.7$ MHz. Since the lasers are far detuned the coupling to all the phonon modes is approximately equal. The dipole-dipole interactions resulting from this laser pair are approximately given by $J_{ij} \approx J_0 / |i - j|^\alpha$, with $\alpha \approx 1.98$ and $J_0 = 2\pi \times 80$ Hz. The total mean field introduced by these lasers $\bar{J} \approx 2\pi \times 0.20$ kHz is on the order of

ω_q . The coupling matrix J_{ij} , including imperfections from the P^2 -term, is plotted in Fig. 8.2(b). The value of $\alpha \lesssim 2$ is limited by the ratio between the bandwidth of the y phonon modes and the detuning. For a 1D chain the $|i-j|^{-2}$ couplings can be considered as mid-range [165]. Since the beat-note of the far detuned pair of lasers must be larger than the COM frequency, $\mu_{y,2} > \nu_{y,c}$, the effective interactions are always repulsive. In order to implement an equivalent model with $J_{ij} < 0$, we can reverse the sign of the other terms in H_{EDM} [166]. This is obtained by replacing $\Omega_x \rightarrow -\Omega_x$ and reversing the sign of the detunings, $\Delta_{x,r/b}$ and $\Delta_{y,1}$. This trick results in the model $-H_{\text{cQED}}$ with $J_0 < 0$. The overall minus sign is irrelevant for the quantum simulation. The resulting attractive dipole-dipole interactions are plotted in Fig. 8.2(c) for $\Delta_{y,1} = -2\pi \times 11 \text{ kHz}$ and $\Omega_{y,1} = 2\pi \times 112 \text{ kHz}$. Apart from the sign, these parameters give essentially the same effective parameters as above.

We have shown that trapped ions can be used to engineer few-body cavity QED models with coupling constants $g/\omega_r \sim O(1)$ at absolute frequency scales of a few hundred of Hz. These scales are still fast compared to simulation times of tens of milliseconds available in state-of-the-art trapped-ion experiments [157, 167].

Non-perturbative regime

Above we have shown that reaching the regime of $g/\omega_r \sim 1$ is possible with our trapped-ion implementation of the EDM. As shown in Chap. 5 significant non-perturbative changes in the ground state of the EDM happen beyond $g/\omega_r \gtrsim 2-3$. In order to simulate this regime two difficulties arise. Firstly, for a fixed value of $D \approx 2\pi \times 200 \text{ Hz}$ the qubit and mode frequencies have to be an order of magnitude lower $\omega_{r,q} \approx 2\pi \times 20 \text{ Hz}$ than before, leading to longer absolute time scales. In addition to this a smaller value of ω_q also means that the variations in D_{ij} will become more important, $\Delta\bar{J}/\omega_q \approx 2$ and the qubits can no longer be considered non-interacting. In general these issues are worse for larger N , since the mode spacing of the crystal is smaller making the single mode addressability harder to achieve. This results in a competition between the time scale of the simulation and the fidelity of the realized model. For small and moderate number of ions, however, many interesting effects can be explored within these constraints. It also has been shown [168, 169] that with single ion addressability and machine learning algorithms, it is possible to improve the quality of the created spin models significantly.

8.2 Examples

The above analysis shows that trapped ions can be used to simulate regimes of cavity QED at the moment inaccessible in other experiments. In this section we present two examples, also illustrating possible measurements that one can apply to gather information about the system. We begin by considering the excitation spectrum of a cavity QED system and later use the ground state preparation scheme of [Chap. 7](#) to probe the light-matter decoupled ground state in the USC regime.

8.2.1 Qubit excitation spectrum

The first example we consider is the measurement of the excitation spectrum of a cavity QED system. We consider the parameter regime $g/\omega_r \lesssim 1$. In order to measure the excitation spectrum the ions are prepared in their ground state $|g\rangle$ and the phonon mode is cooled to its ground state. At this point the couplings are gradually switched on such that the system is adiabatically prepared into the ground state $|G\rangle$ of [Eq. \(8.1\)](#). Then a weak perturbation $H_p(t) \sim Ae^{-i\omega t} + A^\dagger e^{i\omega t}$ is applied for a time T_p . For long pulses $T_p \rightarrow \infty$ the amount of excitations created by the perturbation is proportional to the excitation spectrum

$$S(\omega) = \frac{\Gamma}{2} \Re \int_0^\infty d\tau \langle A(\tau) A^\dagger(0) \rangle_{\rho_0} e^{i\omega\tau}, \quad (8.17)$$

where the average is taken with respect to the state $\rho_0 \approx |G\rangle \langle G|$ obtained with the adiabatic preparation. Practically speaking, a difference in the measurement of $\langle A^\dagger A \rangle$ before and after the perturbation gives a good estimate of $S(\omega)$ for a finite T_p .

If one takes $A = a$, a measurement of the cavity spectrum is performed. We choose instead $A = \sigma_3^-$, in which case the spectrum also contains information about the dark excitations of the qubits not coupled to the mode. In [Fig. 8.3](#) we plot the numerically calculated spectra for $N = 6$ qubits. Other parameters are similar as discussed above. In our case a purely adiabatic preparation of the ground state was not feasible, taking a time of hundreds of milliseconds, and a non-adiabatic bang-bang scheme was used [[151](#), [170](#), [171](#)]. Using this scheme we are able to prepare the ground state with a fidelity $\mathcal{F} = \langle G | \rho_0 | G \rangle \gtrsim 0.8$ within $T_{\text{prep}} \lesssim 7$ ms. Using this prepared state the spectrum is evaluated assuming a common phenomenological decay rate $\Gamma = 2\pi \times 4$ Hz for all states, corresponding to experimental runtime of $T_p \approx 40$ ms.

In the excitation spectrum the USC regime can be identified as the regime where the splitting between the upper and lower polariton modes $\Delta\omega$ no longer follows the initial linear behaviour $\Delta\omega \sim G = \sqrt{N}g$. In [8.3\(a\)](#), corresponding

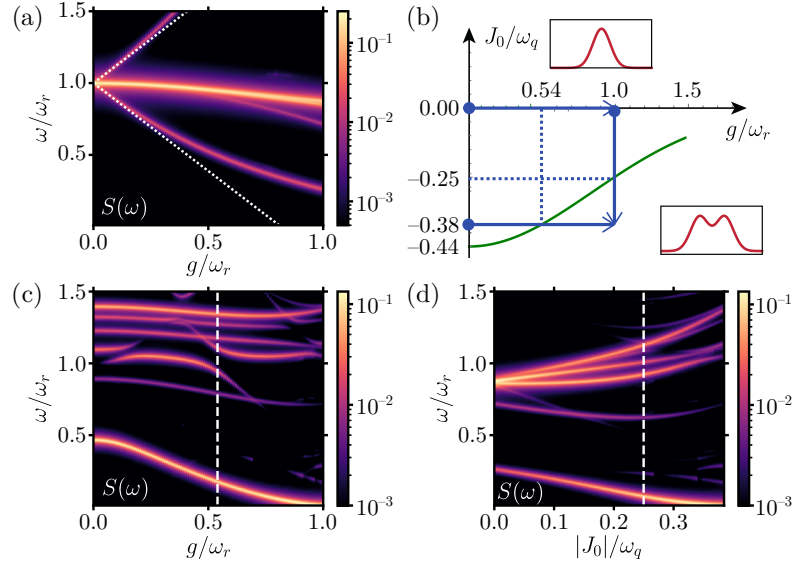


Figure 8.3: Excitation spectra of $N = 6$ non-interacting qubits, $J_0 = 0$, for varying g (a). The dotted lines indicate the initial linear scaling of the polaritonic branches $\omega_r \pm G/2$. (b) Sketch of the phase boundary (green line) between the normal and the ferroelectric phase. The insets show the behaviour of the $p(m_x)$ distribution in the two phases. Parameter sweeps in (a), (b) and (c) are indicated by the blue arrows. In (c) and (d) the phase boundary is crossed by changing the qubit-photon coupling g for $J_0/\omega_q \simeq -0.38$ and the DD interaction strength J_0 , and $g/\omega_r = 1$, respectively. The dashed lines indicate the point at which the phase boundary is crossed. We have used $\omega_q = \omega_r$ for all plots.

to non-interacting dipoles $J_{ij} = 0$ (up to small corrections c.f. Fig. 8.2(a)), the linear scaling can be observed for small G . Due to probing a single ion, the response is sensitive to all excitation modes and the coupling to the collective polariton modes is reduced by a factor N^{-1} . Being able to observe both collective and single-qubit effects is, thus, an interesting feature of the few-qubit regime. For larger couplings the P^2 -term starts to become important and the spectrum deviates from the predictions of the DM [44, 172–175]. The most important difference being that the lower polariton branch stabilizes to a non-vanishing value for any coupling [44, 172]. Another interesting feature of the few-qubit regime is the redshift of the dark polariton modes seen in Fig. 8.3(a). It is caused by the fact that the ground state energy $E_G(g)$ is an increasing function of the coupling g . When a qubit is excited to a dark mode less energy is required. This cannot be predicted by a purely linear theory, and conversely not observed in traditional experiments in the optical and THz regime, where the single qubit-photon coupling $g \ll \omega_r$ and

only the linearized collective interaction of a large number, $N \gg 1$, of qubits is available. Non-linear effects such as this are expected to be observable only for a moderate number of qubits $N \lesssim 10$ [176]. The presence of the small residual DD interactions can also be observed in Fig. 8.3(a) as the finite splitting between the dark polariton modes.

Consider next a system with strong attractive dipole-dipole interactions, $J_{ij} \approx J_0/|i-j|^\alpha$ with $J_0 < 0$. In this situation the qubits can exhibit a phase transition to a ferroelectric state at a critical coupling J_0^c . For $\alpha = 2$ and in the thermodynamic limit the critical value $J_0^c/\omega_q \simeq -0.4$ is obtained [177]. When the qubits are additionally coupled to a cavity the critical DD coupling is expected to decrease as

$$J_0^c(g) \approx J_0^c(g=0)e^{-g^2/(2\omega_r^2)}, \quad (8.18)$$

due to the qubits getting dressed by virtual cavity photons, see Chap. 5. This is a purely non-perturbative effect absent in the Dicke model, where the transition is driven by strong ferroelectric DD interactions $J_{ij} = -g^2/\omega_r$ and is only weakly modified by the presence of the cavity mode [51]. For the $N = 6$ qubits considered only a crossover between the normal phase and the ferroelectric phase takes place. It is possible, however, to find the phase boundary by considering the probability distribution

$$p(m_x) = \langle G | \mathbb{P}_{m_x} | G \rangle, \quad (8.19)$$

where $\mathbb{P}_{m_x} = \sum_s \mathbb{P}_{s,m_x}$ is the projection operator to collective spin states with total spin s and x -projection m_x , $S_x |s, m_x\rangle = m_x |m_x\rangle$. In the normal phase this distribution has always a single maximum at minimal $|m_x|$. In contrast in the ferroelectric phase the distribution is bi-modal with the maximal weight at $m_x = \pm s$ for very large couplings. The phase diagram and $p(m_x)$ in the different phases are sketched in Fig. 8.3(b).

As we see from Eq. (8.18), the phase boundary can be crossed in two ways: Either one can increase the qubit-photon coupling g while keeping $|J_0| < |J_0^c|$ constant or by increasing the DD coupling $|J_0|$ directly. The spectra corresponding to these cases are plotted in Fig. 8.3(c) and (d). In both cases the frequency of first excitation mode approaches zero at the phase boundary, but stays finite due to finite size corrections, as expected. Even though the lowest excitation mode behaves very similarly in both tuning schemes, there is a clear difference in the excited states. When tuning the qubit-photon coupling there are many avoided crossing around ω_r indicating a strong hybridization with the mode. These features are completely absent in the case where J_0 is tuned.

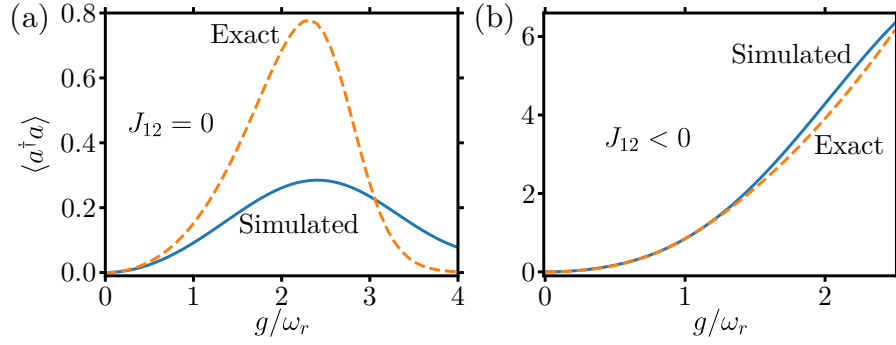


Figure 8.4: Adiabatic ground-state preparation in the USC regime for (a) non-interacting qubits $J_{12} = 0$ and (b) $J_{12}/\omega_c = -3.5$. Starting from the normal ground state $|n = 0\rangle \otimes |m_z = -N/2\rangle$, the ground state is prepared by adiabatically turning on the qubit-photon coupling and DD interactions during a time of $T_{\text{prep}} \lesssim 10$ ms for a given pair (g, J_0) . In both cases we have taken $\omega_q = \omega_r$.

8.2.2 Ground state preparation

As we have shown above, the first non-perturbative corrections are observable in the regime $g/\omega_r \lesssim 1$. However, the ground state is still essentially determined by ω_q and J_{ij} , while the effect of the cavity mode can be only seen in the excited states. For large enough coupling $g/\omega_r \gtrsim 2$ this is no longer the case. In this regime, in addition to renormalizing ω_q , see Eq. (8.18), the qubit-photon coupling also creates effective anti-ferroelectric interactions between the qubits, see Chap. 5,

$$H_{\text{AF}} = \frac{\omega_r \omega_q^2}{2g^2} (\mathcal{S}_x^2 - \mathcal{S}^2). \quad (8.20)$$

These effective interactions compete with $|J_0|$ favouring a subradiant ground state with completely anti-aligned qubits, that decouple from the cavity, see Chap. 5.

Experimentally this physics can be seen already in the simple case of $N = 2$ ions. In this case the interaction matrices reduce to a single relevant parameter $D_{ij} = D$ and $J_{ij} = J_0$. The detuning constraints are relaxed, which allows us to consider $D = g^2/\omega_r = 2\pi \times 2$ kHz corresponding to a value of $\omega_r = \omega_q = 125$ kHz for $g/\omega_r = 4$. In Fig. 8.4 we plot the expectation value of the simulated ground state photon number $\langle a^\dagger a \rangle$ for non-interacting qubits $J_0 = 0$, (a), and ferroelectrically coupled qubits $J_0/\omega_q = -3.5$, (b). In this case an adiabatic preparation is possible in a reasonable time and that is what has been used, see Chap. 7 for details. For small values of the coupling constant g , both cases show an increase in the photon number as expected from the hybridization of the mode and the qubits. In the ferroelectric case this trend continues for larger couplings, experiencing a

rapid increase after $g/\omega_r \approx 1$, as one expects in the superradiant phase. In the non-interacting system the increasing trend turns around after $g/\omega_r \gtrsim 2$, and for $g/\omega_r \approx 4$ the cavity mode has approximately returned into the vacuum state. The simulated ground state photon number differs from the correct value for the preparation time $T_{\text{prep}} \approx 10$ ms used here, but it shows the correct qualitative behaviour, especially the characteristic maximum of $\langle a^\dagger a \rangle$, a witness of entering the subradiant regime [51], is reproduced. This effect can be easily confirmed in the trapped-ion platform by doing full tomography of the internal state of the ions. We find a high fidelity of $\text{Tr}[\rho_0 |T\rangle \langle T|] \approx 0.95$, where $|T\rangle = (|eg\rangle + |ge\rangle)/\sqrt{2}$ is the triplet state minimizing Eq. (8.20), for the largest coupling.

8.3 Discussion

In this chapter we have shown that trapped ions can be used to implement quantum simulation of non-perturbative cavity QED. This platform offers a flexible way to tune both the interactions between the qubits and a cavity mode, and the direct dipole-dipole interactions. In the two examples presented, we have highlighted some possibilities for observing signatures of non-perturbative light-matter interactions.

We have used a small number of ions, for which we can benchmark the performance of the simulation with exact numerical methods. In this sense the simulation aspect lies in the possibility of studying light-matter interactions in a regimes not accessible today with systems of real or artificial atoms, rather than simulating systems beyond the scale of classical simulations. The proposal presented can be, however, extended to tens of ions and/or multiple modes, allowing to study non-perturbative effects in systems well beyond the reach of classical capabilities. The main difficulty in increasing the simulation scale is the collective P^2 -term, $\sim g^2/\omega_r S_x^2$, which is the most dominant term in the USC regime. This term is created by addressing a single transverse normal mode of the ion crystal, which becomes more difficult the larger the crystal is, in turn increasing the experimental runtime. In the future with improved motional heating rates and ion coherence times, second scale quantum simulations can become available, enabling the extension of the proposed scheme to tens of ions.

Chapter 9

Summary and Outlook

In this thesis we have studied the interaction between light and matter in the ultra-strong coupling regime. The main focus has been in circuit QED systems, since they offer an experimentally relevant platform in realizing ultra-strong light-matter couplings.

We started with a brief introduction to Hamiltonian circuit theory and basic phenomena of superconductivity, namely the Josephson effect and flux quantization, needed to understand superconducting (SC) circuits. The quantum LC -oscillator was introduced and two prototypical type of SC qubits, the charge qubit and the flux qubit. The two main coupling schemes, capacitive and inductive coupling, between qubits and LC -circuits in experiments were discussed. The suitability of the coupling schemes for USC were discussed and limits to the obtainable coupling strengths were derived.

[Chap. 4](#) started with a review of the main USC models used in the literature. The superradiant phase transition of the Dicke model and the no-go theorem were discussed. Then, by starting from three different microscopic circuit models representing superconducting qubits, we showed that the Extended Dicke model must be used to correctly capture the USC physics of multi-qubit circuit QED systems. It was shown that the Extended Dicke model is the accurate two-level-truncated Hamiltonian in the USC regime, while the traditional Dicke model, derived in the Coulomb gauge, fails due to the momentum coupling to the field.

In [Chap. 5](#) the ground state properties of the EDM were discussed first in the case of non-interacting qubits, and it was shown that there is no SRPT in this model. The ground state in the USC regime is in a new subradiant phase, where the qubits form a highly entangled state and decouple from the resonator mode. Next the treatment was expanded to include dipole-dipole interactions between the qubits in a collective approximation. The ground state phase diagram of light-matter systems was explored as a function of the light-matter coupling strength and the DD interaction strength. In the case of repulsive dipole-dipole interac-

tions it was shown that the ground state is also in the subradiant phase as in the case of non-interacting qubits. For attractive DD interactions the ground state was shown to be in the superradiant phase for sufficiently strong couplings. This allowed us to give a new interpretation of the Dicke SRPT as an instability of the interacting qubit ensemble which is not created by coupling the TLSs with the mode. For extremely strong light-matter coupling it was shown that a new type of phase transition exist where the system transitions directly from the superradiant vacuum to the subradiant phase, the super-to-subradiant phase transition. The new PT is reminiscent of a first order phase transition, with the important difference that at the critical point more than two states become degenerate. Including quantum corrections it was shown that the transition from the superradiant to the subradiant phase happens at a finite attractive DD interaction strength.

In [Chap. 6](#) we moved our focus to the excited states of the EDM, whereas in the previous chapters mainly the ground state physics was considered. A regime where the qubits and the resonator have very dissimilar frequencies, the resonator frequency being much smaller than the qubit frequency, was considered. In this case a Born-Oppenheimer approximation can be used to separate the fast and slow dynamics of the qubits and the resonator, respectively. The qubits create an effective potential for the resonator, whose shape depends on the light-matter and DD coupling strengths and the number of coupled qubits. It was shown that the BO potentials show various instabilities in the ground and excited states. Schemes to detect an instability in the excited states were presented. The first possibility is to perform single qubit excitation spectroscopy. An instability can be detected as a splitting of the excitation spectrum above the critical coupling of the transition for a thermal resonator. As another method a Ramsay-type scheme was presented. The qubits are driven in a superposition state and the resonator is let to evolve in a superposition of effective potentials. Measurements of the coherence of the qubit state in the energy basis, then reveal the motion of the resonator in the BO potential. Importantly the presented schemes only involve operations in the frequency scale of the qubit, such that standard circuit QED methods and measurements can be applied.

A scheme to extract entanglement from the subradiant vacuum was presented in [Chap. 7](#). High fidelity multi-qubit entangled states can be prepared using the protocol. The suggested protocol was shown to be robust against experimental restrictions and non-idealities, and that the presented protocol can be performed with state-of-the-art circuit QED systems. An example realization using the tunable four-junction flux qubit was presented.

In [Chap. 8](#) a quantum-simulation scheme of non-perturbative cavity QED using trapped ions was suggested. By driving the harmonic modes of the trapped-ion crystal, interactions between qubits, and between qubits and a mode of the crystal,

can be engineered. It was shown that the general cavity QED Hamiltonian can be implemented in these systems. The available parameter regimes of the simulation in state-of-the-art trapped-ion systems were discussed and the main limitations were pinpointed. Possible experiments with the quantum simulator include using the scheme of [Chap. 7](#) to prepare the subradiant vacuum state and confirming the generated multi-qubit-entangled state with full-state tomography. The spectrum of the EDM could as well be probed in the ion system.

9.1 Outlook

In the future an interesting research direction would be to study how the single mode description we have presented arises from a more complicated situation where the TLSs are ultra-strongly coupled to multiple, possibly infinite number of modes. This regime has already received some attention, but mainly for single qubits coupled to a continuum of modes [42, 69, 178–182]. As we have shown the physics of multi-qubit systems can be very different, opening chances for exiting physics. This situation presents challenges both numerically and analytically. The fast growth of the size of the systems Hilbert space restricts the domain where brute force numerical simulations can be performed. Existing sophisticated numerical methods such as matrix product states (MPS) are limited to situations where the system is only weakly entangled, *a priori* not guaranteed in the USC regime. Also the long-range interacting nature of the EDM presents a challenge for MPS simulations which are more suited to simulate short-range interactions. Numerical techniques based on the polaron ansatz exist [183–185], but also these methods run into problems for $g/\omega_r \gtrsim 1$. Due to the numerical restrictions new analytical methods have to be developed that capture the important physical features of the multi-mode USC system in a simpler manner, enabling numerical simulations of manageable size.

Another direction would be to study the two-level-approximation in a multi-mode USC system. Results on the optimal gauge for the TLA exist only up to two coupled modes [110]. It would be interesting to expand the analysis to an arbitrary number of coupled modes. Also in this case exact numerical simulations will be limited to very small system sizes and analytical methods have to be developed.

In this thesis we have treated the dipole-dipole interactions always in the mean-field approximation. Including the exact DD interaction matrix opens up possibilities for new interesting physics. The complete 2^N -dimensional Hilbert space of the qubits has to be considered in this case, again creating challenges in numerical simulations. One interesting direction to take would be to look for quantum effects of the superradiant phase transition stemming from the DD interactions. This could be done, e.g., by studying the quantum Kibble-Zurek mechanism (QKZM)

[186–188]. By tuning the light-matter system across the SRPT and observing the rate of defect production, the dynamical scaling exponents of the transition can be obtained [189]. The scaling exponents determine if the phase transition is in the mean field class or not [189]. (For the Dicke model the SRPT is in the mean field class.)

Appendix A

Polaron transformation

In this appendix we present the *Polaron transformation* used frequently in the analysis of ultra-strongly coupled systems. It is a useful tool in context of the Dicke and Extended Dicke models. The aim of the transformation is to simplify the Hamiltonian so that it can be solved analytically at least quasixactly. This is achieved by eliminating the qubit-resonator coupling from the Hamiltonian.

We analyze the effect of the transformation on the most general Hamiltonian used in this thesis and give simplified results for the DM and EDM with the collective spin approximation. The starting Hamiltonian is the that of the Extended Dicke model with dipole-dipole interactions

$$H = \hbar\omega_r a^\dagger a + \hbar\omega_q S_z + \hbar g (a^\dagger + a) S_x + \frac{\hbar g^2}{\omega_r} S_x^2 + \frac{\hbar g^2}{4\omega_r} \sum_{i,j} D_{ij} \sigma_i^x \sigma_j^x, \quad (\text{A.1})$$

where S_α are the collective spin operators introduced in [Chap. 4](#). As stated above, our aim is to eliminate the qubit-oscillator coupling term $H_{\text{int}} \sim g (a^\dagger + a) S_x$. This can be achieved with the unitary transformation [\[50, 51\]](#)

$$\mathcal{U} = e^{\gamma(a^\dagger - a)S_x}, \quad (\text{A.2})$$

where $\gamma = g/\omega_r$.

The effect of the transformation on the operators a and a^\dagger can be calculated using the Baker–Campbell–Hausdorff formula

$$e^A B e^{-A} = B + [A, B] + \frac{1}{2!} [A, [A, B]] + \dots \quad (\text{A.3})$$

for exponential of operators. Since $[a, a^\dagger] = \mathbb{1}$ the above formula truncates after the first order. Thus, we obtain

$$\mathcal{U} a \mathcal{U}^\dagger = a + [\gamma (a^\dagger - a) S_x, a] = a - \gamma S_x, \quad (\text{A.4})$$

$$\mathcal{U} a^\dagger \mathcal{U}^\dagger = a^\dagger + [\gamma (a^\dagger - a) S_x, a^\dagger] = a^\dagger - \gamma S_x, \quad (\text{A.5})$$

i.e. the resonator field operators are displaced by an amount γS_x . Let us now move on to the qubit operators. Since $\mathcal{U} \propto S_x$ it commutes with S_x and by extension with all of the single qubit Pauli sigma- x operators, σ_i^x . The effect on the collective sigma- z operator S_z can be calculated by thinking of \mathcal{U} as a resonator dependent rotation of the qubit around the x -axis. The angle of rotation is given by $\theta = -i\gamma (a^\dagger - a)$ as can be seen by writing $\mathcal{U} = e^{i\theta S_x} = \mathcal{R}_x(\theta)$. The effect of this S_x rotation on S_z is given by

$$\mathcal{R}_x(\theta)S_z\mathcal{R}_x^\dagger(\theta) = \cos(\theta)S_z + \sin(\theta)S_y. \quad (\text{A.6})$$

Thus, the action of \mathcal{U} is

$$\begin{aligned} \mathcal{U}S_z\mathcal{U}^\dagger &= \cos(-i\gamma (a^\dagger - a))S_z + \sin(-i\gamma (a^\dagger - a))S_y \\ &= \cos(i\gamma (a^\dagger - a))S_z - \sin(i\gamma (a^\dagger - a))S_y. \end{aligned} \quad (\text{A.7})$$

Using $\cos(x) = (e^{ix} + e^{-ix})/2$ and $\sin(x) = -i(e^{ix} - e^{-ix})/2$, and defining the raising and lowering operators $\tilde{S}_\pm = S_z \pm iS_y$ with respect to S_x , we obtain

$$\begin{aligned} \mathcal{U}S_z\mathcal{U}^\dagger &= \frac{1}{4} \left(e^{-\gamma(a^\dagger - a)} + e^{\gamma(a^\dagger - a)} \right) \left(\tilde{S}_+ + \tilde{S}_- \right) + \frac{1}{4} \left(e^{-\gamma(a^\dagger - a)} - e^{\gamma(a^\dagger - a)} \right) \left(\tilde{S}_+ - \tilde{S}_- \right) \\ &= \frac{1}{2} \left(e^{-\gamma(a^\dagger - a)} \tilde{S}_+ + e^{\gamma(a^\dagger - a)} \tilde{S}_- \right) \\ &= \frac{1}{2} \left(\mathcal{D}(-\gamma) \tilde{S}_+ + \mathcal{D}(\gamma) \tilde{S}_- \right), \end{aligned} \quad (\text{A.8})$$

where we have introduced the displacement operator $\mathcal{D}(\alpha) = \exp(\alpha a^\dagger - \alpha^* a)$. In this frame the S_z term thus induces jumps between different S_x eigenstates and simultaneously displaces the resonator by γ .

It is now easy to see that we get a term from the free oscillator Hamiltonian that cancels the interaction Hamiltonian H_{int} , but we also get a term that is proportional to S_x^2 . Also transforming H_{int} gives that kind of term, but with a negative sign and factor of two in front. The result is to cancel the collective S_x^2 term in the EDM Hamiltonian. Putting everything together gives

$$\tilde{H} = \hbar\omega_r a^\dagger a + \frac{\hbar\omega_q}{2} \left(\mathcal{D}\left(-\frac{g}{\omega_r}\right) \tilde{S}_+ + \mathcal{D}\left(\frac{g}{\omega_r}\right) \tilde{S}_- \right) + \frac{\hbar g^2}{4\omega_r} \sum_{i,j} D_{ij} \sigma_i^x \sigma_j^x. \quad (\text{A.9})$$

The resulting Hamiltonian is diagonal in the S_x eigenbasis when neglecting the second term.

For the EDM with the collective spin approximation, i.e. $\sum_{i,j} D_{ij} \sigma_i^x \sigma_j^x / 4 \rightarrow \varepsilon S_x^2$ see [Sec. 4.3](#), we obtain

$$\tilde{H}_{\text{EDM}} = \hbar\omega_r a^\dagger a + \frac{\hbar\omega_q}{2} \left(\mathcal{D}\left(-\frac{g}{\omega_r}\right) \tilde{S}_+ + \mathcal{D}\left(\frac{g}{\omega_r}\right) \tilde{S}_- \right) + \varepsilon \frac{\hbar g^2}{\omega_r} S_x^2. \quad (\text{A.10})$$

In the special case of $\varepsilon = -1$, corresponding to the Dicke model see [Sec. 4.3](#), we get

$$\tilde{H}_{\text{DM}} = \hbar\omega_r a^\dagger a + \frac{\hbar\omega_q}{2} \left(\mathcal{D}\left(-\frac{g}{\omega_r}\right)\tilde{S}_+ + \mathcal{D}\left(\frac{g}{\omega_r}\right)\tilde{S}_- \right) - \frac{\hbar g^2}{\omega_r} S_x^2. \quad (\text{A.11})$$

Appendix B

Effective low energy theory for the USC regime

B.1 Effective Hamiltonian

In this appendix we give the details of the perturbative approach to obtain a low energy effective Hamiltonian for the Extended Dicke model. The starting point is the Hamiltonian in the polaron frame obtained through the polaron transformation of [App. A](#) (we set $\hbar = 1$ through out this appendix),

$$H = \omega_r a^\dagger a + \frac{g^2}{4\omega_r} \sum_{i,j} D_{ij} \sigma_i^x \sigma_j^x + \frac{\omega_q}{2} \left(\mathcal{D}\left(-\frac{g}{\omega_r}\right) \tilde{S}_+ + \mathcal{D}\left(\frac{g}{\omega_r}\right) \tilde{S}_- \right), \quad (\text{B.1})$$

where $\tilde{S}_\pm = S_z \pm iS_y$. We divide the Hamiltonian in two parts $H = H_0 + H_1$, where

$$H_0 = \omega_r a^\dagger a + \frac{g^2}{4\omega_r} \sum_{i,j} D_{ij} \sigma_i^x \sigma_j^x, \quad (\text{B.2})$$

$$H_1 = \frac{\omega_q}{2} \left(\mathcal{D}\left(-\frac{g}{\omega_r}\right) \tilde{S}_+ + \mathcal{D}\left(\frac{g}{\omega_r}\right) \tilde{S}_- \right). \quad (\text{B.3})$$

The first term is diagonal in the basis $|n, \{s_i\}\rangle$, where n is the photon number and the s_i , $s_i = \pm 1$, specifies the spin state. In the limit of $\omega_q \rightarrow 0$ these are the eigenstates of the system. The second term, H_1 , induces transitions between these states by flipping a spin, not a specific one but a superposition of all N possible flips, and at the same time displaces the resonator state by $\pm g/\omega_r$ depending on the direction. Note that in the original basis these states are given by

$$\Psi_{n, \{s_i\}} = \exp \left[-\frac{g}{\omega_r} (a^\dagger - a) S_x \right] |n, \{s_i\}\rangle. \quad (\text{B.4})$$

These states are displaced Fock-states where the amplitude of the displacement $\alpha = g/\omega_r \sum_i s_i$ depends on the total projection along x -direction.

Let us introduce the short-hand notation $\gamma = g/\omega_r$. We want to calculate the effective Hamiltonian for the systems low energy states in the limit $\omega_q/g \rightarrow 0$. Thus, we need to evaluate the perturbative corrections to the energies of eigenstates of H_0 coming from H_1 . In general this will be very difficult due to the presence of the dipole-dipole interactions and, thus, the dependence of the energy of the eigenstates on the spin state. Thus, we will restrict ourselves to the situation when these energy differences are negligible compared to the coupling induced between the states by H_1 . Neglecting the dipole-dipole coupling induced energy shifts makes all of the spin states degenerate and allows us to do the perturbation theory using the collective spin states $|s, m_x\rangle$. Thus, the states with the lowest energy are the ones with no photons and the spin state is arbitrary $\{|0, s, m_x\rangle\}_{s, m_x}$.

The direct coupling induced between the states in the lowest n -manifold by H_1 is given by

$$\langle 0, s', m'_x | H_1 | 0, s, m_x \rangle = \frac{\omega_q}{2} e^{-\gamma^2/2} \delta_{s, s'} \left(\tilde{S}_+^{m_x, m_x+1} \delta_{m'_x, m_x+1} + \tilde{S}_-^{m_x, m_x-1} \delta_{m'_x, m_x-1} \right), \quad (\text{B.5})$$

where $\tilde{S}_\pm^{m_x, m_x \pm 1} = \langle s, m_x \pm 1 | \tilde{S}_\pm | s, m_x \rangle = \sqrt{s(s+1) - m_x(m_x \pm 1)}$. Thus, the effective Hamiltonian at first order is

$$H_{\text{eff}}^{(1)} = \omega_q e^{-\gamma^2/2} S_z. \quad (\text{B.6})$$

We see that to first order the different m_x -states are coupled through the perturbation by the bare qubit Hamiltonian S_z , but the frequency of the qubits has been suppressed exponentially. The origin of this suppression is the photonic component of the spin eigenstates in the polaron frame. The coherent cloud of photons in the states reduces the overlap by a factor $\exp(-\gamma^2/2) = \langle 0, -\gamma | 0, \gamma \rangle$, where $|n, \alpha\rangle$ is a displaced Fock-state.

To obtain the second order correction we need to evaluate the effect of virtual transitions to higher n -manifolds and again back to the ground-state manifold. The perturbation H_1 can only change the m_x -state by ± 1 and leaves s untouched. The photonic component is displaced by $\pm\gamma$ and, thus, all photonic states $n \geq 1$ are coupled. Thus the needed corrections are given by

$$M(s, m_x, m'_x) = \sum_{n=1}^{\infty} \left[\frac{\langle 0, s, m'_x | H_1 | n, s, m_x + 1 \rangle \langle n, s, m_x + 1 | H_1 | 0, s, m_x \rangle}{E_{0, s, m_x} - E_{n, s, m'_x}} + \frac{\langle 0, s, m'_x | H_1 | n, s, m_x - 1 \rangle \langle n, s, m_x - 1 | H_1 | 0, s, m_x \rangle}{E_{0, s, m_x} - E_{n, s, m'_x}} \right]. \quad (\text{B.7})$$

Of these elements the only ones that can be non-zero are the ones where $m'_x = m_x$ or $m'_x = m_x \pm 2$. For both of the terms the denominator is given by $E_{0,s,m_x} - E_{n,s,m'_x} = -n\omega_r$.

Let us evaluate the diagonal term first

$$\begin{aligned} M(s, m_x, m_x) &= \sum_{n=1}^{\infty} \frac{\omega_q^2}{4} \left[\frac{(\tilde{S}_+^{m_x, m_x+1})^2 e^{-\gamma^2} (-\gamma)^{2n}}{-n\omega_r n!} + \frac{(\tilde{S}_-^{m_x, m_x-1})^2 e^{-\gamma^2} \gamma^{2n}}{-n\omega_r n!} \right] \\ &= -\frac{\omega_q^2}{2\omega_r} e^{-\gamma^2} [s(s+1) - m_x^2] \sum_{n=1}^{\infty} \frac{\gamma^{2n}}{n \times n!}. \end{aligned} \quad (\text{B.8})$$

The sum can be evaluated exactly to be

$$\sum_{n=1}^{\infty} \frac{\gamma^{2n}}{n \times n!} = \text{Ei}(\gamma^2) - 2 \log(\gamma) - \Gamma, \quad (\text{B.9})$$

where $\text{Ei}(x) = -\int_x^{\infty} e^{-t}/t dt$ is the exponential integral, $\log(x)$ is the natural logarithm and $\Gamma \approx 0.5772$ is the Euler-Mascheroni constant. For $\gamma \gtrsim 2$ it is approximately given by

$$\sum_{n=1}^{\infty} \frac{\gamma^{2n}}{n \times n!} \approx \frac{e^{\gamma^2}}{\gamma^2}, \quad (\text{B.10})$$

such that the diagonal term can be simplified, in this regime, to

$$M(s, m_x, m_x) = \frac{\omega_r \omega_q^2}{2g^2} [m_x^2 - s(s+1)]. \quad (\text{B.11})$$

This term is not exponentially suppressed like the first order coupling, thus, it is this second order term which will determine the ordering of the levels for large γ .

Next we evaluate the off-diagonal elements:

$$\begin{aligned} M(s, m_x, m_x \pm 2) &= \sum_{n=1}^{\infty} \frac{\omega_q e^{-\gamma^2} (-\gamma)^n \gamma^n \tilde{S}_-^{m_x \pm 2, m_x \pm 1} \tilde{S}_+^{m_x, m_x \pm 1}}{-4n\omega_r n!} \\ &= -\frac{\omega_q^2}{4\omega_r} e^{-\gamma^2} \tilde{S}_-^{m_x \pm 2, m_x \pm 1} \tilde{S}_+^{m_x, m_x \pm 1} \sum_{n=1}^{\infty} \frac{(-1)^n \gamma^{2n}}{n \times n!}. \end{aligned} \quad (\text{B.12})$$

Also the sum appearing above can be solved analytically

$$\sum_{n=1}^{\infty} \frac{(-1)^n \gamma^{2n}}{n \times n!} = \text{Ei}(-\gamma^2) - 2 \log(\gamma) - \Gamma, \quad (\text{B.13})$$

and for large γ it is approximately given by

$$\sum_{n=1}^{\infty} \frac{(-1)^n \gamma^{2n}}{n \times n!} \approx -2 \log(\gamma), \quad (\text{B.14})$$

so that the off-diagonal terms simplify to

$$M(s, m_x, m_x \pm 2) = \frac{\omega_q^2}{2\omega_r} e^{-\gamma^2} \log(\gamma) \tilde{S}_-^{m_x \pm 2, m_x \pm 1} \tilde{S}_+^{m_x, m_x \pm 1}. \quad (\text{B.15})$$

These off-diagonal elements are, again, exponentially suppressed in g compared to the diagonal terms. It is also exponentially smaller than the first order term such that we neglect it all together. Thus, the effective Hamiltonian at second order reads

$$H_{\text{eff}}^{(2)} = \frac{\omega_r \omega_q^2}{2g^2} (S_x^2 - \mathbf{S}^2), \quad (\text{B.16})$$

where $\mathbf{S}^2 = S_x^2 + S_y^2 + S_z^2$ is the square of the length of the collective spin \mathbf{S} .

The total effective Hamiltonian for the ground state $n = 0$ manifold is then

$$H_{\text{eff}} = \frac{\omega_r \omega_q^2}{2g^2} (S_x^2 - \mathbf{S}^2) + \frac{g^2}{4\omega_r} \sum_{i,j} D_{ij} \sigma_i^x \sigma_j^x + \omega_q e^{-\gamma^2/2} S_z, \quad (\text{B.17})$$

where we have reinserted the small dipole-dipole interactions.

B.2 Correction to the eigenstates

Not only the energies of the states get shifted also the eigenstates change due to the perturbation from H_1 :

$$|0, s, m_x\rangle \simeq |0, s, m_x\rangle^{(0)} + |0, s, m_x\rangle^{(1)}, \quad (\text{B.18})$$

where $|0, s, m_x\rangle^{(0)}$ are the unperturbed eigenstates introduced earlier. The first order correction is given by

$$\begin{aligned} |0, s, m_x\rangle^{(1)} &= \sum_{m'_x=-s}^s \sum_{n=1}^{\infty} \frac{\langle n, s, m'_x | H_1 | 0, s, m_x \rangle}{-n\omega_r} |n, s, m'_x\rangle \\ &= -\frac{\omega_q}{\omega_r} e^{\gamma^2/2} \sum_{n=1}^{\infty} \frac{\gamma^n}{n\sqrt{n!}} \left((-1)^n \tilde{S}_+^{m_x, m_x+1} |n, s, m_x+1\rangle \right. \\ &\quad \left. + \tilde{S}_-^{m_x, m_x-1} |n, s, m_x-1\rangle \right). \end{aligned} \quad (\text{B.19})$$

The states in the ground state manifold get some higher n manifold states mixed to them and also some character from the neighbouring $m_x \pm 1$ states. For most of the observables these corrections do not make a practical difference, but there are some exceptions. For example, the qubit polarization in the ground state is significantly modified due to the mixing [50]

$$\langle S_z \rangle_{\text{GS}} = \frac{2}{\omega_q} \langle 0, s, 0 | H_1 | 0, s, 0 \rangle \approx -s(s+1) \frac{\omega_q \omega_r}{g^2}, \quad (\text{B.20})$$

which would decay exponentially in g according to H_{eff} . In the above analysis we have again assumed the dipole-dipole energy to be negligible.

Appendix C

Master equation for ultra-strongly coupled systems

In this appendix we give the details of the derivation of the master equation used in [Chap. 7](#). The derivation presented is mainly based on [\[140\]](#). The environment is modelled in the standard way as a collection of harmonic oscillators, and the coupling between the bath and the system is assumed to be bilinear. The derivation is done for an almost generic system operator X with a Hamiltonian H_S . In [Chap. 7](#) the specific case of $X = a + a^\dagger$ and $H_S = H_{\text{EDM}}$ is used.

The system and the bath, under the rotating wave approximation of the interaction Hamiltonian, are described by the total Hamiltonian $H = H_S + H_B + H_{SB}$, where

$$H_S = \sum_n \hbar\omega_n |n\rangle \langle n|, \quad (\text{C.1})$$

$$H_B = \sum_k \hbar\omega_k b_k^\dagger b_k, \quad (\text{C.2})$$

$$H_{SB} = \sum_k \hbar g_k (b_k^\dagger X_+ + b_k X_-), \quad (\text{C.3})$$

and $X_{+(-)} = \sum_{n,m>(<)n} x_{nm} |n\rangle \langle m|$, $x_{nm} = \langle n| X |m\rangle$. The system Hamiltonian is expressed in the energy eigenbasis $\{|n\rangle\}_n$ with eigenfrequencies ω_n . The frequencies ω_k are the eigenfrequencies of the bath oscillators and $b^{(\dagger)}$ is the annihilation (creation) operator for mode k of the environment. We have assumed that the system operator that couples to the bath has only off-diagonal matrix elements (thus this treatment does not include pure dephasing).

The density operator for the whole system + environment ρ_{tot} satisfies the von

Neumann equation [30]

$$\frac{d\rho_{\text{tot}}}{dt} = -\frac{i}{\hbar}[H, \rho_{\text{tot}}(t)]. \quad (\text{C.4})$$

We move to an interaction picture with respect to the free Hamiltonians of the system and the bath, $H_S + H_B$. The von Neumann equation in this frame is given by

$$\frac{d\rho_I}{dt} = -\frac{i}{\hbar}[H_{SB}(t), \rho_I(t)], \quad (\text{C.5})$$

where the interaction picture system-bath coupling Hamiltonian is

$$H_{SB}(t) = \sum_k g_k \left(b_k^\dagger e^{i\omega_k t} X_+(t) + b_k e^{-i\omega_k t} X_-(t) \right), \quad (\text{C.6})$$

$$X_{+(-)}(t) = \sum_{n,m > (<) n} x_{nm} e^{i\Delta_{nm} t} |n\rangle \langle m|, \quad (\text{C.7})$$

and we have defined $\Delta_{nm} \equiv \omega_n - \omega_m$. The von Neumann equation can be integrated to [30]

$$\begin{aligned} \rho_I(t) = & \rho_I(0) - \frac{i}{\hbar} \int_0^t dt' [H_{SB}(t'), \rho_I(t')] \\ & - \frac{1}{\hbar^2} \int_0^t dt' \int_0^{t'} dt'' [H_{SB}(t'), [H_{SB}(t''), \rho_I(t'')]]. \end{aligned} \quad (\text{C.8})$$

We assume weak coupling to the reservoir so that we can use the Born approximation [30], and assume an uncorrelated system bath state $\rho_I(t) \approx \rho_{I,S}(t) \otimes \rho_B(0)$ for all times, where $\rho_B(0)$ is the equilibrium state of the bath. Taking a trace over the bath degrees of freedom gives

$$\begin{aligned} \rho_{I,S}(t) = & \rho_{I,S}(0) - \frac{i}{\hbar} \int_0^t dt' \text{Tr}_B ([H_{SB}(t'), \rho_{I,S}(0) \otimes \rho_B(0)]) \\ & - \frac{1}{\hbar^2} \int_0^t dt' \int_0^{t'} dt'' \text{Tr}_B ([H_{SB}(t'), [H_{SB}(t''), \rho_{I,S}(t'') \otimes \rho_B(0)]]). \end{aligned} \quad (\text{C.9})$$

The second term of the above equation gives

$$\text{Tr}_B ([H_{SB}(t'), \rho_{I,S}(0) \otimes \rho_B]) = \sum_k [X_+(t) \langle b_k^\dagger \rangle + X_-(t) \langle b_k \rangle, \rho_{I,S}(0)]. \quad (\text{C.10})$$

We assume, without loss of generality, that $\langle b_k^{(\dagger)} \rangle = \text{Tr}_B(\rho_B(0) b_k^{(\dagger)}) = 0$, which is mostly the case. A non-vanishing value is easily incorporated [30]. Thus, the first integral vanishes.

To continue we take a derivative of $\rho_{I,S}$ and obtain

$$\frac{d\rho_{I,S}}{dt} = -\frac{1}{\hbar^2} \int_0^t dt' \text{Tr}_B ([H_{SB}(t), [H_{SB}(t'), \rho_{I,S}(t') \otimes \rho_B(0)]]). \quad (\text{C.11})$$

Expanding the double commutator gives in total 16 terms, which contain autocorrelation functions of the environment. We take them to be

$$\langle b_k(t) b_k^\dagger(0) \rangle = (N_{\text{th}}(\omega) + 1) e^{-i\omega t} \delta(t), \quad (\text{C.12})$$

$$\langle b_k^\dagger(t) b_k(0) \rangle = N_{\text{th}}(\omega) e^{-i\omega t} \delta(t), \quad (\text{C.13})$$

and everything else vanishes, as is the case for a bath in a thermal equilibrium. Above $N_{\text{th}}(\omega) = (e^{\beta\hbar\omega} - 1)^{-1}$ is the thermal occupation of the environmental modes at frequency ω . Assuming a delta correlated bath allows us to approximately replace $\rho_{I,S}(t') \rightarrow \rho_{I,S}(t)$, making Eq. (C.11) time-local. This is the so called Markov approximation. Putting everything together and going back to the Schrödinger picture gives [140]

$$\begin{aligned} \frac{d\rho}{dt} = & -\frac{i}{\hbar} [H_S, \rho] + \sum_{n,m>n} \Gamma_{nm} N_{\text{th}}(\Delta_{mn}) \mathcal{D}[|m\rangle \langle n|] \rho(t) \\ & + \sum_{n,m>n} \Gamma_{nm} (1 + N_{\text{th}}(\Delta_{mn})) \mathcal{D}[|n\rangle \langle m|] \rho(t), \end{aligned} \quad (\text{C.14})$$

where $\mathcal{D}[O] = O\rho O^\dagger - \{O^\dagger O, \rho\}/2$. The decay constants are given by

$$\Gamma_{nm} = 2\pi d(\Delta_{mn}) g^2(\Delta_{mn}) |x_{mn}|^2, \quad (\text{C.15})$$

and we have taken a limit of a continuous bath with density of states $d(\omega)$. The coupling constant $g(\omega)$ also depends on the energy of the transition. For a one dimensional bath, such as a transmission line, we have $g^2(\omega) = \omega$ [190]. In addition to these bath dependent factors the relaxation rate for a transition also depends on the matrix element of the coupling operator between the eigenstates in question $x_{mn} = \langle m| X |n\rangle$.

The form of the USC master equation has a simple interpretation. The dissipators in the eigenbasis are given by the negative and positive frequency components of the operator X coupling to the environment. Consider for example the situation where the resonator mode in the Extended Dicke model is coupled inductively to a transmission line. Then we would have $X = a + a^\dagger$. Using just the standard dissipators a and a^\dagger would not result in the system relaxing towards its ground state [140]. Instead taking the positive and negative frequency components results in the correct behaviour.

C.1 Simulation of the master equation with time-dependent couplings

In [Chap. 7](#) the qubit frequency and the coupling of the qubits to the resonator mode were taken to be time-dependent. This introduces additional complexity to the simulation. The master equation of [Eq. \(C.14\)](#) is not adequate because the basis $\{|n\rangle\}_n = \{|n(t)\rangle_n$ of the EDM is in this situation time-dependent. In order to use the eigenbasis of the EDM, [Eq. \(C.14\)](#) needs to be complemented with terms $\propto \langle n(t)|\dot{n}(t)\rangle$, where the dot denotes the time derivative. We, however, take a complementary approach.

In order to accommodate for the changing qubit frequency and coupling, we diagonalize the EDM Hamiltonian for every time step and construct the correct jump operators, X_{\pm} , as explained above. Then these operators are transformed back to the time-independent uncoupled basis, $|k, s, m_z\rangle$, spanned by the Fock states $|k\rangle$ and the collective spin states $|s, m_z\rangle$. This is done with a time-dependent unitary transformation

$$\mathcal{U}(t) = \sum_{n,k,m_z} |k, s, m_z\rangle \langle n(t)|. \quad (\text{C.16})$$

In the uncoupled basis no additional terms $\propto \langle n(t)|\dot{n}(t)\rangle$ are needed, in the expense of the jump operators becoming very complicated, inducing transitions between multiple basis states $|k, s, m_z\rangle$. The master equation is simulated using the solver provided in the quantum optics package `QuantumOptics.jl` [\[191\]](#) for the julia programming language.

Bibliography

- [1] A. Einstein, Über einen die erzeugung und verwandlung des liches betreffenden heuristischen gesichtspunkt, *Ann. Phys. (Berl.)* **322**, 132–148 (1905).
- [2] P. A. M. Dirac and N. H. D. Bohr, The quantum theory of the emission and absorption of radiation, *Proc. Royal Soc. Lond. Ser. A* **114**, 243–265 (1927).
- [3] V. Weisskopf, Probleme der neueren quantentheorie des elektrons, *Naturwissenschaften* **23**, 631–637 (1935).
- [4] W. E. Lamb and R. C. Retherford, Fine structure of the hydrogen atom by a microwave method, *Phys. Rev.* **72**, 241–243 (1947).
- [5] E. M. Purcell, Proceedings of the american physical society, *Phys. Rev.* **69**, 674–674 (1946).
- [6] E. M. Purcell, “Spontaneous emission probabilities at radio frequencies”, in *Confined electrons and photons: new physics and applications*, edited by E. Burstein and C. Weisbuch (Springer US, Boston, MA, 1995), pp. 839–839.
- [7] S. Haroche and J.-M. Raimond, *Exploring the quantum: atoms, cavities, and photons* (Oxford university press, 2006).
- [8] D. S. Dovzhenko et al., Light–matter interaction in the strong coupling regime: configurations, conditions, and applications, *Nanoscale* **10**, 3589–3605 (2018).
- [9] Y. Kaluzny et al., Observation of self-induced rabi oscillations in two-level atoms excited inside a resonant cavity: the ringing regime of superradiance, *Phys. Rev. Lett.* **51**, 1175–1178 (1983).
- [10] G. Rempe, H. Walther, and N. Klein, Observation of quantum collapse and revival in a one-atom maser, *Phys. Rev. Lett.* **58**, 353–356 (1987).
- [11] R. J. Thompson, G. Rempe, and H. J. Kimble, Observation of normal-mode splitting for an atom in an optical cavity, *Phys. Rev. Lett.* **68**, 1132–1135 (1992).

- [12] C. Weisbuch et al., Observation of the coupled exciton-photon mode splitting in a semiconductor quantum microcavity, *Phys. Rev. Lett.* **69**, 3314–3317 (1992).
- [13] P. A. Hobson et al., Strong exciton–photon coupling in a low-q all-metal mirror microcavity, *Appl. Phys. Lett.* **81**, 3519–3521 (2002).
- [14] R. Houdré et al., Room-temperature cavity polaritons in a semiconductor microcavity, *Phys. Rev. B* **49**, 16761–16764 (1994).
- [15] T. Yoshie et al., Vacuum rabi splitting with a single quantum dot in a photonic crystal nanocavity, *Nature* **432**, 200–203 (2004).
- [16] I. Chiorescu et al., Coherent dynamics of a flux qubit coupled to a harmonic oscillator, *Nature* **431**, 159–162 (2004).
- [17] A. Wallraff et al., Strong coupling of a single photon to a superconducting qubit using circuit quantum electrodynamics, *Nature* **431**, 162 (2004).
- [18] J. P. Reithmaier et al., Strong coupling in a single quantum dot-semiconductor microcavity system, *Nature* **432**, 197–200 (2004).
- [19] Y. Sugawara et al., Strong coupling between localized plasmons and organic excitons in metal nanovoids, *Phys. Rev. Lett.* **97**, 266808 (2006).
- [20] A. E. Schlather et al., Near-field mediated plexcitonic coupling and giant rabi splitting in individual metallic dimers, *Nano Lett.* **13**, 3281–3286 (2013).
- [21] A. Shalabney et al., Coherent coupling of molecular resonators with a microcavity mode, *Nat. Commun.* **6**, Article, 5981 (2015).
- [22] T. Sleator and H. Weinfurter, Realizable universal quantum logic gates, *Phys. Rev. Lett.* **74**, 4087–4090 (1995).
- [23] S.-B. Zheng and G.-C. Guo, Efficient scheme for two-atom entanglement and quantum information processing in cavity qed, *Phys. Rev. Lett.* **85**, 2392–2395 (2000).
- [24] T. Pellizzari et al., Decoherence, continuous observation, and quantum computing: a cavity qed model, *Phys. Rev. Lett.* **75**, 3788–3791 (1995).
- [25] A. Blais et al., Cavity quantum electrodynamics for superconducting electrical circuits: an architecture for quantum computation, *Phys. Rev. A* **69**, 062320 (2004).
- [26] J. Q. You and F. Nori, Superconducting circuits and quantum information, *Phys. Today* **58**, 42–47 (2005).
- [27] J. Clarke and F. K. Wilhelm, Superconducting quantum bits, *Nature* **453**, 1031 (2008).

- [28] M. Devoret, S. Girvin, and R. Schoelkopf, Circuit-qed: how strong can the coupling between a josephson junction atom and a transmission line resonator be?, *Ann. Phys.* **16**, 767–779 (2007).
- [29] J. J. Hopfield, Theory of the contribution of excitons to the complex dielectric constant of crystals, *Phys. Rev.* **112**, 1555–1567 (1958).
- [30] D. F. Walls and G. J. Milburn, *Quantum optics* (Springer Science & Business Media, 2007).
- [31] J. Koch et al., Charge-insensitive qubit design derived from the cooper pair box, *Phys. Rev. A* **76**, 042319 (2007).
- [32] V. E. Manucharyan et al., Fluxonium: single cooper-pair circuit free of charge offsets, *Science* **326**, 113–116 (2009).
- [33] F. Yan et al., The flux qubit revisited to enhance coherence and reproducibility, *Nat. Commun.* **7**, 12964 (2016).
- [34] Y. Qiu et al., Four-junction superconducting circuit, *Sci. Rep.* **6**, Article, 28622 (2016).
- [35] P. Forn-Díaz et al., Ultrastrong coupling regimes of light-matter interaction, *Rev. Mod. Phys.* **91**, 025005 (2019).
- [36] A. F. Kockum et al., Ultrastrong coupling between light and matter, *Nat. Rev. Phys.* **1**, 19–40 (2019).
- [37] A. A. Anappara et al., Signatures of the ultrastrong light-matter coupling regime, *Phys. Rev. B* **79**, 201303 (2009).
- [38] T. Niemczyk et al., Circuit quantum electrodynamics in the ultrastrong-coupling regime, *Nat. Phys.* **6**, 772 (2010).
- [39] P. Forn-Díaz et al., Observation of the bloch-siegert shift in a qubit-oscillator system in the ultrastrong coupling regime, *Phys. Rev. Lett.* **105**, 237001 (2010).
- [40] J. Casanova et al., Deep strong coupling regime of the jaynes-cummings model, *Phys. Rev. Lett.* **105**, 263603 (2010).
- [41] F. Yoshihara et al., Superconducting qubit-oscillator circuit beyond the ultrastrong-coupling regime, *Nat. Phys.* **13**, 44 (2016).
- [42] P. Forn-Díaz et al., Ultrastrong coupling of a single artificial atom to an electromagnetic continuum in the nonperturbative regime, *Nat. Phys.* **13**, 39 (2016).
- [43] A. Bayer et al., Terahertz light-matter interaction beyond unity coupling strength, *Nano Lett.* **17**, 6340–6344 (2017).

- [44] C. Ciuti, G. Bastard, and I. Carusotto, Quantum vacuum properties of the intersubband cavity polariton field, *Phys. Rev. B* **72**, 115303 (2005).
- [45] S. Ashhab and F. Nori, Qubit-oscillator systems in the ultrastrong-coupling regime and their potential for preparing nonclassical states, *Phys. Rev. A* **81**, 042311 (2010).
- [46] P. Nataf and C. Ciuti, Vacuum degeneracy of a circuit qed system in the ultrastrong coupling regime, *Phys. Rev. Lett.* **104**, 023601 (2010).
- [47] Y. K. Wang and F. T. Hioe, Phase transition in the dicke model of super-radiance, *Phys. Rev. A* **7**, 831–836 (1973).
- [48] K. Hepp and E. H. Lieb, On the superradiant phase transition for molecules in a quantized radiation field: the dicke maser model, *Ann. Phys.* **76**, 360–404 (1973).
- [49] S. De Liberato, Light-matter decoupling in the deep strong coupling regime: the breakdown of the purcell effect, *Phys. Rev. Lett.* **112**, 016401 (2014).
- [50] T. Jaako et al., Ultrastrong-coupling phenomena beyond the dicke model, *Phys. Rev. A* **94**, 033850 (2016).
- [51] D. De Bernardis, T. Jaako, and P. Rabl, Cavity quantum electrodynamics in the nonperturbative regime, *Phys. Rev. A* **97**, 043820 (2018).
- [52] P. Nataf and C. Ciuti, Protected quantum computation with multiple resonators in ultrastrong coupling circuit qed, *Phys. Rev. Lett.* **107**, 190402 (2011).
- [53] Y. Wang et al., Holonomic quantum computation in the ultrastrong-coupling regime of circuit qed, *Phys. Rev. A* **94**, 012328 (2016).
- [54] Y. Wang et al., Ultrafast quantum computation in ultrastrongly coupled circuit qed systems, *Sci. Rep.* **7**, Article, 44251 (2017).
- [55] G. Romero et al., Ultrafast quantum gates in circuit qed, *Phys. Rev. Lett.* **108**, 120501 (2012).
- [56] T. H. Kyaw et al., Scalable quantum memory in the ultrastrong coupling regime, *Sci. Rep.* **5**, Article, 8621 (2015).
- [57] R. Stassi and F. Nori, Long-lasting quantum memories: extending the coherence time of superconducting artificial atoms in the ultrastrong-coupling regime, *Phys. Rev. A* **97**, 033823 (2018).
- [58] F. Armata et al., Harvesting multiqubit entanglement from ultrastrong interactions in circuit quantum electrodynamics, *Phys. Rev. Lett.* **119**, 183602 (2017).

- [59] K. Rzażewski, K. Wódkiewicz, and W. Żakowicz, Phase transitions, two-level atoms, and the A^2 term, *Phys. Rev. Lett.* **35**, 432–434 (1975).
- [60] J. M. Knight, Y. Aharonov, and G. T. C. Hsieh, Are super-radiant phase transitions possible?, *Phys. Rev. A* **17**, 1454–1462 (1978).
- [61] J. Keeling, Coulomb interactions, gauge invariance, and phase transitions of the dicke model, *J. Phys. Condens. Matter* **19**, 295213 (2007).
- [62] A. Vukics and P. Domokos, Adequacy of the dicke model in cavity qed: a counter-no-go statement, *Phys. Rev. A* **86**, 053807 (2012).
- [63] A. Vukics, T. Grieser, and P. Domokos, Elimination of the a -square problem from cavity qed, *Phys. Rev. Lett.* **112**, 073601 (2014).
- [64] A. Vukics, T. Grieser, and P. Domokos, Fundamental limitation of ultra-strong coupling between light and atoms, *Phys. Rev. A* **92**, 043835 (2015).
- [65] P. Nataf and C. Ciuti, No-go theorem for superradiant quantum phase transitions in cavity qed and counter-example in circuit qed, *Nat. Commun.* **1**, Article, 72 (2010).
- [66] O. Viehmann, J. von Delft, and F. Marquardt, Superradiant phase transitions and the standard description of circuit qed, *Phys. Rev. Lett.* **107**, 113602 (2011).
- [67] T. P. Orlando et al., Superconducting persistent-current qubit, *Phys. Rev. B* **60**, 15398–15413 (1999).
- [68] S. J. Bosman et al., Approaching ultrastrong coupling in transmon circuit qed using a high-impedance resonator, *Phys. Rev. B* **95**, 224515 (2017).
- [69] S. J. Bosman et al., Multi-mode ultra-strong coupling in circuit quantum electrodynamics, *npj Quantum Inf.* **3**, 46 (2017).
- [70] D. De Bernardis et al., Breakdown of gauge invariance in ultrastrong-coupling cavity qed, *Phys. Rev. A* **98**, 053819 (2018).
- [71] J. Bourassa et al., Ultrastrong coupling regime of cavity qed with phase-biased flux qubits, *Phys. Rev. A* **80**, 032109 (2009).
- [72] M. Tinkham, *Introduction to superconductivity* (Courier Corporation, 2004).
- [73] S. Girvin, *Circuit qed: superconducting qubits coupled to microwave photons. in quantum machines: measurement and control of engineered quantum systems: lecture notes of the les houches summer school: volume 96, july 2011.* (Oxford University Press, 2014).
- [74] J. Bardeen, L. N. Cooper, and J. R. Schrieffer, Microscopic theory of superconductivity, *Phys. Rev.* **106**, 162–164 (1957).

- [75] J. Bardeen, L. N. Cooper, and J. R. Schrieffer, Theory of superconductivity, *Phys. Rev.* **108**, 1175–1204 (1957).
- [76] V. L. Ginzburg and L. D. Landau, On the theory of superconductivity, *Zh. Eksp. Teor. Fiz.* **20**, 1064–1082 (1950).
- [77] V. L. Ginzburg and L. D. Landau, “On the theory of superconductivity”, in *On superconductivity and superfluidity: a scientific autobiography* (Springer Berlin Heidelberg, Berlin, Heidelberg, 2009), pp. 113–137.
- [78] F. London and H. London, The electromagnetic equations of the supraconductor, *Proc. Royal Soc. Lond. Ser. A* **149**, 71–88 (1935).
- [79] W. Meissner and R. Ochsenfeld, Ein neuer effekt bei eintritt der supraleitfähigkeit, *Naturwissenschaften* **21**, 787–788 (1933).
- [80] H. Kamerlingh Onnes, Leiden comm, *120b, 122b, 124c* (1911).
- [81] B. Josephson, Possible new effects in superconductive tunnelling, *Phys. Lett.* **1**, 251–253 (1962).
- [82] P. W. Anderson and J. M. Rowell, Probable observation of the josephson superconducting tunneling effect, *Phys. Rev. Lett.* **10**, 230–232 (1963).
- [83] A. F. Andreev, The thermal conductivity of the intermediate state in superconductors, *Sov. Phys. JETP.* **46**, 1823–1828 (1964).
- [84] W. Ashcroft N and N. D. Mermin, *Solid state physics* (1976).
- [85] U. Vool and M. Devoret, Introduction to quantum electromagnetic circuits, *Int. J. Circ. Theor. Appl.* **45**, 897–934 (2017).
- [86] V. Bouchiat et al., Quantum coherence with a single cooper pair, *Phys. Scr.* **1998**, 165 (1998).
- [87] N. A. Masluk et al., Microwave characterization of josephson junction arrays: implementing a low loss superinductance, *Phys. Rev. Lett.* **109**, 137002 (2012).
- [88] I. V. Pechenezhskiy et al., Quantum dynamics of quasicharge in an ultrahigh-impedance superconducting circuit, *1907.02937* (2019).
- [89] I. I. Rabi, On the process of space quantization, *Phys. Rev.* **49**, 324–328 (1936).
- [90] I. I. Rabi, Space quantization in a gyrating magnetic field, *Phys. Rev.* **51**, 652–654 (1937).
- [91] E. T. Jaynes and F. W. Cummings, Comparison of quantum and semiclassical radiation theories with application to the beam maser, *Proc. IEEE* **51**, 89–109 (1963).

- [92] D. Braak, Integrability of the rabi model, *Phys. Rev. Lett.* **107**, 100401 (2011).
- [93] R. H. Dicke, Coherence in spontaneous radiation processes, *Phys. Rev.* **93**, 99–110 (1954).
- [94] G. Feher et al., Spontaneous emission of radiation from an electron spin system, *Phys. Rev.* **109**, 221–222 (1958).
- [95] J. M. Raimond et al., Statistics of millimeter-wave photons emitted by a rydberg-atom maser: an experimental study of fluctuations in single-mode superradiance, *Phys. Rev. Lett.* **49**, 1924–1927 (1982).
- [96] M. Tavis and F. W. Cummings, Exact solution for an n -molecule—radiation-field hamiltonian, *Phys. Rev.* **170**, 379–384 (1968).
- [97] J. Larson and E. K. Irish, Some remarks on ‘superradiant’ phase transitions in light-matter systems, *J. Phys. A: Math. Theor.* **50**, 174002 (2017).
- [98] K. Baumann et al., Dicke quantum phase transition with a superfluid gas in an optical cavity, *Nature* **464**, Article, 1301 (2010).
- [99] K. Baumann et al., Exploring symmetry breaking at the dicke quantum phase transition, *Phys. Rev. Lett.* **107**, 140402 (2011).
- [100] Z. Zhang et al., Nonequilibrium phase transition in a spin-1 dicke model, *Optica* **4**, 424–429 (2017).
- [101] Z. Zhang et al., Dicke-model simulation via cavity-assisted raman transitions, *Phys. Rev. A* **97**, 043858 (2018).
- [102] N. N. Bogoljubov, On a new method in the theory of superconductivity, *Il Nuovo Cimento (1955-1965)* **7**, 794–805 (1958).
- [103] C. Emary and T. Brandes, Chaos and the quantum phase transition in the dicke model, *Phys. Rev. E* **67**, 066203 (2003).
- [104] M. Bamba, K. Inomata, and Y. Nakamura, Superradiant phase transition in a superconducting circuit in thermal equilibrium, *Phys. Rev. Lett.* **117**, 173601 (2016).
- [105] J. D. Jackson, *Classical electrodynamics* (Wiley New York, 1998).
- [106] C. Cohen-Tannoudji, J. Dupont-Roc, and G. Grynberg, *Photons & atoms: introduction to quantum electrodynamics* (Wiley New York, 1997).
- [107] I. Chiorescu et al., Coherent quantum dynamics of a superconducting flux qubit, *Science* **299**, 1869–1871 (2003).
- [108] O. Di Stefano et al., Resolution of gauge ambiguities in ultrastrong-coupling cavity quantum electrodynamics, *Nat. Phys.* (2019).

- [109] A. Stokes and A. Nazir, Gauge ambiguities imply jaynes-cummings physics remains valid in ultrastrong coupling qed, *Nat. Commun.* **10**, 499 (2019).
- [110] M. Roth, F. Hassler, and D. P. DiVincenzo, Optimal gauge for the multi-mode rabi model in circuit qed, (2019).
- [111] T. Holstein and H. Primakoff, Field dependence of the intrinsic domain magnetization of a ferromagnet, *Phys. Rev.* **58**, 1098–1113 (1940).
- [112] D. F. Walls and G. J. Milburn, *Quantum optics* (Springer Science & Business Media, 2007).
- [113] H. J. Lipkin, N. Meshkov, and A. Glick, Validity of many-body approximation methods for a solvable model:(i). exact solutions and perturbation theory, *Nucl. Phys.* **62**, 188–198 (1965).
- [114] R. Graham and M. Höhnerbach, Two-state system coupled to a boson mode: quantum dynamics and classical approximations, *Z. Phys. B* **57**, 233–248 (1984).
- [115] M. D. Crisp, Application of the displaced oscillator basis in quantum optics, *Phys. Rev. A* **46**, 4138–4149 (1992).
- [116] G. Liberti et al., Entanglement of a qubit coupled to a resonator in the adiabatic regime, *Phys. Rev. A* **73**, 032346 (2006).
- [117] G. Liberti, F. Plastina, and F. Piperno, Scaling behavior of the adiabatic dicke model, *Phys. Rev. A* **74**, 022324 (2006).
- [118] S. Ashhab, Superradiance transition in a system with a single qubit and a single oscillator, *Phys. Rev. A* **87**, 013826 (2013).
- [119] L. Bakemeier, A. Alvermann, and H. Fehske, Quantum phase transition in the dicke model with critical and noncritical entanglement, *Phys. Rev. A* **85**, 043821 (2012).
- [120] M.-J. Hwang, R. Puebla, and M. B. Plenio, Quantum phase transition and universal dynamics in the rabi model, *Phys. Rev. Lett.* **115**, 180404 (2015).
- [121] R. Puebla, M.-J. Hwang, and M. B. Plenio, Excited-state quantum phase transition in the rabi model, *Phys. Rev. A* **94**, 023835 (2016).
- [122] M.-J. Hwang, P. Rabl, and M. B. Plenio, Dissipative phase transition in the open quantum rabi model, *Phys. Rev. A* **97**, 013825 (2018).
- [123] B. L. T. Plourde et al., Entangling flux qubits with a bipolar dynamic inductance, *Phys. Rev. B* **70**, 140501 (2004).
- [124] M. Born and R. Oppenheimer, Zur quantentheorie der molekeln, *Ann. Phys. (Berl.)* **389**, 457–484 (1927).

- [125] A. Garg, Tunnel splittings for one-dimensional potential wells revisited, *Am. J. Phys.* **68**, 430–437 (2000).
- [126] M. Vranicar and M. Robnik, Accuracy of the wkb approximation: the case of general quartic potential, *Prog. Theor. Phys. Suppl.* **139**, 214–233 (2000).
- [127] T. Jaako, J. J. García-Ripoll, and P. Rabl, Ultrastrong-coupling circuit qed in the radio-frequency regime, *Phys. Rev. A* **100**, 043815 (2019).
- [128] M. F. Gely et al., Observation and stabilization of photonic fock states in a hot radio-frequency resonator, *Science* **363**, 1072–1075 (2019).
- [129] B. H. Bransden, C. J. Joachain, and T. J. Plivier, *Physics of atoms and molecules* (Pearson Education India, 2003).
- [130] C. Caloz, A. Sanada, and T. Itoh, A novel composite right-/left-handed coupled-line directional coupler with arbitrary coupling level and broad bandwidth, *IEEE Trans. Microw. Theory Tech.* **52**, 980–992 (2004).
- [131] P. Macha et al., Implementation of a quantum metamaterial using superconducting qubits, *Nat. Commun.* **5**, Article, 5146 (2014).
- [132] M. J. Schwarz et al., Gradiometric flux qubits with a tunable gap, *New J. Phys.* **15**, 045001 (2013).
- [133] F. Deppe et al., Two-photon probe of the jaynes-cummings model and controlled symmetry breaking in circuit qed, *Nat. Phys.* **4**, 686 (2008).
- [134] J. M. Fink et al., Quantum electromechanics on silicon nitride nanomembranes, *Nat. Commun.* **7**, 12396 (2016).
- [135] S. Barzanjeh et al., Mechanical on-chip microwave circulator, *Nat. Commun.* **8**, 953 (2017).
- [136] S. Barzanjeh et al., Stationary entangled radiation from micromechanical motion, *Nature* **570**, 480–483 (2019).
- [137] L. McKenzie-Sell et al., Low-impedance superconducting microwave resonators for strong coupling to small magnetic mode volumes, *Phys. Rev. B* **99**, 140414 (2019).
- [138] M. Born and V. Fock, Beweis des adiabatenatzes, *Z. Phys.* **51**, 165–180 (1928).
- [139] C. M. Wilson et al., Observation of the dynamical casimir effect in a superconducting circuit, *Nature* **479**, 376 (2011).
- [140] F. Beaudoin, J. M. Gambetta, and A. Blais, Dissipation and ultrastrong coupling in circuit qed, *Phys. Rev. A* **84**, 043832 (2011).
- [141] M. Yu, Computable and uncomputable, *Sovetskoye Radio, Moscow* (1980).

- [142] R. P. Feynman, Simulating physics with computers, *Int. J. Theor. Phys.* **21**, 467–488 (1982).
- [143] D. Leibfried et al., Quantum dynamics of single trapped ions, *Rev. Mod. Phys.* **75**, 281–324 (2003).
- [144] R. Blatt and C. F. Roos, Quantum simulations with trapped ions, *Nat. Phys.* **8**, Review Article, 277 (2012).
- [145] M. Johanning, A. F. Varón, and C. Wunderlich, Quantum simulations with cold trapped ions, *J. Phys. B* **42**, 154009 (2009).
- [146] B. P. Lanyon et al., Universal digital quantum simulation with trapped ions, *Science* **334**, 57–61 (2011).
- [147] J. S. Pedernales et al., Quantum rabi model with trapped ions, *Sci. Rep.* **5**, Article, 15472 (2015).
- [148] D. Lv et al., Quantum simulation of the quantum rabi model in a trapped ion, *Phys. Rev. X* **8**, 021027 (2018).
- [149] A. Safavi-Naini et al., Exploring adiabatic quantum dynamics of the dicke model in a trapped ion quantum simulator, (2017).
- [150] A. Safavi-Naini et al., Verification of a many-ion simulator of the dicke model through slow quenches across a phase transition, *Phys. Rev. Lett.* **121**, 040503 (2018).
- [151] J. Cohn et al., Bang-bang shortcut to adiabaticity in the dicke model as realized in a penning trap experiment, *New Journal of Physics* **20**, 055013 (2018).
- [152] N. K. Langford et al., Experimentally simulating the dynamics of quantum light and matter at deep-strong coupling, *Nat. Commun.* **8**, 1715 (2017).
- [153] F. Dimer et al., Proposed realization of the dicke-model quantum phase transition in an optical cavity qed system, *Phys. Rev. A* **75**, 013804 (2007).
- [154] P. Schneeweiss, A. Dureau, and C. Sayrin, Cold-atom-based implementation of the quantum rabi model, *Phys. Rev. A* **98**, 021801 (2018).
- [155] S.-L. Zhu, C. Monroe, and L.-M. Duan, Arbitrary-speed quantum gates within large ion crystals through minimum control of laser beams, *EPL* **73**, 485–491 (2006).
- [156] K. Kim et al., Quantum simulation of the transverse ising model with trapped ions, *New J. Phys.* **13**, 105003 (2011).
- [157] P. Jurcevic et al., Spectroscopy of interacting quasiparticles in trapped ions, *Phys. Rev. Lett.* **115**, 100501 (2015).

- [158] D. Porras and J. I. Cirac, Effective quantum spin systems with trapped ions, *Phys. Rev. Lett.* **92**, 207901 (2004).
- [159] A. Friedenauer et al., Simulating a quantum magnet with trapped ions, *Nature Physics* **4**, 757–761 (2008).
- [160] K. Kim et al., Entanglement and tunable spin-spin couplings between trapped ions using multiple transverse modes, *Phys. Rev. Lett.* **103**, 120502 (2009).
- [161] G.-D. Lin, C. Monroe, and L.-M. Duan, Sharp phase transitions in a small frustrated network of trapped ion spins, *Phys. Rev. Lett.* **106**, 230402 (2011).
- [162] R. Islam et al., Onset of a quantum phase transition with a trapped ion quantum simulator, *Nature Communications* **2**, 377 (2011).
- [163] D. Dylewsky et al., Nonperturbative calculation of phonon effects on spin squeezing, *Phys. Rev. A* **93**, 013415 (2016).
- [164] C. Schneider, D. Porras, and T. Schaetz, Experimental quantum simulations of many-body physics with trapped ions, *Rep. Prog. Phys.* **75**, 024401 (2012).
- [165] A. Dutta and J. K. Bhattacharjee, Phase transitions in the quantum ising and rotor models with a long-range interaction, *Phys. Rev. B* **64**, 184106 (2001).
- [166] P. Jurcevic et al., Direct observation of dynamical quantum phase transitions in an interacting many-body system, *Phys. Rev. Lett.* **119**, 080501 (2017).
- [167] P. Jurcevic et al., Quasiparticle engineering and entanglement propagation in a quantum many-body system, *Nature* **511**, 202 (2014).
- [168] J. J. García-Ripoll, P. Zoller, and J. I. Cirac, Coherent control of trapped ions using off-resonant lasers, *Phys. Rev. A* **71**, 062309 (2005).
- [169] Y. H. Teoh et al., Machine learning design of a trapped-ion quantum spin simulator, *1910.02496* (2019).
- [170] L. Viola and S. Lloyd, Dynamical suppression of decoherence in two-state quantum systems, *Phys. Rev. A* **58**, 2733–2744 (1998).
- [171] S. Balasubramanian et al., Bang-bang shortcut to adiabaticity in trapped-ion quantum simulators, *Phys. Rev. A* **97**, 022313 (2018).
- [172] Y. Todorov and C. Sirtori, Intersubband polaritons in the electrical dipole gauge, *Phys. Rev. B* **85**, 045304 (2012).
- [173] Y. Todorov et al., Ultrastrong light-matter coupling regime with polariton dots, *Phys. Rev. Lett.* **105**, 196402 (2010).

- [174] C. Maissen et al., Ultrastrong coupling in the near field of complementary split-ring resonators, *Phys. Rev. B* **90**, 205309 (2014).
- [175] Q. Zhang et al., Collective non-perturbative coupling of 2d electrons with high-quality-factor terahertz cavity photons, *Nat. Phys.* **12**, 1005 (2016).
- [176] Y. Todorov and C. Sirtori, Few-electron ultrastrong light-matter coupling in a quantum lc circuit, *Phys. Rev. X* **4**, 041031 (2014).
- [177] D. Jaschke et al., Critical phenomena and kibble–zurek scaling in the long-range quantum ising chain, *New Journal of Physics* **19**, 033032 (2017).
- [178] A. J. Leggett et al., Dynamics of the dissipative two-state system, *Rev. Mod. Phys.* **59**, 1–85 (1987).
- [179] B. Peropadre et al., Nonequilibrium and nonperturbative dynamics of ultrastrong coupling in open lines, *Phys. Rev. Lett.* **111**, 243602 (2013).
- [180] E. Sanchez-Burillo et al., Scattering in the ultrastrong regime: nonlinear optics with one photon, *Phys. Rev. Lett.* **113**, 263604 (2014).
- [181] C. Sánchez Muñoz, F. Nori, and S. De Liberato, Resolution of superluminal signalling in non-perturbative cavity quantum electrodynamics, *Nature Communications* **9**, 1924 (2018).
- [182] E. Sánchez-Burillo et al., Single photons by quenching the vacuum, *Phys. Rev. Lett.* **123**, 013601 (2019).
- [183] G. Díaz-Camacho, A. Bermudez, and J. J. García-Ripoll, Dynamical polaron ansatz: a theoretical tool for the ultrastrong-coupling regime of circuit qed, *Phys. Rev. A* **93**, 043843 (2016).
- [184] T. Shi, Y. Chang, and J. J. García-Ripoll, Ultrastrong coupling few-photon scattering theory, *Phys. Rev. Lett.* **120**, 153602 (2018).
- [185] V. Paulisch, T. Shi, and J. J. Garcia-Ripoll, Two-photon scattering in usc regime, *1810.08439* (2018).
- [186] W. H. Zurek, U. Dorner, and P. Zoller, Dynamics of a quantum phase transition, *Phys. Rev. Lett.* **95**, 105701 (2005).
- [187] A. Polkovnikov, Universal adiabatic dynamics in the vicinity of a quantum critical point, *Phys. Rev. B* **72**, 161201 (2005).
- [188] J. Dziarmaga, Dynamics of a quantum phase transition: exact solution of the quantum ising model, *Phys. Rev. Lett.* **95**, 245701 (2005).
- [189] A. Keesling et al., Quantum kibble-zurek mechanism and critical dynamics on a programmable rydberg simulator, *Nature* **568**, 207–211 (2019).

- [190] C. Gardiner and P. Zoller, *Quantum noise: a handbook of markovian and non-markovian quantum stochastic methods with applications to quantum optics*, Vol. 56 (Springer Science & Business Media, 2004).
- [191] S. Krämer et al., Quantumoptics.jl: a julia framework for simulating open quantum systems, *Computer Physics Communications* **227**, 109–116 (2018).
- [192] T. Jaako, J.-J. García-Ripoll, and P. Rabl, Quantum simulation of non-perturbative cavity qed with trapped ions, *1911.05087* (2019).

List of publications

In addition to this thesis the results described in the end of chapter 3 and chapters 4-7, can be found in the following peer-reviewed publications. Reference [192] that is the basis of chapter 8 has been posted to the arXiv, and is under peer review.

- T. Jaako, Z.-L. Xiang, J. J. García-Ripoll, and P. Rabl, Ultrastrong-coupling phenomena beyond the Dicke model, *Phys. Rev. A* **94**, 033850 (2016). [50]

In this paper we describe circuit QED systems in the USC regime. First the Hamiltonian of circuit QED systems in the USC regime is derived and its properties are discussed. It is shown that circuit QED systems cannot undergo Dicke superradiant phase transition. Rather a new ground state phase is discovered where the qubit and the field mode decouple, while the qubits are entangled among themselves. In this work I performed all the analytical calculations and most of the numerical simulations. The data for figure 4 was produced by Z.-L. Xiang.

- F. Armata, G. Calajó, T. Jaako, M. S. Kim, and P. Rabl, Harvesting Multi-qubit Entanglement from Ultrastrong Interactions in Circuit Quantum Electrodynamics, *Phys. Rev. Lett.* **119**, 183602 (2017). [58]

In this publication a circuit QED system in the USC regime is exploited for entanglement generation. A protocol is devised in order to prepare a circuit QED system into the USC vacuum where the qubits are in a highly entangled state, and then bring the entangled qubit state back to the non-interacting regime. In this work I was responsible for the circuit QED realization of the protocol. I designed the tunable flux qubit that was used, and performed simulations regarding to it. The master equation simulations were also performed by me. I also participated in discussing all of the results and gave feedback on the manuscript.

- D. De Bernardis, T. Jaako, and P. Rabl, Cavity quantum electrodynamics in the nonperturbative regime, *Phys. Rev. A* **97**, 043820 (2018). [51]

In this paper a toy model of cavity QED is analysed. The model consist of dipoles interacting with a single mode of electromagnetic field and with other dipoles through dipole-dipole (DD) interactions. A general cavity QED Hamiltonian is derived. Its properties are discussed first in the classical limit and then in the quantum case. The ground state phase diagram of cavity QED systems in the presence of DD interactions is obtained and analysed. New super-to-subradiant phase transition is discovered. In this publication I performed part of the analytical calculations and numerical simulations in sections 5 and 6. I also participated in discussing all the results and gave feed back on the manuscript.

- D. De Bernardis, P. Pilar, T. Jaako, S. De Liberato, and P. Rabl, Breakdown of gauge invariance in ultrastrong-coupling cavity QED, *Phys. Rev. A* **98**, 053819 (2018). [[70](#)]

This publication is concerned on the gauge equivalence of approximate two-level Hamiltonians in the USC regime. A Rabi model description of light-matter systems is derived in two prevalent gauges used in the field, the Coulomb gauge and the electric dipole gauge. It is shown that the approximate Hamiltonians give different predictions in the USC regime, and that only the Rabi model derived in the electric dipole gauge can reproduce the results of the full Hamiltonian. The culprit for the failure of the two-level-approximation in the Coulomb gauge is identified to be the momentum coupling. A circuit QED example is discussed and gauge invariance is found also in this system. In this paper I participated in devising the circuit QED example of section 5 with P. Pilar. I participated in discussing the results and gave feedback on the manuscript.

- T. Jaako, J. J. García-Ripoll, and P. Rabl, Ultrastrong-coupling circuit QED in the radio-frequency regime, *Phys. Rev. A* **100**, 043815 (2019). [[127](#)]

A circuit QED system is discussed in the limit where the qubit frequency is much larger than that of the oscillator. A Born-Oppenheimer type description of the system is used to show that several symmetry breaking transitions can be found in the ground and excited states of the system. Protocols to probe the transitions in the excited states are presented that involve only measurements on the qubits, avoiding operations on the MHz resonator. In this publication I performed all of the numerical simulations and analytical calculations.

Curriculum Vitae

Tuomas Kimmo Jalmari Jaako

Untere Weißgerberstraße 10/12

1030 Wien

+43 660 8463557

tuomas.jaako@tuwien.ac.at

Born November 17, 1990, Ylitornio, Finland

EDUCATION

- Doctor of Natural Sciences, Vienna University of Technology, 2015 -

Programme: Doctoral programme in Natural Sciences Technical Physics
Dissertation (under submission): “Ultrastrong Light-Matter Coupling in Circuit QED”

- Master of Science, University of Oulu, 2014 - 2015

Programme: Physics of matter; Major: theoretical physics, Minor: physics, mathematics;
Master’s thesis: “Validity of the semiquantum approximation in the ultrastrong coupling regime of cavity QED”

- Bachelor of Science, University of Oulu, 2010 - 2014

Programme: Physics; Major: physics, Minor: theoretical physics, mathematics
Bachelor’s thesis: “Kvanttisähköpiirin Hamiltonin operaattorin johtaminen” (“Derivation of the Hamiltonian for a quantum electric circuit”)

- Matriculation examination, Ylitornion yhteiskoulun lukio, 2009

WORK EXPERIENCE

- Project Assistant, Quantum Optics Theory, Institute of Atomic and Subatomic Physics, Vienna University of Technology; 1. Aug 2015 -
- Research assistant, Theoretical physics, Department of physics, University of Oulu; 1. Sep - 31. Dec 2014
- Research assistant, Theoretical physics, Department of physics, University of Oulu; 1. Jun - 31. Jul 2014
- Research assistant, Theoretical physics, Department of physics, University of Oulu; 1. - 30. Jun and 1. - 31. Aug 2013
- Course assistant, Department of Physics, University of Oulu; 2013 - 2015

PUBLICATIONS

- T. Jaako, J. J. García-Ripoll, and P. Rabl, *Ultrastrong-coupling circuit QED in the radio-frequency regime*, Phys. Rev. A **100**, 043815 (2019).
- D. De Bernardis, P. Pilar, T. Jaako, S. De Liberato, and P. Rabl, *Breakdown of gauge invariance in ultrastrong-coupling cavity QED*, Phys. Rev. A **98** 053819 (2018).
- D. De Bernardis, T. Jaako, and P. Rabl, *Cavity quantum electrodynamics in the non-perturbative regime*, Phys. Rev. A **97**, 043820 (2018).
- F. Armata, G. Calajo, T. Jaako, M. S. Kim, and P. Rabl, *Harvesting Multi-qubit Entanglement from Ultrastrong Interactions in Circuit Quantum Electrodynamics*, Phys. Rev. Lett. **119**, 183602 (2017).
- T. Jaako, Z.-L. Xiang, J.J. García-Ripoll and P. Rabl, *Ultrastrong coupling phenomena beyond the Dicke model*, Phys. Rev. A **94**, 033850 (2016).